

Thermoelectric transport in organic materials

by

Gun Ho Kim

A dissertation submitted in partial fulfillment
of the requirements for the degree of
Doctor of Philosophy
(Mechanical Engineering)
in the University of Michigan
2013

Doctoral Committee:

Associate Professor Kevin P. Pipe, Chair
Associate Professor Jinsang Kim
Professor Katsuo Kurabayashi
Associate Professor Pramod S. Reddy
Associate Professor Max Shtein

© Gun-Ho Kim 2013

All Rights Reserved

Acknowledgements

This work is the result of the time and effort of many people, whom I thank from the bottom of my heart.

Prof. Kevin Pipe has been a great teacher and advisor for past four years. He continuously brought sharp insights which initiated most of my works and solved many obstacles I encountered. I appreciate and am greatly impressed by his kindness and friendly attitude to me, which have allowed me to focus on research and enjoy the most challenging period of my life. I have learned not only scientific knowledge but also respectable life spirit from the time I spent with him.

I thank Prof. Max Shtein for showing his enthusiasm and visions about organic electronics, which made me decide to seek the possibilities of organic thermoelectrics. Prof. Pramod Reddy kindly provided practical tips for building a low noise thermoelectric measurement setup. I learned many important concepts and experimental methods for the thin film thermal conductivity measurement from Prof. Katsuo Kurabayashi. My special thanks go to Prof. Jinsang Kim who helped me learn polymer-based organic materials, and my major achievements would not be possible without his support. I appreciate, again, all my committee members for their time and insightful comments.

The Center for Solar and Thermal Energy Conversion and the US Department of Energy provided necessary financial support for my research.

I am indebted to my lab mates. Prof. Paddy Chan, Dr. Kwang Hyup An, Dr. Abhishek Yadav, Dr. Yansha Jin, Shaurjo Biswas, and Steve Morris provided guidance for using lab instruments and facilities. I thank Dr. Huarui Sun for his good spirit which made me laugh often. I thank Kejia Zhang for helping me perform the thermal conductivity measurement. I thank Vahid

Rashidi for his useful simulation of polymers. I thank Si Hui for his pleasant personality. My special thanks go to Lei Shao who has helped me to a great extent with essential cleanroom works. Likewise, I appreciate my collaborators. I thank Kyeongwoon Chung for explaining many experimental instruments related to polymeric materials. I deeply thank Dongwook Lee and Apoorv Shanker for intensively supporting my recent ideas of thermal conductivity in organic materials. I appreciate Yoonseob Kim for providing his interesting samples. I thank Shuyi Zhang for providing her samples which widened my insight for oxide materials. Dr. Sangwoo Lee provided great help with the design of an amplifier circuit. I also thank Brenda Vyletel for her many kind assistances.

I also want to extend appreciation to my friends in Ann Arbor: Heonjeong Kim, Youngbum Kwon, and Yoonmyung Lee. I have had many joyful experiences with them which have brought great fun to my time in Ann Arbor.

Finally, I admit that I would not be able to begin and continue my study without support from my parents and wife. I deeply appreciate my parents for their unwavering love and prayer. My sincere thanks go to my wife, Hyejin Kim, for her endless support and for enduring my shameful temper sometimes. I thank God for my son Juwon Kim and the anticipated birth of my second son. The happiness that my wife and boys bring me is truly more than what I can express.

Gun-Ho Kim, 2013 November

Table of contents

Acknowledgements	ii
List of figures	viii
Abstract	xi
Chapter 1	
Introduction	1
1.1 Thermoelectric materials	1
1.2 Organic thermoelectric materials	5
1.3 Charge carrier transport in organic semiconductors	8
1.4 Thermally conductive organic compounds	10
Chapter 2	
Experimental setup for thermoelectric measurements	13
2.1 Temperature measurement in the ambient conditions	14
2.1.1 Minimization of error due to air convection	14
2.1.2 Type of temperature sensor	17
2.2 Voltage measurement	19
2.2.1 Circuitry with a low input bias current	20
2.2.2 Parasitic Seebeck voltages	22
2.2.3 Integral Seebeck measurement method	25
2.2.4 Energy barrier at the electrode	27
2.2.5 Differential technique of varying sample lengths	28
2.3 Stable temperature gradient	29
2.3.1 Fast response temperature sensor	30
2.3.2 Liquid-cooled heat sink	30

2.4	Thermal conductivity measurement by the 3ω method	31
2.4.1	Theory of the 3ω method	32
2.4.2	Differential 3ω method	36
2.4.3	Calibration and measurement setup	37
2.4.4	Circuitry for the 3ω method	39
2.4.5	3ω method for measuring the anisotropic thermal conductivity	39
Chapter 3		
Charge carrier transport in organic semiconductors		
3.1	Transport of localized charge carriers	43
3.1.1	Carrier localization in disordered materials (Anderson localization)	43
3.1.2	Static and dynamic disorder	45
3.1.3	Transport of localized charge carriers	46
3.1.4	Uncertainties in previous hopping models	48
3.2	Thermoelectric model	49
3.2.1	Model for the Seebeck coefficient	50
3.2.2	Dependence of the Seebeck coefficient on the hopping parameters	55
3.3	Weak carrier localization in high mobility OSCs	56
3.3.1	Pentacene bulk films and field-effect transistors	57
3.3.2	PEDOT bulk film doped by various chemicals	60
3.4	Three regimes of the charge carrier transport in OSCs	63
Chapter 4		
Weak carrier localization in doped pentacene bulk films		
4.1	Sample preparation and characterization	67
4.1.1	Pentacene films with various degrees of static disorder	67
4.1.2	Spontaneous dedoping technique	68
4.1.3	Simultaneous measurement of S and σ	69
4.2	Transition of the transport regime in bulk pentacene films	71
4.2.1	Bulk mobility measurement	71
4.2.2	Transition from an activated to an intermediate hopping regime	73

Chapter 5

High-performance polymer-based thermoelectric materials	79
5.1 Previous achievements and limitations in thermoelectric materials	80
5.2 Sample preparation and characterization	81
5.2.1 Sample preparation	82
5.2.2 Sample geometry	83
5.2.3 Determination of S	84
5.2.4 Determination of σ	85
5.2.5 Determination of doping-dependent cross-plane thermal conductivity κ_y	85
5.2.6 Determination of in-plane thermal conductivity κ_x	87
5.2.7 Analysis of XPS spectra	88
5.2.8 Morphology of EG treated PEDOT:PSS	89
5.2.9 Stability of EG-treated PEDOT:PSS in atmosphere	89
5.3 Dopant volume as an engineering parameter for organic thermoelectric materials	91
5.3.1 Optimal carrier concentration for maximum $S^2\sigma$ in OSCs	91
5.3.2 Inefficiency of molecular doping	94
5.3.3 Strong dependence of $S^2\sigma$ on dopant volume	95
5.4 Effect of reduction in dopant volume on ZT	98
5.4.1 Selective removal of PSS	98
5.4.2 S and σ increases while κ decreases, causing ZT to increase	100

Chapter 6

Thermally conductive amorphous plastics	104
6.1 Impacts of thermally conductive organic materials on the plastics industry	105
6.2 Previous efforts to improve κ in organic materials	107
6.2.1 High- κ filler method	108
6.2.2 Crystalline organic materials	108

6.3	A design principle for enhanced thermal conductivity in organic materials	109
6.3.1	Model for κ as a function of intermolecular junction conductance	109
6.3.2	van der Waals bonding	112
6.3.3	Hydrogen bonding	113
6.4	Sample preparation and characterization	114
6.4.1	Sample preparations	114
6.4.2	Sample characterization	118
6.5	Thermally conductive amorphous organic materials	122
6.5.1	Mixtures of PMMA and PVA	122
6.5.2	Mixtures of PAP and PVA	128
6.5.3	κ versus ϕ	130
Chapter 7		
Conclusions and insights		131
References		136

List of figures

Figure 1.1	U.S. energy consumption in 2012.	2
Figure 1.2	Traditional heat engine vs. solid-state (thermoelectric) heat engine.	3
Figure 1.3	The abundance of elements in the earth's crust.	4
Figure 1.4	Current status of OSC-based thermoelectric materials.	6
Figure 1.5	Dependence of the electrical conductivity (σ), Seebeck coefficient (S), and thermoelectric power factor ($S^2\sigma$) on the carrier concentration in silicon.	7
Figure 2.1	Seebeck measurement setup.	15
Figure 2.2	Various types of sensors for steady-state temperature measurement.	18
Figure 2.3	Circuitry used for electrical measurement.	20
Figure 2.4	Probe configuration for the Seebeck voltage measurement.	23
Figure 2.5	Illustration of the effect of a contact built-in potential on the measured Seebeck coefficient.	28
Figure 2.6	Differential techniques used for measurements of S and σ	29
Figure 2.7	Sample configuration for the 3ω measurement.	33
Figure 2.8	Temperature coefficient of resistance (TCR) of the metal line heater.	38
Figure 2.9	Anisotropic ratio of the thermal conductivity.	41
Figure 3.1	Anderson localization.	44
Figure 3.2	Dependence of the carrier mobility on the normalized carrier concentration.	54
Figure 3.3	Seebeck coefficient versus n/N_0 for different a_{DOS} and α	56
Figure 3.4	Seebeck coefficient, electrical conductivity, and mobility in pentacene FETs and bulk films.	58
Figure 3.5	Hopping parameters in PEDOT.	61
Figure 3.6	Three regimes of hopping transport.	65

Figure 4.1	AFM topography images in pentacene films.	68
Figure 4.2	Seebeck voltage measurement during iodine dedoping.	70
Figure 4.3	Comparison between n/N_0 calculated by Fermi-Dirac statistics and the Boltzmann approximation.	73
Figure 4.4	Seebeck coefficient and electrical conductivity during iodine dedoping.	75
Figure 4.5	Dependence of carrier mobility on carrier concentration for various grain sizes.	76
Figure 4.6	Required iodine concentration for $n = 10^{16} \text{ cm}^{-3}$	78
Figure 5.1	Temperature rise across the PEDOT:PSS layer.	87
Figure 5.2	Ratio of the PSS monomer to PEDOT monomer (χ) at different EG treatment times.	89
Figure 5.3	Tapping-mode AFM images ($500\text{nm} \times 500\text{nm}$) for PEDOT:PSS.	90
Figure 5.4	Effect of the EG treatment on the air-stability of PEDOT:PSS.	90
Figure 5.5	Hopping activation energy (ϵ_a), carrier mobility (μ), and carrier concentration (n).	92
Figure 5.6	Thermoelectric power factor for various α and r/b	93
Figure 5.7	Ratio of PSS to PEDOT in typical PEDOT:PSS.	95
Figure 5.8	The 2D trajectory of doping (or dedoping) for efficient maximization of thermoelectric power factor in an OSC.	97
Figure 5.9	Thicknesses of PEDOT:PSS at different EG treatment times.	99
Figure 5.10	S_{2p} XPS spectra in pristine PEDOT:PSS and EG-treated PEDOT:PSS.	100
Figure 5.11	Thermoelectric properties of PEDOT:PSS at various dedoping times.	101
Figure 6.1	Schematics of PMMA:PVA and PAP:PAA mixtures.	115
Figure 6.2	Thickness of i- and a-PMMA:PVA and PAP:PAA.	116
Figure 6.3	Measured temperature rise across the PAP:PAA film.	118
Figure 6.4	AFM topological images for the i- and a-PMMA(45 mol%):PVA(55 mol%), the PAP(30 mol%):PAA(70 mol%), and the PAP spin-coated films.	120
Figure 6.5	Phase segregation occurred in the i-PMMA(30 mol%):PVA(70 mol%) film.	122

Figure 6.6	Tapping-mode AFM topological and phase images for i- and a-PMMA:PVA and PAP:PAA spin-coated films.	125
Figure 6.7	Thermal conductivity in the H-bonding mixtures.	127
Figure 6.8	O _{1s} XPS spectra of i- and a-PMMA:PVA and PAP:PAA at various mol% of H-bonding acceptor monomer.	129
Figure 7.1	OSCs – past, current, and future.	134

Abstract

Organic materials are well-suited to certain applications due to their low cost, low weight, and mechanical flexibility, but are less desirable for other applications due to poor conduction of electricity and heat. The contributions of my work focus on strategies to mitigate these limitations in current and emerging organic materials, developing techniques to improve charge carrier mobility in doped organic semiconductors (OSCs) and improve thermal conductivity in common commercial plastic materials.

Understanding of charge carrier transport is a prerequisite to developing a good electrical conductor. In OSCs, charge carriers are historically assumed to be strongly localized, which bears heavily on their assumed mechanism of transport; however, the degree of localization in emerging high-conductivity OSCs has been the subject of intense study. My work develops a model that can be used with thermoelectric measurements to quantitatively determine the degree of carrier localization in an OSC, and applies this technique to high-conductivity polymers and iodine-doped pentacene films. The model also suggests a strategy to improve energy conversion efficiency in OSC-based thermoelectric materials by reducing dopant volume. This strategy was confirmed experimentally to vary all three thermoelectric parameters (Seebeck coefficient, electrical conductivity, and thermal conductivity) in a manner that increases thermoelectric efficiency, in sharp contrast to their trade-offs in common inorganic semiconductor based

thermoelectric materials. This method led to 70% increase in the thermoelectric efficiency from the previous record for an OSC.

Finally, I propose and study methods to increase inter-chain bonding in polymer mixtures as an efficient engineering route to improve their thermal conductivity. By controlling the mole fractions of components to favor (strong) hydrogen bonds over weaker van der Waals bonds, the thermal conductivities of mixtures of common commercial polymers are increased by an order of magnitude, reaching $1.72 \text{ W m}^{-1}\text{K}^{-1}$, the highest value yet reported among non-crystalline polymer materials without the incorporation of fillers.

Chapter 1

Introduction

1.1 Thermoelectric materials

Heat is abundant, since it is the form of energy to which other types of energy ultimately convert. This abundant heat energy at relatively low temperatures is known as “waste heat”, which cannot be easily utilized in traditional heat engines. Figure 1.1 shows the U.S. national energy consumption in 2012, during which time more than half of the total energy input was immediately converted to waste heat. Moreover, the remaining ~40% which was used to perform work (e.g., transportation, electricity) was eventually converted into waste heat. For example, vehicle kinetic energy used for transportation is eventually converted to waste heat at the car brake when it stops. Therefore, within the bounds of ideal (Carnot) thermodynamic efficiency, a technology that can convert waste heat to a more useful form of energy can significantly improve the overall energy consumption efficiency.

Thermoelectric materials directly convert heat to electricity and vice versa (Fig. 1.2), and can use low-quality waste heat for electricity generation. The Seebeck effect occurs in a solid when an applied temperature gradient leads to a gradient in the average velocity of charge carriers (which is proportional to kT , where k is the Boltzmann constant and T is the absolute temperature), causing a net diffusion of carriers from the hot side to the cold side. This is analogous to the

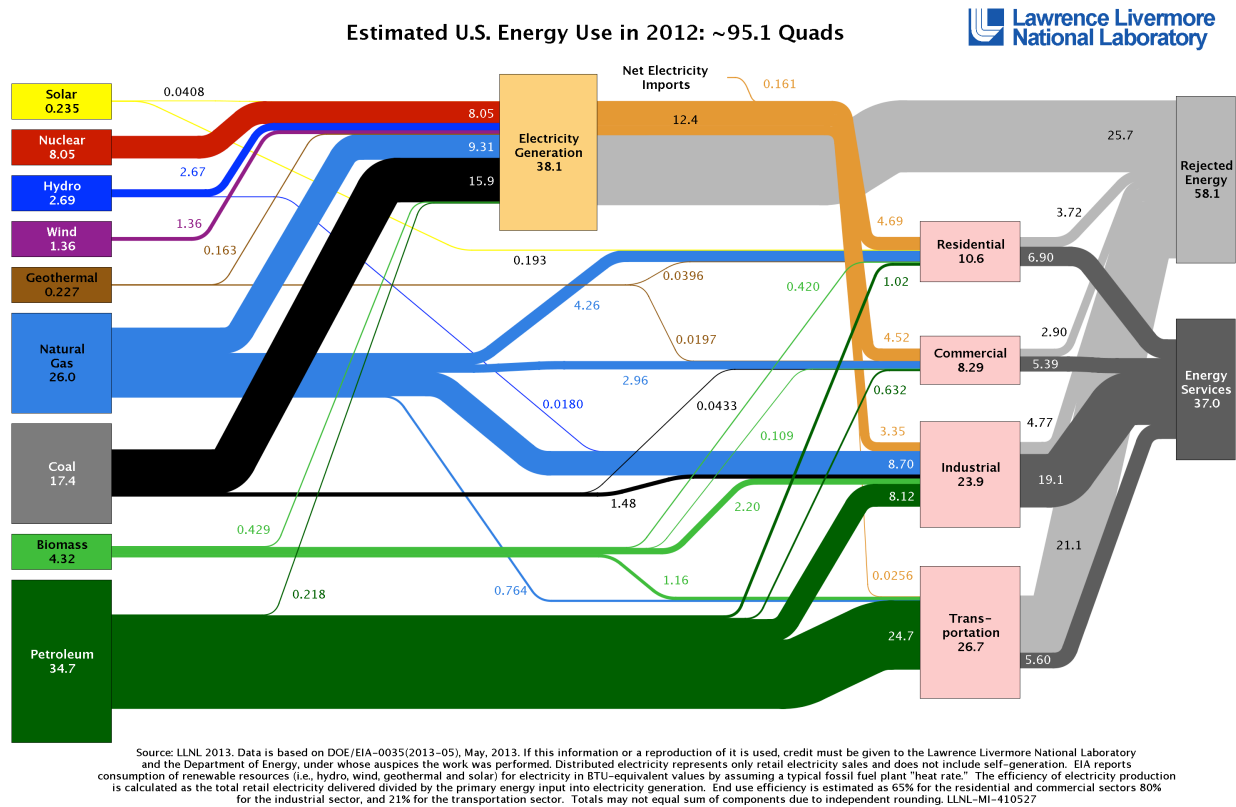


Figure 1.1 | U.S. energy consumption in 2012. Overall energy consumption efficiency is 37%, while 58.1% of energy is wasted. Adapted with permission from the Lawrence Livermore National Laboratory.

thermally-induced diffusion of air molecules (e.g., wind), except that the carriers in a solid (electrons) have an electric charge and hence their diffusion generates an electric potential. The Seebeck coefficient (which has units of VK^{-1}) quantitatively defines the electrical potential induced by a unit temperature difference. In thermoelectric devices, this direct energy conversion between heat and electricity occurs without any moving parts (e.g., piston, turbine), which makes thermoelectric devices very small, light, and reliable compared to traditional heat engines. These advantages of small size and the low weight are essential particularly for harvesting useful energy from waste heat, since waste heat is secondary energy source, which should be utilized without substantial increase in the system weight and volume. For example, waste heat from human body, car, and airplane is hard to be utilized by a traditional heat engine because of its

heavy weight and bulky size. Together with their portability, the outstanding reliability of thermoelectric devices fits to the power generation requirements for applications, for which the system reliability is critical (e.g., deep-space probes). These benefits of portability and reliability apply equally to the thermoelectric cooling application, as a thermoelectric material transforms itself into a heat pump simply by biasing it with an electric current rather than a heat current. A silent, slim, and reliable refrigerator made of thermoelectric materials is already available in market.

The energy conversion efficiency of a thermoelectric material depends on both its thermal and electrical transport properties. It should be a good electrical conductor in order to transport charge carriers efficiently, and a good thermal insulator in order to maintain a large temperature difference between the heat sink and the heat source at a given heat flux. The conversion

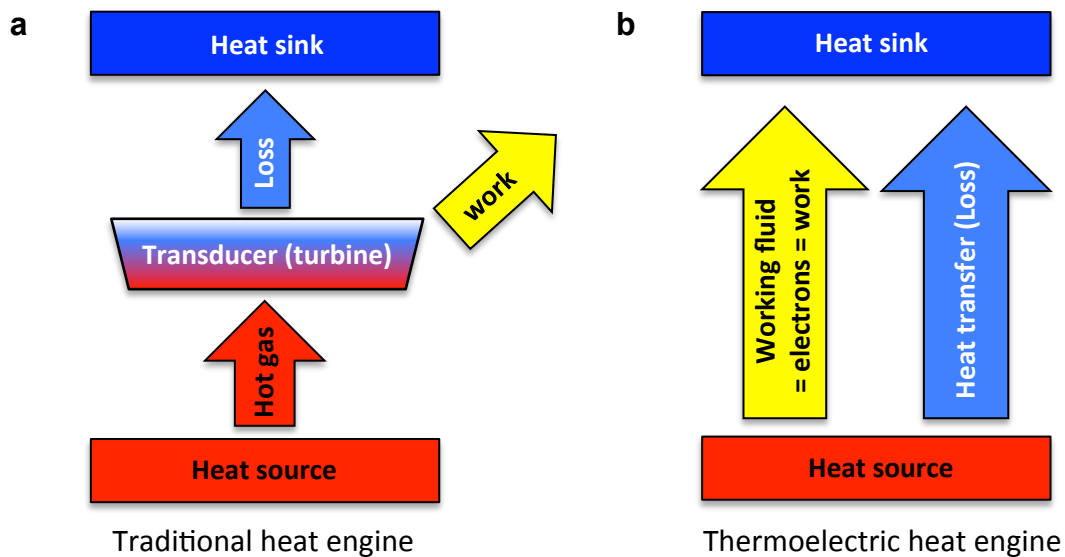


Figure 1.2 | Traditional heat engine vs. solid-state (thermoelectric) heat engine. (a) Traditional heat engine: the flow of working fluid is converted to other types of energy using a transducer (e.g., turbine, cylinder); ejected working fluid at low temperatures represents energy loss. **(b)** Working fluid is charge carriers, and its flow directly defines the engine output, while heat conduction by other mechanisms (e.g., phonon diffusion) corresponds to energy loss.

efficiency is dictated by the thermoelectric figure-of-merit $ZT (= S^2 \sigma T / \kappa$, where S is the Seebeck coefficient, σ is the electrical conductivity, κ is the thermal conductivity, and T is the absolute temperature). The requirements for an efficient thermoelectric material (i.e., large σ , large S , and small κ) lead to a limited choice of candidate materials, which have traditionally been heavy metal alloys such as Bi_2Te_3 or PbTe ($ZT \approx 1$). For the past few decades, engineering of nanostructures within these materials [1, 2] has significantly improved their energy conversion efficiency, achieving levels comparable to that of a traditional heat engine [3], yet the scarcity of heavy metal elements increases the cost per watt, and hence limits their practical use for power generation and refrigeration. Figure 1.3 illustrates the abundance of elements in the earth's crust,

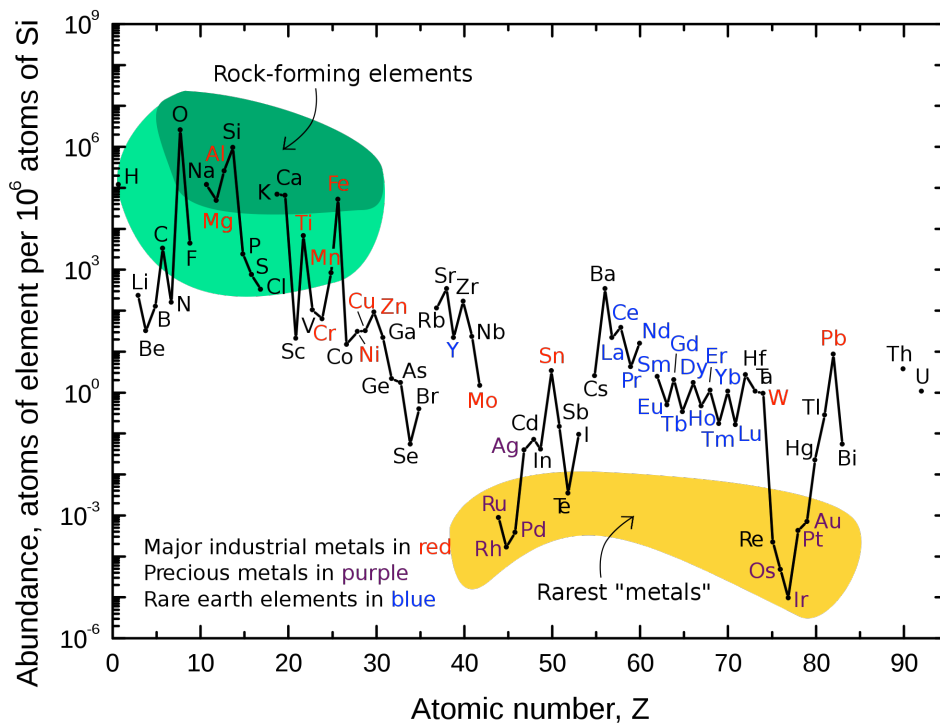


Figure 1.3 | The abundance of elements in the earth's crust. Element abundance is inversely proportional to the atomic number in general because of the manner in which they were created. The most popular element in current thermoelectric materials, tellurium (Te), is one of the rarest elements in the earth's crust. The figure is reproduced from Wikipedia: (http://en.wikipedia.org/wiki/Abundance_of_the_chemical_elements).

showing that one of the most popular elements for thermoelectric materials (tellurium) is as rare as gold.

Several earth-abundant elements in the Fig. 1.3 have been investigated in an attempt to reduce the cost of a thermoelectric module. Replacing the tellurium in PbTe by selenium showed promising thermoelectric performance [4], while TE materials based on silicon nanowires exhibited a large increase in ZT due to a thermal conductivity reduction of two orders of magnitude relative to bulk silicon [5]. Oxides have likewise been studied for high-temperature thermoelectric applications [6].

1.2 Organic thermoelectric materials

Organic semiconductors are based on earth-abundant elements (e.g., C, H, O) and have many advantages over inorganic semiconductors (ISCs) such as low cost, low weight, and mechanical toughness. Their low thermal conductivity is beneficial to thermoelectric conversion efficiency, which is inversely proportional to κ (i.e., $ZT = S^2\sigma T/\kappa$). In spite of these advantages, OSCs have not traditionally been considered candidate thermoelectric materials, since they have historically been poor electrical conductors due to low charge carrier mobility. While ZT in OSCs had been typically 3 orders of magnitude lower than in heavy-metal alloys, it has rapidly improved since 2011, and now is reaching a value similar to that of the heavy-metal alloys, as shown in Fig. 1.4. This dramatic improvement of the thermoelectric efficiency in OSCs is due to a better understanding of charge carrier transport [7], new molecular designs [8], and novel fabrication methods [9, 10]. Like significant improvements in other applications such as organic light

emitting diodes (OLEDs) [11], photovoltaics (OPVs) [12], and field effect transistors (OFETs) [10], OSCs are now being considered as promising candidate thermoelectric materials.

The first notable enhancement in the efficiency of organic thermoelectric materials was observed in poly(3,4-ethylenedioxythiophene) PEDOT, in which the carrier concentration was optimized to maximize the thermoelectric power factor [13]. Since the Seebeck coefficient and electrical conductivity typically have opposite dependences on the carrier concentration, thermoelectric materials have an optimal carrier concentration at which the thermoelectric power factor ($S^2\sigma$) is maximized (Fig. 1.5). To realize this optimal carrier concentration, the doping concentration

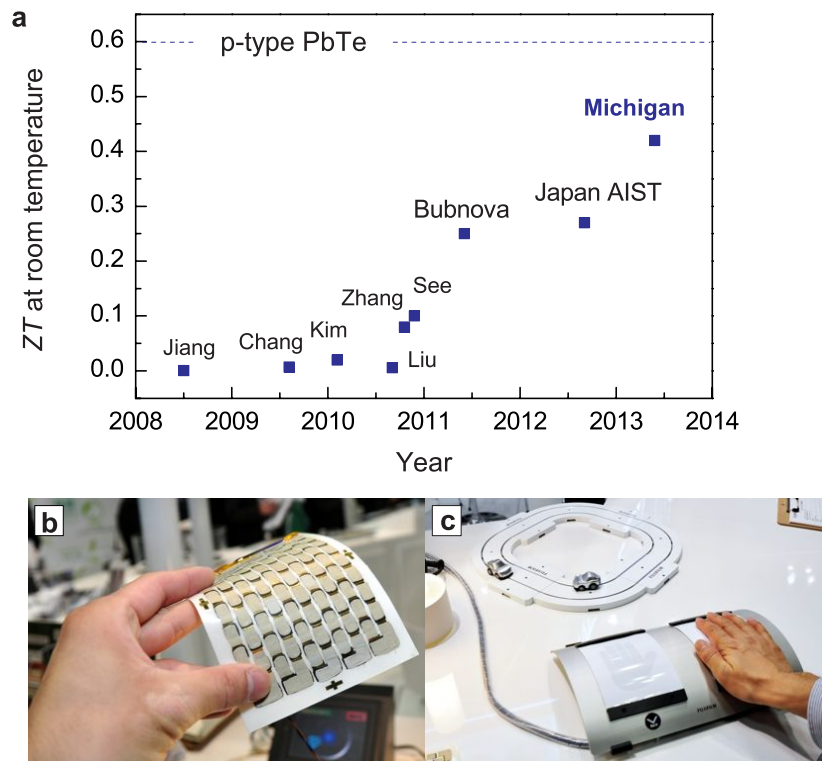


Figure 1.4 | Current status of OSC-based thermoelectric materials. (a) Extraordinary recent progress in bulk (i.e., non-transistor) OSC-based TE materials (with respect to the common inorganic TE material PbTe). Data points appear in References [13-20]. **(b,c)** Flexible OSC-based TE module developed by Fujifilm that runs a toy car using the heat from a human hand [21]. The Japan AIST ZT is from [21]. Pictures are reproduced from ref. [21].

must be precisely controlled. However, dopants in OSCs alter the weak van der Waals interactions between molecules, and therefore controlling the dopant concentration without sacrificing charge carrier transport properties is challenging. Bubnova et al. overcame this problem using chemical reduction in tosylate-doped PEDOT, and demonstrated the first meaningful value of ZT (0.25) in an OSC at room temperature [13]. Composite materials made of conducting polymers and ISCs showed large increases in the Seebeck coefficient without sacrificing the electrical conductivity much, leading to meaningful enhancements in the thermoelectric power factor [18, 19]. Carbon nanotube-polymer composites demonstrated a promising value of the thermoelectric power factor ($\sim 500 \text{ W m}^{-1}\text{K}^{-2}$) [22]. Fujifilm demonstrated an efficient flexible thermoelectric module based on a thermoelectric polymer [21]. A large thermoelectric power factor ($S^2\sigma$) comparable to that of Bi_2Te_3 was measured in an

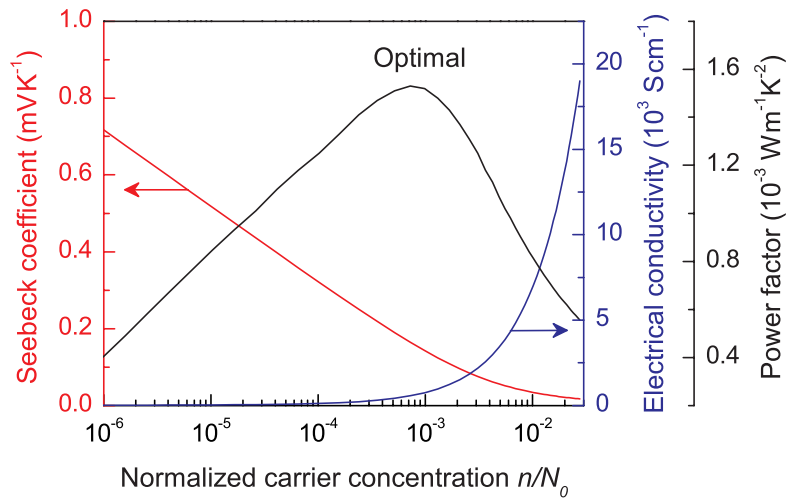


Figure 1.5 | Dependence of the electrical conductivity (σ), Seebeck coefficient (S), and thermoelectric power factor ($S^2\sigma$) on the carrier concentration in silicon. The opposite dependences of the electrical conductivity and Seebeck coefficient result in an optimal value of the power factor. The carrier concentration is normalized by the atomic density of silicon ($5 \times 10^{22} \text{ cm}^{-3}$). The electrical conductivity and Seebeck coefficient are calculated taking into account impurity scattering [23, 24].

electrochemically modulated polymer transistor [25]. In addition these previous achievements, my work has shown that minimizing the total dopant volume is essential when maximizing $S^2\sigma$ in OSCs. By removing (primarily) non-ionized poly(styrenesulfonate) (PSS) dopants from PEDOT, ZT was increased by almost 70% from the previous record [20].

1.3 Charge carrier transport in organic semiconductors

Like the phase diagram of water is key to optimizing steam engine efficiency, understanding the transport of charge carriers is critical to improving thermoelectric efficiency, since charge carriers are the working fluid in a thermoelectric material (Fig. 1.2). Since the discovery of highly conductive iodine-doped polyacetylene [26], charge transport in OSCs has been intensively studied. As described in Anderson's early work on carrier transport in disordered materials [27], charge carriers in OSCs are localized rather than extended throughout the material, since OSCs are either statically disordered (e.g., crystal imperfections, impurities) or dynamically disordered (intermolecular vibrations) near room temperature. Note that the thermal energy at room temperature is 25 meV, which is on the same order as the van der Waals interaction (which is the predominant form of intermolecular bonding in OSCs), while a covalent bond is on the order of 1 eV. This low energy of intermolecular bonding leads to considerable thermally induced intermolecular vibrations, which result in the localization of charge carriers even in a single crystal OSC [28, 29]. For this localized carrier, an external energy source (e.g., thermal energy, electric field) is required to overcome the energetic barrier, and the carrier transport is described by "thermally activated hopping". Before the mid 2000s, this description of hopping transport has well explained the observed experimental data in many OSCs.

However, as the material quality of OSCs has rapidly improved, several OSCs have shown a discrepancy from the hopping model. For example, the charge carrier mobility in high-quality pentacene transistors is either independent of temperature or even decreasing with temperature [30, 31], both of which have been thought of as the signature of “band-like” transport (i.e., a fully extended electronic wavefunction). The traditional hopping model (which assumes strong carrier localization) cannot explain these dependences of mobility on temperature, yet evidence of carrier localization has been observed even in single-crystal pentacene [28] and OFETs, which show “band-like” transport [31].

These recent results suggest that strong carrier localization, which has traditionally been assumed in previous hopping models [32, 33], should be reconsidered. In the hopping model based on the Miller-Abraham transition rate [34], three material parameters dictate the carrier mobility: the degree of carrier localization, the degree of energetic disorder, and the energy exchange rate between electrons and phonons (the external energy source for hopping transport). Since all three parameters directly determine the carrier mobility, they are difficult to determine independently from electrical conductivity or carrier mobility data. In practice, this uncertainty has led to a qualitative assumption of strong carrier localization [32] because the other two hopping parameters (which are likewise uncertain) can be arbitrarily modified to fit a given set of experimental data.

As part of my work, I developed a model of the Seebeck coefficient in terms of the hopping parameters that is appropriate for OSCs, and showed how this model can be used to derive the localization length in such materials [7]. Because the Seebeck coefficient (S) is the voltage induced by a given temperature gradient, it relates to the energy distribution of conducting charge carriers. Since the carrier localization length, together with the shape of the electronic

density of states, strongly affects this distribution, the Seebeck coefficient is sensitive to these quantities. Furthermore, its dependences on these parameters are different than those of electrical conductivity, allowing simultaneous use of Seebeck coefficient and electrical conductivity data to independently determine the parameters. Using this method, the localization length in several OSCs was quantitatively extracted from experimental data. This derived localization length represents the material's bulk properties and therefore is more relevant to thermoelectric applications.

1.4 Thermally conductive organic materials

Organic materials are intrinsically thermal insulators due to their softness caused by weak van der Waals intermolecular interaction. Improving thermal conductivity could have a large effect on the entire industry related to organic materials such as OLEDs, OFETs, electronics packaging, thermal interface materials, and automobile applications. For example, the electrical insulator used in a light bulb, plastic parts in an automobile, and the active organic layer in OLEDs should dissipate heat fast for both device performance and reliability. A large demand for thermally conductive electronic packaging materials exists in the electronic industry, as the power density of electronic components increases exponentially by the Moore's law. Furthermore, improving thermal conductivity reduces the price of plastic products as they are typically made by thermal machining (e.g., thermoforming, injection molding), during which the time required for melting and cooling down the thermally insulating organic material increases the manufacturing time and cost; this long melting (cooling) time is particularly considerable for the bulky plastic parts used for the automobile application (e.g., car bumper) [35].

Previous efforts for increasing thermal conductivity have mainly been based on adding species that have a high thermal conductivity into the polymer matrix. Popular materials for the fillers are thermally conductive metals (e.g., silver and copper) [36], carbon nanotubes (CNTs) [37], and graphene flakes or graphite [38, 39]. Typical thermal conductivities in these filler-polymer composites are few $\text{W m}^{-1}\text{K}^{-1}$, which is larger than the polymer matrix (0.1 to $0.5 \text{ W m}^{-1}\text{K}^{-1}$), yet far lower than the averaged value of the used filler and polymer. The inefficiency of the filler method is due to the large boundary resistance between the filler and polymer, because the bonding between them is still weak van der Waals interaction, which is the bottleneck of the overall heat transfer in organic materials. Furthermore, a large volume fraction of the fillers is required to exceed the percolation threshold, at which the thermal conductivity starts considerably increasing; the percolation threshold for the typical sphere-shaped filler is around 20 volume%, equivalent to ~ 90 weight% for the metal filler. This large amount of the fillers not only increases the material cost but also alters other physical properties in an undesired manner. Interestingly, a single polymer chain is itself a good thermal conductor, having thermal conductivities on the order of a few hundreds of $\text{W m}^{-1}\text{K}^{-1}$ [40], which is far larger than that of a bulk polymer film and comparable to silver or copper. When these highly conductive polymer chains are aligned to form a crystalline organic material, the thermal conductivity remains large along the aligned direction, ranging from 20 to $100 \text{ W m}^{-1}\text{K}^{-1}$ [41, 42]. However, this large κ gained by nano-scale crystallization is hard to scale-up and practically apply to most plastic-related products, which rely on low cost.

The tremendous difference in thermal conductivity between an individual polymer chain (or crystalline polymer fiber) and common amorphous organic materials implies that weak intermolecular interactions (in particular, van der Waals bonds) limit the thermal conductivities

of organic materials. Thus, strengthening of this weak intermolecular interaction is an important route for altering the thermal conductivities of organic materials; however, to the author's best knowledge, no studies have been performed in this area.

Here, I propose a strategy for the enhanced thermal conductivity in organic materials by improving intermolecular interactions. Hydrogen bonding (H-bonding) occurs in many organic materials and is a particularly strong intermolecular interaction, typically 10 to 100 times stronger than a van der Waals bond. The prevalence and strength of H-bonding makes it an ideal choice for the proposed strategy. To experimentally demonstrate the strategy, two commercially available polymers, poly(methyl methacrylate) (PMMA) (which contains the hydrogen acceptor (C=O)) and poly(vinyl alcohol) (which contains the hydrogen donor (OH)), were mixed, and their thermal conductivities at various mixture ratios (i.e., hydrogen bond concentrations) were tested. An exceptionally high thermal conductivity was observed in the mixture containing the maximum concentration of hydrogen bonds, reaching over $1 \text{ Wm}^{-1}\text{K}^{-1}$. In addition to this high κ in PMMA:PVA, κ in a certain mixture of poly(acryloyl piperidine) (PAP) and poly(acrylic acid) (PAA) was measured to be $1.72 \pm 0.23 \text{ Wm}^{-1}\text{K}^{-1}$, the highest value yet reported among all non-crystalline organic materials.

Chapter 2

Experimental setup for thermoelectric measurements

The measurement of thermoelectric properties includes several sub-measurements of the Seebeck coefficient, electrical conductivity, and thermal conductivity. While the measurement of electrical conductivity is relatively straightforward, measurements of Seebeck coefficient and thermal conductivity require temperature measurements, for which careful consideration of possible heat leakages to (or from) the temperature sensor should be taken into account. Also, the electrical resistivity of organic semiconductors (OSCs) is typically large due to their low carrier mobility, requiring a low-noise voltmeter with very large input impedance for accurate Seebeck measurement. While a large temperature gradient allows for a large Seebeck voltage signal, a tradeoff exists due to the increased heat leakages by air convection and radiation at elevated temperatures. Additionally, since the Seebeck coefficient has a non-linear relationship with temperature, the applied temperature difference should be as small as possible to derive a precise Seebeck coefficient at a certain temperature. In this chapter, I will discuss in detail the challenges of thermoelectric and thermal conductivity measurements, and give practical tips for experimental design and data analysis.

2.1 Temperature measurement in ambient conditions

A prerequisite of accurate Seebeck coefficient and thermal conductivity measurements is getting precise temperature data. Temperature is the result of heat transfer, which can occur via conduction, convection, or radiation. The experimental design principle of accurate temperature measurement is to minimize the heat transfer between the sensor and the point to be measured, since the temperature deviation due to the thermal interface resistance is proportional to the magnitude of heat transfer. At the same time, the heat transfer between the sensor and the sample should be small enough to not perturb the existing temperature profile within the sample. While an electrical probe can be easily isolated since the contrast ratio of electrical conductance between the metal probe and the surrounding materials (e.g., air or insulating sheath) is very large in most cases, a thermal probe is hard to isolate, since various paths of heat transfer due to convection by the surrounding fluid, conduction by adjacent objects, and radiation can readily affect its temperature. In this sense, the type and size of the temperature sensor should be carefully chosen in order to minimize the heat transfer between the sensor and the tested sample.

2.1.1 Minimization of error due to air convection

Thermoelectric measurements are often performed in air, since an ambient measurement has many advantages over a vacuum measurement, including cheaper apparatus, less time required for the measurement, and easier sample preparation. For an accurate temperature measurement under ambient conditions, the heat transfer between the temperature sensor and the surrounding air should be carefully taken into account. Figure 2.1 shows the Seebeck measurement setup used in this work; the differential setup (Fig. 2.1a) uses two thin thermocouple probes for surface

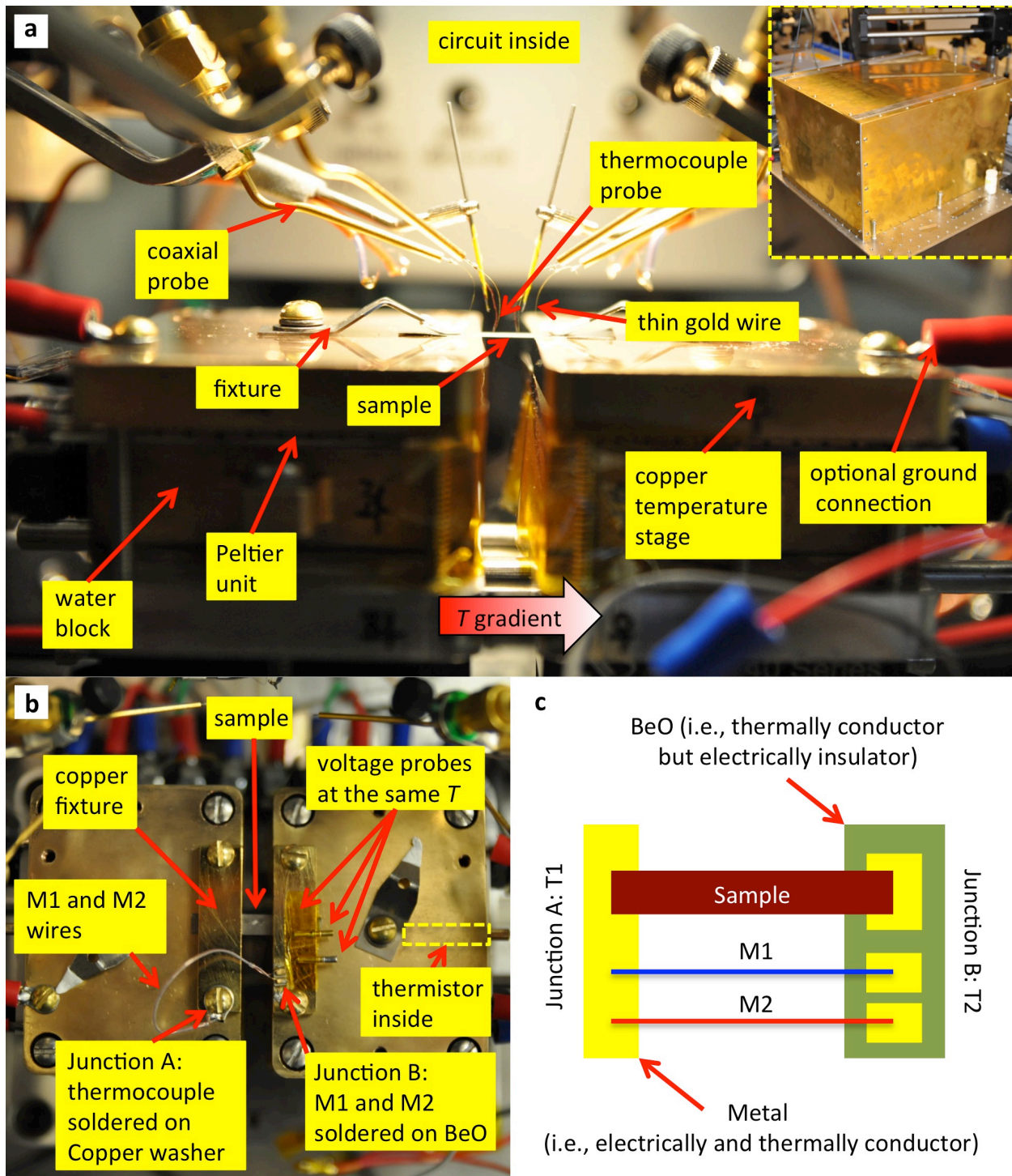


Figure 2.1 | Seebeck measurement setup. (a) Differential Seebeck setup, in which Seebeck voltages are measured at different temperatures. Inset is the Faraday cage used for shielding the setup described in a and b. (b) Integral Seebeck setup, in which Seebeck voltages are measured at the same temperature and are referenced to a metal with a known Seebeck coefficient (M1, M2). (c) Schematic illustration of the integral Seebeck measurement. Tested sample is a thin nickel sheet, the Seebeck coefficient of which was measured at 297K to be $-19.95 \mu\text{VK}^{-1}$ by the setup a and $-20.03 \mu\text{VK}^{-1}$ by the setup b.

temperature measurement. Since the temperature probe is surrounded by air, the measured temperature is the result of not only the heat conduction from the sample but also heat convection by the surrounding air. To minimize the deviation between the measured and real temperature of a sample, the magnitude of the heat transfer between the sensor and air must be much smaller than the heat conduction between the sensor and the sample.

To address this heat leakage by air convection, the temperature of the surrounding air (T_∞) at the given sample temperature (T_s) must be calculated. For a thin air layer very close to the sample surface, the air temperature gradient (∇T_{air}) can be calculated based on Fourier's conduction and Newton's convection laws:

$$q_H = -\kappa \nabla T_{air} = -h(T_s - T_\infty), \quad (2.1)$$

where q_H is the heat flux between the sample surface and the air, κ is the air thermal conductivity, and h is the heat transfer coefficient. The heat transfer coefficient for natural convection is given by [43]:

$$h = \frac{C_1 \kappa Ra^{C_2}}{L}, \quad (2.2)$$

where Ra is the Rayleigh number, L is the characteristic length ($= A_s/p$, where A_s is the sample area and p is its perimeter), and the constants C_1 and C_2 depend on the magnitude of Ra . At room temperature, Ra of air is given by $0.71 \times 78 \times 10^9 \times (T_s - T_\infty) \times L^3$ [44]; for $L = 6.35$ mm (e.g., a $25.4\text{mm} \times 25.4\text{mm}$ square sample) and $T_s - T_\infty = 1\text{K}$, Ra is 1.42×10^4 , leading to $C_1 = 0.54$ and $C_2 = 0.25$. The temperature gradient of air near the sample surface (∇T_{air}) is now given by:

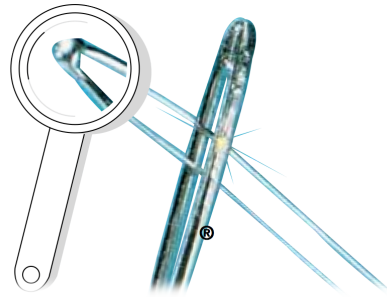
$$\nabla T_{air} = 928(T_s - T_\infty)^{1.25}, \text{ or } T_s - T(y) = 928(T_s - T_\infty)^{1.25} y, \quad (2.3)$$

where y is the vertical distance from the sample surface. Equation 2.3 provides insight on the size of the sensor required for an accurate measurement. For example, the distance from the sample surface required for $T(y) = 0.9T_s$ is $100 \mu\text{m}$ for $T_s - T_\infty = 1\text{K}$. In other words, the difference between the air and the sample temperatures is less than 10% within a boundary thickness of $100 \mu\text{m}$, allowing the negligible air convection with respect to the heat conduction between the sensor and the sample surface. The size of a sensor needs to be smaller than this boundary layer thickness in order to minimize air convection. It should be noted that the boundary layer thickness gets smaller as $T_s - T_\infty$ becomes larger as can be seen in Eq. 2.3, and one should use the minimum temperature gradient that still generates a measurable Seebeck voltage for accurate surface temperature measurement by a sensor with a certain size. For example, the sensor size should be smaller than $100 \mu\text{m}$, if a temperature gradient of 2Kmm^{-1} is measured by 1mm separated sensors, assuming the mean temperatures at the two sensor contact points to be T_∞ .

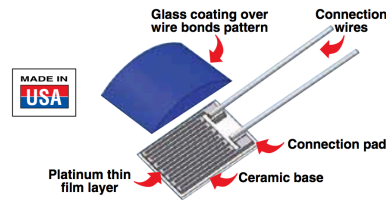
2.1.2 Type of temperature sensor

As discussed in the section 2.1.1, the size of a temperature sensor should be smaller than the boundary layer thickness ($\sim 100 \mu\text{m}$) in order to minimize error due to air convection. Figure 2.2 shows various types of temperature sensors such as a thermocouple, a resistance temperature detector (RTD), and a thermistor. While RDTs typically provide high accuracy and reliability, the size of commercially available RDTs (and thermistors) is typically larger than a few millimeters. This millimeter-range size makes the mass center of the RTD (or thermistor) far beyond the boundary layer, causing the temperature measured by these sensors to be

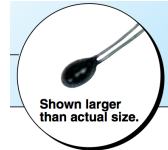
a – fine diameter thermocouple
(from 25 μm)



b – 0.8 mm thick RTD



c – 2.4 mm diameter thermistor



d

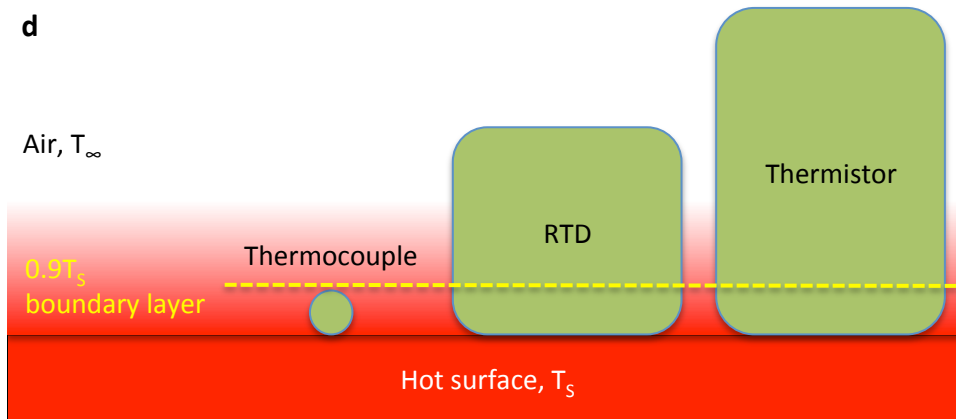


Figure 2.2 | Various types of sensors for steady-state temperature measurement. Examples of commercially available various sensors: **(a)** thermocouple **(b)** resistance temperature detector (RTD) **(c)** thermistor. Pictures are reproduced from Omega Inc., and correspond to the smallest size available for each type. **(d)** The effect of sensor size on the accuracy of the surface temperature measurement in air. For the RTD and thermistor, temperature data is sensitive to the attachment method.

considerably affected by air convection and heat conduction within the sensor. For this reason, while commercially available RTDs and thermistors are adequate for a thermal measurement in vacuum, for ambient use these sensors require both a specific attachment method to the measured surface and good thermal shielding (discussed in Section 2.3). One can fabricate a customized RTD that is several nanometers thin and sits directly on the sample surface, yet this requires considerable calibration efforts for each sample.

The size of a thermocouple junction (which acts as a temperature sensor) is limited by the thermocouple wire diameter, which can be as small as a few micrometers with reasonable strength for practical use. When a thermocouple wire of 50 μm diameter is used, the thermocouple junction is completely surrounded by air at 90% of the sample temperature for $T_s - T_\infty = 1\text{K}$, which allows an accurate temperature measurement regardless of air convection. It should be noted however that the required size of the thermocouple junction is smaller if the sample surface temperature differs by more than 1K from the ambient temperature, since the effect of convection becomes larger (Eq. 2.3). One should compromise between the signal strength of the Seebeck voltage (which needs large $T_s - T_\infty$) and the minimization of the heat leakage by air convection (which needs small $T_s - T_\infty$). In my work, a 25 μm diameter thermocouple (T-type) was mechanically attached to the sample for the temperature measurement, with $T_s - T_\infty$ usually on the order of 1 K. The Seebeck coefficient of nickel measured by this 25 μm thermocouple setup is $-19.95 \mu\text{V/K}$ at 297 K, consistent with literature values [45, 46].

2.2 Voltage measurement

The signal of the Seebeck voltage is typically very small, on the order of 10 μV , and cannot be increased significantly by increasing the applied temperature gradient due to the air convection problem discussed in Section 2.1. To measure this small signal, one should carefully account for the Seebeck voltages across the measurement lead wires, the contact effect between the sample and electrode, and the finite bias current of the voltmeter.

2.2.1 Circuitry with a low input bias current

Organic semiconductors typically have low carrier mobility, and consequently large electrical resistance over a wide range of carrier concentrations. The small input bias current of a voltmeter (i_b) could therefore result in a significant voltage drop across a sample. For example, when a sample with resistance $R_S = 10 \text{ k}\Omega$ is biased by a typical voltmeter with $i_b = 100 \text{ nA}$, the voltage drop across the sample can be as high as 1 mV , which is much larger than the expected Seebeck voltage (~ 10 to $100 \mu\text{V}$). To overcome these challenges, a voltage measurement setup that has good EM shielding and low input bias current (i.e., high input impedance) is needed. An

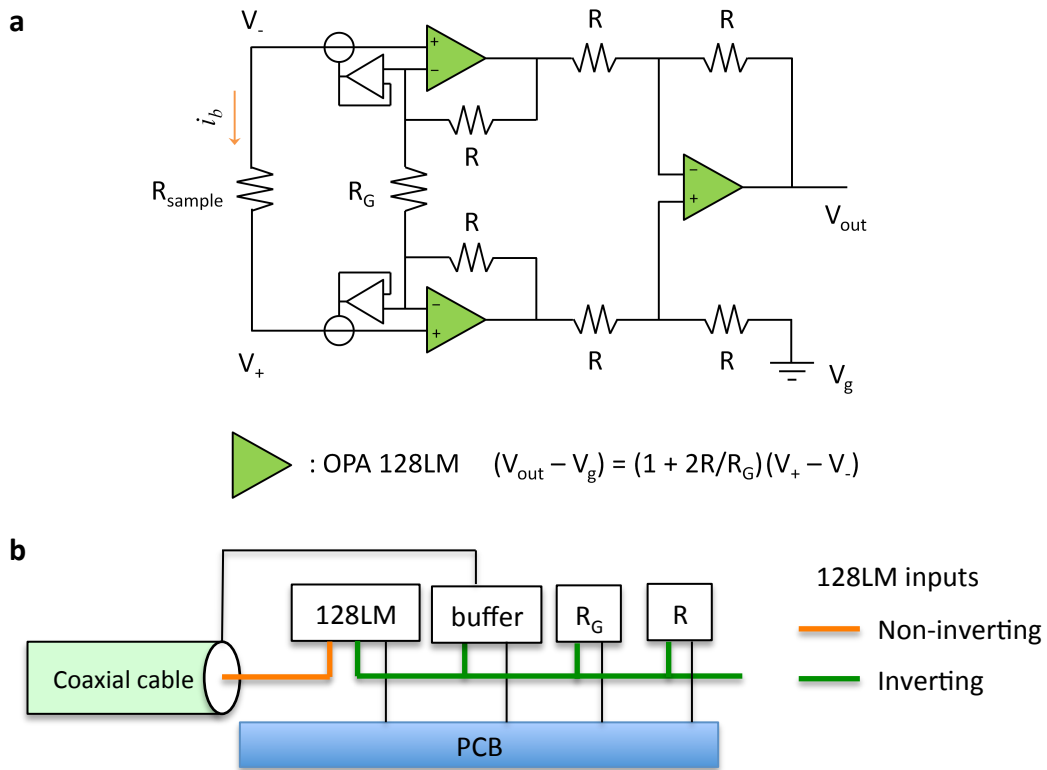


Figure 2.3 | Circuitry used for electrical measurement. (a) Low-noise instrumentation amplifier circuit designed for a femtoampere level input bias current. **(b)** Air connection used to isolate the input of the OPA 128LM from a printed circuit board (PCB).

instrumentation amplifier is a type of differential amplifier that uses the gate contact of the field effect transistor as an input lead and therefore provides a very low i_b , in addition to additional benefits of low DC offset and input noise. Figure 2.3a shows a circuit diagram of an instrumentation amplifier, where two operational amplifiers (OP amp A) are used to measure the differential voltage signal, and a third operational amplifier (OP amp B) is used as a buffer. For OP amp A, an ultralow i_b operational amplifier (Texas Instruments OPA128LM) was chosen: $i_b = 40$ fA, input offset current = 30 fA, and input offset voltage = 140 μ V. For this low level of i_b , even the pathway on a printed circuit board (PCB) can be more conductive than the input lead of the op amp; a typical resistivity of PCB 10^{10} $\Omega\cdot$ m can result in a leakage current of 1 pA between two PCB holes separated by 2.54 mm with a voltage difference of 1V.

Two possible methods can be applied to minimize the leakage current: minimizing the electric potential difference or maximizing the electrical resistance between the signal lead and the adjacent area. For the minimization of electric potential difference, a guard ring can be used to maintain the adjacent electrical potential very close to the input lead of OP amp A. This guard ring potential can extend to the shield of a coaxial cable and a coaxial probe to minimize noise (Fig. 2.1a). The buffer amplifier (OP amp C), the non-inverting input of which is connected to the inverting input of the OP amp A, can be used to handle the capacitance of the guard ring and coaxial cable shield. A Linear Technology LTC1151, which has a very low input offset voltage (0.5 μ V average, 5 μ V max), was chosen for OP amp C to maintain the potential of the guard ring and coaxial shield within ± 5 μ V from the signal voltage. For the maximization of electrical resistance between the signal lead and elsewhere, the “air connection” method can be applied, for which the input lead of the OP amp A is not connected to the PCB but instead is bent up into the air to make an electrical connection there. Since air is one of the best electrical insulators ($\sim 10^{16}$

to $10^{17} \Omega \cdot \text{m}$ at room temperature), this method provides excellent electric isolation. Figure 2.3b shows the air connection in the voltage circuit used in this work.

A good electromagnetic shield (EM shield) is needed for this low bias current measurement, since a small electric current induced by ambient light or a stray EM field may considerably affect the voltage signal. Figure 2.1a inset shows the Faraday cage used in my measurements, which is grounded during measurements.

2.2.2 Parasitic Seebeck voltages

The voltage measured by OP amp A is the sum of Seebeck voltages across the sample, the metal contacts, the voltage lead wires, and anything which experiences a temperature gradient. To isolate the Seebeck voltage that exists only across the sample, all parasitic Seebeck voltages must be subtracted from the measured value.

A common source of parasitic Seebeck voltages is the voltage leads, since the temperature gradient applied to the sample likewise causes a temperature gradient in the voltage leads (assuming that the inputs of the voltmeter are kept at the same ambient temperature). Figure 2.4 shows the overall temperature gradient and the associated Seebeck voltages during the Seebeck measurement. Since the temperature difference along the voltage leads is equal to the temperature difference along the sample between the leads but with the opposite sign (i.e., $\Delta T_{\text{sample}} = -\Delta T_{\text{lead}}$), the Seebeck voltage in the voltage leads (ΔV_{lead}) is given by:

$$\Delta V_{\text{lead}} = -S_{\text{lead}} \Delta T_{\text{lead}} = S_{\text{lead}} \Delta T_{\text{sample}} \quad (2.4a)$$

The measured voltage is the sum of the Seebeck voltages across the sample and voltage leads:

$$\Delta V_{measured} = -S_{sample} \Delta T_{sample} + S_{lead} \Delta T_{sample} \quad (2.4b)$$

and therefore the Seebeck coefficient of a sample is derived as:

$$S_{sample} = -\frac{\Delta V_{measured}}{\Delta T_{sample}} + S_{lead} \quad (2.4c)$$

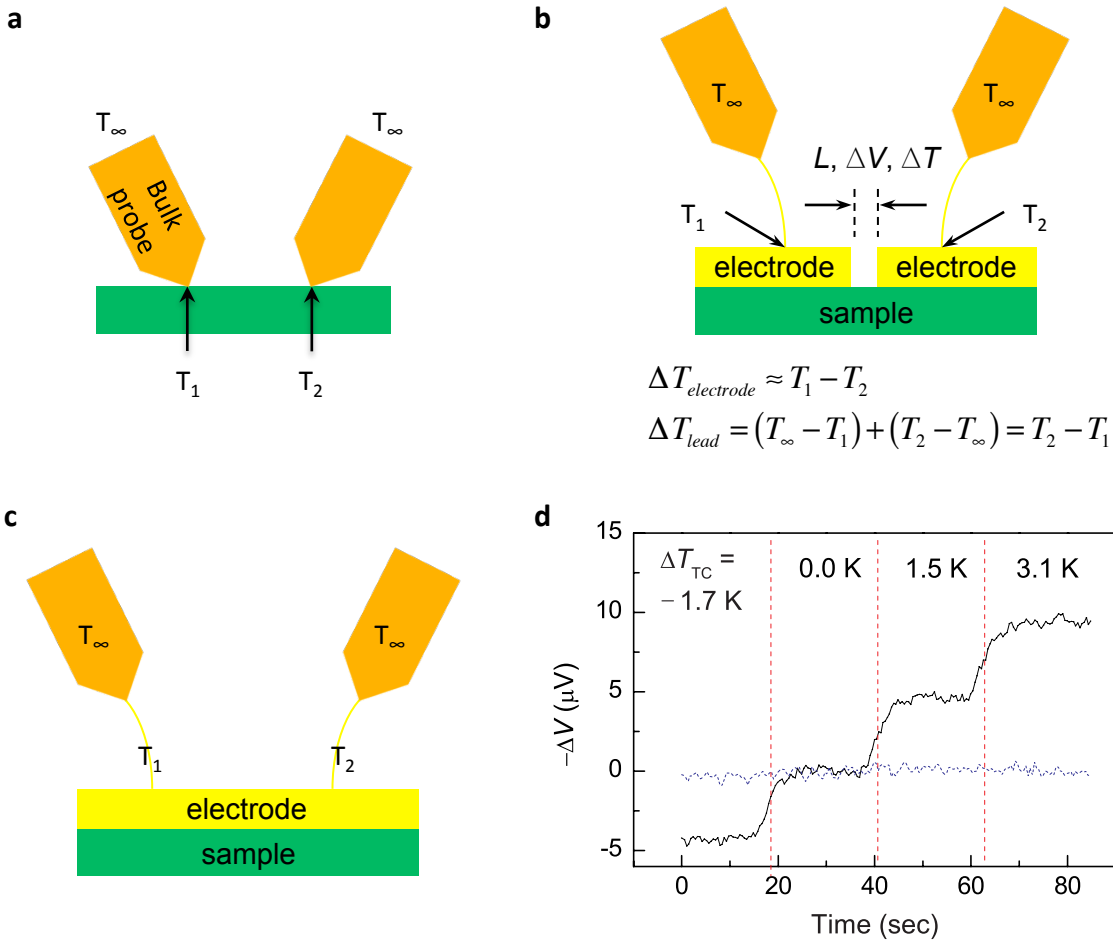


Figure 2.4 | Probe configuration for the Seebeck voltage measurement. (a-b) Seebeck voltage measurements using the direct probe contact **(a)** and the electrode contact with gold thin wires **(b)**. **(c)** The Seebeck voltage across a single electrode was measured for calibration; two thin gold wires are separated by the same distance used in configuration **b**. **(d)** Seebeck voltages for the **b** configuration (black solid line) and **c** configuration (blue dotted line) for various temperature differences ($\sim \Delta T_{TC}$).

Eq. 2.4 suggests that the Seebeck coefficient of a lead wire should be added to a measured Seebeck coefficient ($S_{measured} = -\Delta V_{measured}/\Delta T_{sample}$). It should be noted that the Eq. 2.4 is valid when the two inputs of the voltmeter are maintained at the same temperature, which is true in most cases.

When electrodes on the sample are used, the additional contributions of the electrodes to $\Delta V_{measured}$ should be considered. Figure 2.4b illustrates a Seebeck measurement using thin metal films as electrodes. In this case, the measured voltage is now the sum of the Seebeck voltages along the sample, electrodes, and voltage leads:

$$\Delta V_{measured} = -S_{sample}\Delta T_{sample} - S_{electrode}\Delta T_{electrode} + S_{lead}(\Delta T_{sample} + \Delta T_{electrode}). \quad (2.5)$$

As can be seen in Eq. 2.5, it is hard to derive the precise Seebeck coefficient of a sample directly from a measured voltage ($\Delta V_{measured}$) when temperature gradients exist not only across the voltage leads but also across electrodes. When the electrodes are made of the same metal as the voltage leads, however, Eq. 2.5 can be simplified and becomes equal to Eq. 2.4b. However, in many practical measurements, the voltage path consists of several different metals, needing a further calibration procedure. For calibration, absent-sample configuration (Fig. 2.4c) can be used, and one can deduce the sum of parasitic Seebeck voltages due to electrodes and voltage leads.

A minimal parasitic Seebeck voltage from voltage leads and electrodes is preferred for a reliable measurement. Figure 2.4b shows a setup in which very thin gold wires (diameter: 25 μm , length: 25 mm, Fig. 2.1a) are used between the electrodes and bulk voltage probes. Since the thermal resistances of the thin gold wires are very large, the entire temperature difference that occurs in the sample and electrodes between the points where the gold wires contact the electrodes

likewise occurs within the thin gold wires themselves. The Seebeck voltages along the thin gold wires and across the gold electrodes therefore mostly cancel each other out. It should be noted however that the cancellation of the electrode Seebeck voltage is not complete since part of the temperature difference between the probe contact points occurs across the sample, which has a different Seebeck coefficient than gold. Still, the use of thin gold wires minimizes the contributions of the gold electrodes in the voltage measurement. Figure 2.4d plots the measured Seebeck voltage when two thin gold wires contact the same electrode (Fig. 2.4c), which is representative of the sample having infinitesimal width. No significant Seebeck voltage was observed in this case, indicating the cancellation of Seebeck voltages across the electrodes and voltage leads. This calibration for the minimization of parasitic Seebeck voltages ensures that the measured voltage arises primarily from the Seebeck voltage across the sample.

2.2.3 Integral Seebeck measurement method

There are two main methods for Seebeck measurement: first, a differential method in which the Seebeck voltage is measured along the direction of an applied temperature gradient (Fig. 2.1a); second, an integral method in which the sum of sample and reference material Seebeck voltages is measured at the same temperature point (Fig. 2.1b). As shown in Figs. 2.1b and 2.1c, a sample and two reference materials (M1 and M2) are electrically and thermally shorted at junction A, while they are thermally but not electrically shorted at junction B (i.e., a three wire thermocouple). When a temperature difference is created between junctions A and B (ΔT_{AB}), it induces different Seebeck voltages (ΔV_{sample} , ΔV_{M1} , ΔV_{M2}) within the three materials (i.e., sample, M1 and M2) depending on their individual Seebeck coefficients. Since ΔT_{AB} can be derived by

the known Seebeck coefficients of M1 and M2 (i.e., the thermocouple made by M1 and M2), the sample Seebeck coefficient can be derived by:

$$S_{sample} = -\frac{(\Delta V_{sample} - \Delta V_{M1})}{\Delta T_{AB}} + S_{M1}, \quad (2.6a)$$

where ΔT_{AB} is calculated based on the known Seebeck coefficients of M1 (S_{M1}) and M2 (S_{M2}):

$$\Delta T_{AB} = -\frac{(\Delta V_{M1} - \Delta V_{M2})}{(S_{M1} - S_{M2})}. \quad (2.6b)$$

The benefit of the integral method is that the sum of Seebeck voltages can be probed at spots with the same temperature, enabling the measured voltage to be directly linked to the Seebeck voltage across the sample. In the differential method, temperature gradients at other parts along the voltage path are inevitable and must be accounted for, since Seebeck voltages are probed at different temperatures.

In my integral Seebeck setup (Fig. 2.1b), a thin sample sheet (e.g., nickel) was fixed between a small copper fixture (8mm width \times 32mm length \times 3mm thickness, gold plated) and the copper temperature stage (gold plated). The temperature of the copper temperature stage was controlled by a Peltier cooler beneath. For the fixtures shown in Fig. 2.1 that require an isothermal condition, brass screws were used due to their high thermal conductivity ($\sim 110 \text{ W m}^{-1}\text{K}^{-1}$) and elastic modulus (120 GPa). Two copper stages were electrically isolated from the ground and used as an electrode for the integral Seebeck measurement; they were grounded when a sample on an electrically insulating substrate was tested using the differential Seebeck measurement method. At junction A, M1 and M2 wires were high-temperature soldered to a copper washer which was mechanically fixed by a brass screw on the copper fixture; at junction B, each M1 and

M2 wire was soldered to a separate metallized pad on a BeO chip (Lakeshore HSC-4), the metallized backside of which was thermally brazed to the copper fixture (filler metal: indium).

While I built both differential and integral setups for Seebeck measurements, most data in this thesis were measured by the differential setup, since the integral setup requires a relatively large sample. A comparison between the two different setups was done by measuring the Seebeck coefficient of nickel at 297 K to confirm the reliability of the data used in this work; S_{Nickel} measured by the differential setup was $-19.95 \mu\text{V/K}$, and S_{Nickel} measured by the integral setup was $-20.03 \mu\text{V/K}$. Note that the thermocouple in the differential setup was mechanically attached while the thermocouples made by M1 and M2 were high-temperature soldered; this indicates that the temperature read by the mechanically attached thermocouple is accurate when its size is smaller than the $100 \mu\text{m}$ boundary layer thickness (Section 2.1.1).

2.2.4 Energy barrier at the electrode

The electrode metal, which forms the interface with the sample (in this case, an OSC), should be carefully chosen to minimize the energy barrier at the metal-OSC interface. This energy barrier can filter out charge carriers at low energies, causing the measured Seebeck coefficient to represent not only the bulk sample but also include a contribution from the interface. Figure 2.5 illustrates the deviation of a measured Seebeck coefficient from the bulk value due to a built-in potential at the interface. To remove this energy barrier, the work function of the contact metal should be matched to the average energy level of conducting charge carriers. Many hole-transporting OSCs have their highest occupied molecular orbital (HOMO) level near 5.0 eV, which makes noble metals suitable for an electrode material due to their large work function. For example, a gold electrode forms a good Ohmic interface with pentacene and poly(3,4-

ethylenedioxythiophene):poly(stylenesulfonate) (PEDOT:PSS), which have HOMO levels at 4.9 and 5.0 eV, respectively. Additionally, noble metals are not degraded in ambient conditions, providing a long-term reliable Ohmic contact. In this work, gold was used for electrodes, which forms the interface with OSC samples, for this reason.

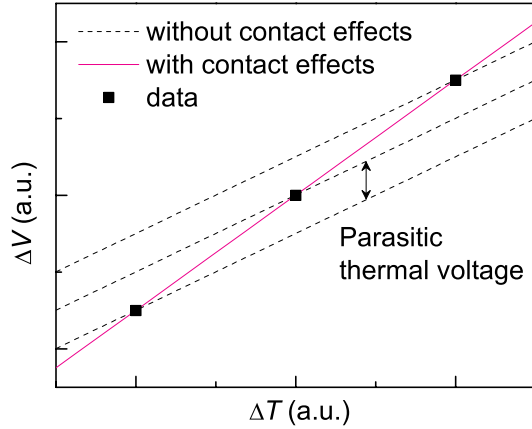


Figure 2.5 | Illustration of the effect of a contact built-in potential on the measured Seebeck coefficient.

2.2.5 Differential technique of varying sample length

Measuring the Seebeck voltages in samples with various lengths is a powerful tool to remove many possible error sources described above. Since only the length of a sample is varied during the measurement, the contact effect (2.2.4) and parasitic voltages along voltage paths (2.2.2) can be subtracted out by comparing the signals of samples with various lengths. It is similar to a differential electrical conductivity measurement, by which the contact resistance is extracted [47]. Figure 2.6 shows a plot of the Seebeck coefficient (S) and electrical conductivity (σ) measured in a sample of PEDOT:PSS as a function of the sample length. In the σ plot, the y -intercept is nearly zero, indicating good Ohmic contacts between the gold electrodes and OSC. In the S plot, the Seebeck voltage increases linearly with the sample length, indicating negligible

parasitic Seebeck voltages during the measurement. Note that the data plotted in Fig. 2.6 was taken by carefully following all of the practical tips described above.

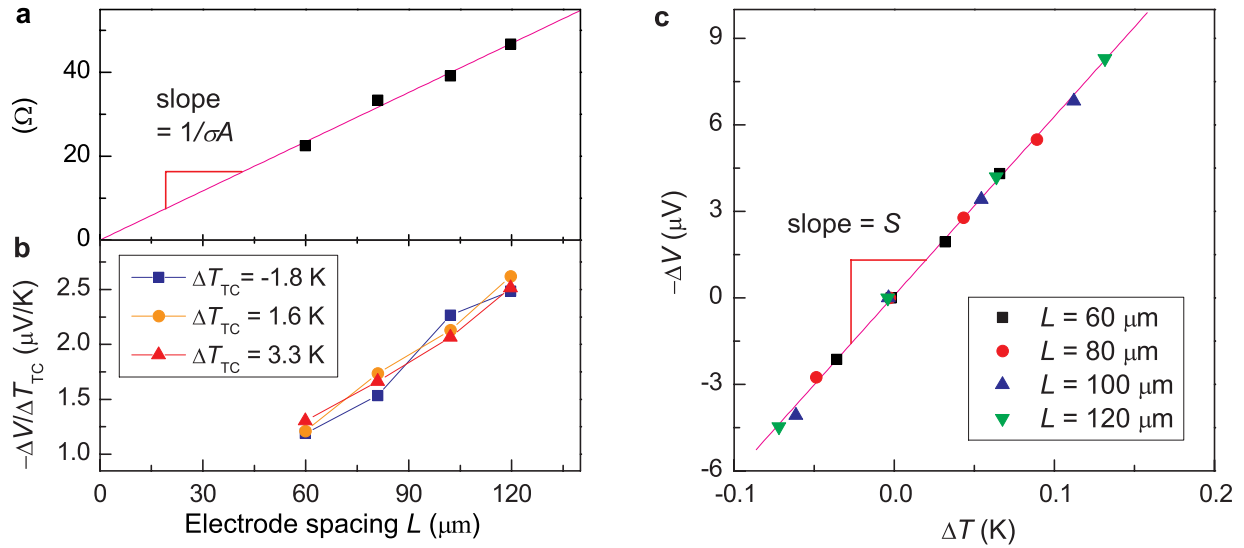


Figure 2.6 | Differential techniques used for measurements of S and σ . (a-b) Measured electrical resistance and normalized thermal voltage (i.e., thermal voltage across the sample (ΔV) divided by the temperature difference between the two thermocouples (ΔT_{TC})) as a function of the sample length L . Here, the sample is PEDOT:PSS. (c) ΔV across samples of various lengths versus the temperature differences across the samples (ΔT).

2.3 Stable temperature gradient

A stable temperature gradient is a prerequisite for reliable temperature and Seebeck measurements. Since a Seebeck voltage and a temperature difference must be measured along the same direction, the 1-dimensional (1D) temperature gradient is preferred. A typical way to achieve a 1D temperature gradient is to use two Peltier modules: one as a heater and the other as a cooler. Several useful tips to achieve a stable temperature gradient in this way are discussed below.

2.3.1 Fast response temperature sensor

Peltier modules are generally driven by a feedback temperature controller which uses the deviation between measured and set temperatures as a feedback signal. This feedback controller cannot produce a stable temperature if the time lag of the temperature sensor is too large. For this reason, not only the heat capacity of the sensor but also any other heat transfers other than that between the sensor and Peltier module should be minimized. A sensor with a minimum size should be used so that the heat capacity is small, and good thermal shielding is required to prevent any heat leakages from the sensor. As shown in Fig. 2.1b, a thermistor with 2 mm diameter is embedded deeply into the copper temperature stage, which is attached to the cold side of a Peltier module using thermal grease. This deep localization of the thermistor (5mm depth) leads to excellent thermal shielding and hence fast sensor response time.

2.3.2 Liquid-cooled heat sink

A Peltier module is a heat pump that does not (by itself) maintain a given temperature but instead removes (or provides) a certain amount of heat at a given power. This means that the temperature at the cold side of a Peltier module changes linearly with its hot side temperature, and therefore the temperature fluctuation at the hot side should be minimized. Anchoring the hot side of a Peltier module with a well-designed heat sink that has very low thermal resistance can provide a constant temperature at the hot side. The thermal resistance of a heat sink cooled by natural air convection is typically $10\text{ }^{\circ}\text{C}/\text{W}$, which is too large compared to the typical power used by a Peltier module ($0.1 - 1\text{ W}$). Forced airflow can be used to reduce this large thermal resistance to $0.1\text{ }^{\circ}\text{C}/\text{W}$, but turbulent air caused by a cooling fan can lead to a significant error in temperature measurement as discussed in Section 2.1.1. A liquid-cooled copper heat sink (often called a

“water block”) has a thermal resistance typically less than 0.05 °C/W with water as the coolant. Moreover, liquid cooling causes no unwanted turbulent airflow near the sample, making it suitable for precise thermoelectric measurement. The flow rate of liquid should be chosen to minimize both the thermal resistance of the water block and any undesired vibrational effects on the measurement caused by liquid flow. Note that stainless steel screws and nylon washers were used to fix the copper temperature stage in order to thermally and electrically isolate it from the copper-based water block (Fig. 2.1).

2.4 Thermal conductivity measurement by the 3ω method

The precise measurement of thermal conductivity is critical to the characterization of thermoelectric materials, since it is the one of three quantities composing the thermoelectric figure-of-merit (ZT). Thermal conductivity is also an essential parameter for other OSC-based devices such as OLEDs and OFETs, since it bears on device performance and long-term reliability. Furthermore, thermal conductivity is itself a figure-of-merit in thermal interface material applications.

Experimental methods used for thermal conductivity measurement vary depending on the sample size and desired temperature range. Organic semiconductors are typically fabricated as a thin film on a substrate, for which conventional methods for bulky samples (such as steady-state heat flux measurements [48]) are not practical. The 3ω method is a reliable and powerful way to measure the thermal conductivity of a thin film down to several nanometers thickness [49, 50]. For thin films, heat leakages by air convection and radiation are negligible compared with heat conduction to the substrate, making the 3ω method ideal for thermal conductivity measurements

in air. Compared to other thin film thermal conductivity measurement techniques such as time-domain thermoreflectance [51], the 3ω method has a relatively cheap setup and is particularly useful for organic thin films, which can be easily destroyed by laser irradiation. Since the 3ω method uses an oscillating heat source, the thermal penetration depth can be designed to be smaller than the substrate thickness, making the thermal boundary condition at the substrate bottom have no effect on the measurement accuracy. Additionally, the 3ω method can be used to measure the anisotropy of the thermal conductivity [52], and hence is particularly valuable for measuring the in-plane thermal conductivity of a thin organic film.

2.4.1 Theory of the 3ω method

The 3ω method uses a thin metal line as both a resistive heater and temperature sensor (Fig. 2.7). The metal line is driven by an alternating current (AC) at the angular frequency of ω , which generates Joule heating at a frequency of 2ω ($Q_H = i_{AC,\omega}^2 R$, where $i_{AC,\omega}$ is the alternating current applied at frequency ω to the metal line and R is the electric resistance of the metal line). Since R is linearly proportional to the metal line temperature within a small temperature range, a small AC signal in R is caused which has a frequency equal to that of the Joule heating (i.e., $R = R_0 + \delta R_{2\omega}$). A voltage signal at 3ω arises due to the ω current modulation and 2ω change in metal line resistance ($V_{3\omega} = i_{AC,\omega} \times \delta R_{2\omega}$).

The 3rd harmonic voltage ($V_{3\omega}$) is directly linked to the change in metal line temperature (ΔT), which can be derived by [53]:

$$\Delta T = 2R \frac{dT}{dR} \frac{V_{3\omega}}{V_{\omega}}, \quad (2.7)$$

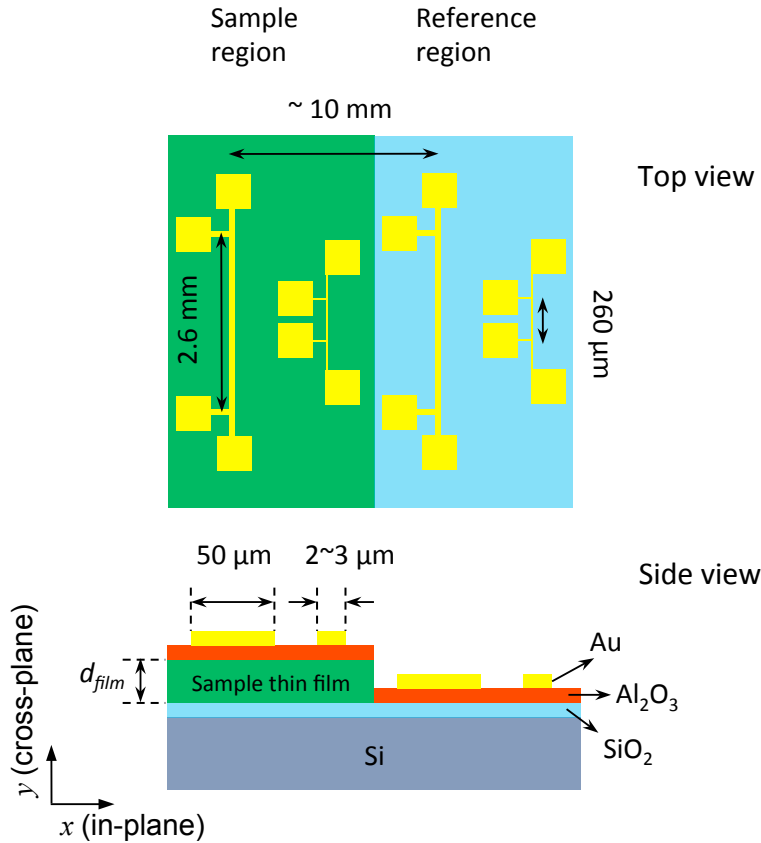


Figure 2.7 | Sample configuration for the 3ω measurement. Wide and the narrow metal lines are deposited on both the sample region and the reference region. The thickness of the sample thin film (d_{film}) is chosen to be much smaller than the $50\ \mu\text{m}$ heater line width (used for the cross-plane κ measurement), and to be on the order of $2 - 3\ \mu\text{m}$ when the in-plane κ needs to be measured. A thin Al_2O_3 layer is used when an electrically conductive sample film is tested. Thin SiO_2 ($100\ \text{nm}$) is used to electrically isolate the heater line from the conductive bulk silicon substrate (which was used rather than an undoped silicon substrate since it is much less expensive).

where dR/RdT is the temperature coefficient of electrical resistance in the metal line and V_ω is the voltage oscillation due to the applied alternating current at ω ($V_\omega = i_{AC,\omega} \times R$). Assuming very large κ in the metal line with respect to the sample and negligible thermal resistance at the metal line-sample interface, ΔT is equal to the temperature rise within the sample, and therefore directly represents its thermal properties. Based on Fourier's law of heat transfer, the analytical solution for ΔT for a given sample thermal conductivity and known applied power can be derived, to

which the ΔT derived from measurement by Eq. 2.7 is fit to extract the thermal conductivity of the sample.

The analytical solution for ΔT appearing in Eq. 2.7 can also be derived for the general case of a multilayer structure in which each layer has anisotropic thermal properties. The temperature rise at the top surface (ΔT) of a sample due to an applied heat power (Q_H) is given by [49]:

$$\Delta T = -\frac{Q_H}{\pi l_M \kappa_{y1}} \int_0^\infty \frac{1}{A_1 B_1} \frac{\sin\left(\frac{w}{2}\gamma\right)}{\left(\frac{w}{2}\gamma\right)^2} d\gamma, \quad (2.8a)$$

where

$$A_{i-1} = \frac{A_i \frac{\kappa_{y,i} B_i}{\kappa_{y,i-1} B_{i-1}} \tanh(B_{i-1} d_{i-1})}{1 - A_i \frac{\kappa_{y,i} B_i}{\kappa_{y,i-1} B_{i-1}} \tanh(B_{i-1} d_{i-1})}, \quad i = 2, 3, \dots, n \quad (2.8b)$$

$$B_i = \left(\frac{\kappa_{x,i}}{\kappa_{y,i}} \gamma^2 + i \frac{2\omega}{D_{y,i}} \right)^{1/2}. \quad (2.8c)$$

In Eq. 2.8, l_M is the length of the metal line, n is the total number of layers, i denotes the i^{th} layer from the surface (i.e., $i = n$ for the substrate), the subscript y represents the perpendicular axis with respect to the plane surface (x is the parallel axis), w is the metal line width, κ is the thermal conductivity, and D is the thermal diffusivity. The boundary condition at the bottom of the substrate determines the constant A_n : for an adiabatic boundary condition, $A_n = -\tanh(B_n d_n)$, while for an isothermal boundary condition, $A_n = -1/\tanh(B_n d_n)$. For a semi-infinite substrate in which the substrate thickness (d_n) is much larger than its thermal penetration depth ($\lambda_n =$

$\sqrt{D_n/2\omega}$), the heat produced by the AC power input does not reach the bottom of the substrate, and A_n becomes a constant (-1). While Eq. 2.8 provides an expression for the general case, its fit to experimentally measured ΔT is not definite, since the thermal diffusivities of the various layers are also free variables (unless they are known beforehand).

One can simplify Eq. 2.8 for a single layer with isotropic thermal properties and semi-infinite thickness ($\lambda \ll d$) on which the metal line has a negligible width ($w \ll \lambda$) [53]:

$$\begin{aligned} \Delta T &= -\frac{Q_H}{\pi l_M \kappa} \left(0.5 \ln \left\{ \frac{D}{(w/2)^2} \right\} - 0.5 \ln \omega + \text{Constant} \right) - i \left(\frac{Q_H}{4l_M \kappa} \right) \\ &= \frac{Q_H}{\pi l_M \kappa} f_{linear}(\ln \omega). \end{aligned} \quad (2.9)$$

Equation 2.9 indicates that $d(\Delta T)/d(\ln \omega)$ varies only according to the thermal conductivity of the single layer (e.g., substrate), making the fit of Eq. 2.9 definite. It should be noted however that the assumptions of semi-infinite thickness and negligible line width limit the use of Eq. 2.8 [49].

The layer for which the thermal conductivity is to be measured is a thin film on a substrate. For a sample thickness much smaller than w , the heat transfer from the metal line to the substrate via the thin film is quasi 1-dimensional, and the additional temperature rise across the thin film can be calculated by Fourier's conduction law in 1D. The total temperature rise due to both the substrate (Eq. 2.9) and thin sample layer is:

$$\Delta T_{total} = \Delta T_{substrate} + \Delta T_{film} = \frac{Q_H}{\pi l_M \kappa_{substrate}} f_{linear}(\ln \omega) - \frac{Q_H d_{film}}{w l_M \kappa_{film}}. \quad (2.10)$$

In Eq. 2.10, $\Delta T_{substrate}$ may include the temperature rise not only in the substrate but also in all layers that may be present in addition to the thin sample layer. For instance, $\Delta T_{substrate}$ for a silicon substrate capped by 100 nm of SiO₂ represents the temperature rise due to both Si and SiO₂.

2.4.2 Differential 3 ω method

From Eq. 2.10, one can easily see that subtracting $\Delta T_{substrate}$ from ΔT_{total} produces a quantity that depends only on the thermal conductivity of the thin sample layer. For thin film samples with different thicknesses (d_{film}), ΔT_{total} is expressed by:

$$\Delta T_{total,1} = \Delta T_{substrate} - \frac{Q_H d_{film,1}}{w l_M \kappa_{film}}, \quad (2.11a)$$

$$\Delta T_{total,2} = \Delta T_{substrate} - \frac{Q_H d_{film,2}}{w l_M \kappa_{film}}, \quad (2.11b)$$

with a difference of:

$$\Delta T_{total,1} - \Delta T_{total,2} = - \frac{Q_H (d_{film,1} - d_{film,2})}{w l_M \kappa_{film}}. \quad (2.11c)$$

The thermal conductivity of the thin sample layer is therefore given by:

$$\kappa_{film} = - \frac{Q_H (d_{film,1} - d_{film,2})}{w l_M (\Delta T_{total,1} - \Delta T_{total,2})}. \quad (2.11d)$$

Equations 2.11c and 2.11d are the basis of the differential 3 ω method. Since all experimental parameters other than the sample layer thickness are kept the same, the temperature changes due

to $\Delta T_{substrate}$ and unwanted parasitic effects such as air convection can be easily removed. The thermal conductivity data shown in this thesis were measured using this differential 3ω method.

2.4.3 Calibration and measurement setup

The thermal conductivity measurement by the differential 3ω method consists of two steps: first, the total temperature rise is derived from the ratio of measured $V_{3\omega}$ and $V_{1\omega}$ (Eq. 2.7), and second, the temperature rise only across the sample layer is extracted by Eq. 2.11c. The uncertainty in the each step should be minimized.

Precise information regarding the metal line width, length, and temperature coefficient of resistance is needed to derive the temperature rise of the metal line from measured $V_{3\omega}$ and $V_{1\omega}$. The accuracy of the metal line geometry is directly related to the accuracy of the shadow mask used to fabricate it. A precision chemical etching process can fabricate a shadow mask with an accuracy of $\pm 1\mu\text{m}$. A large metal line width can therefore be used to reduce the impact of this width uncertainty, as long as it does not lead to considerable air convection. In this work, the metal line was patterned to have $50\mu\text{m}$ width with a standard deviation better than $\pm 3\%$, for which the widths of 50 metal lines were measured by an optical microscope. The widths of the narrow heater lines used for in-plane thermal conductivity measurements were measured by scanning electron microscopy, as they have a width on the order of $1\mu\text{m}$.

The temperature coefficient of resistance (TCR) of the metal line is also critical to accurate data extraction by Eq. 2.7 Both the chemical composition and morphology of the metal line determine its TCR. Regarding the chemical composition, a pure noble metal (e.g., Au, Pt) should be used to

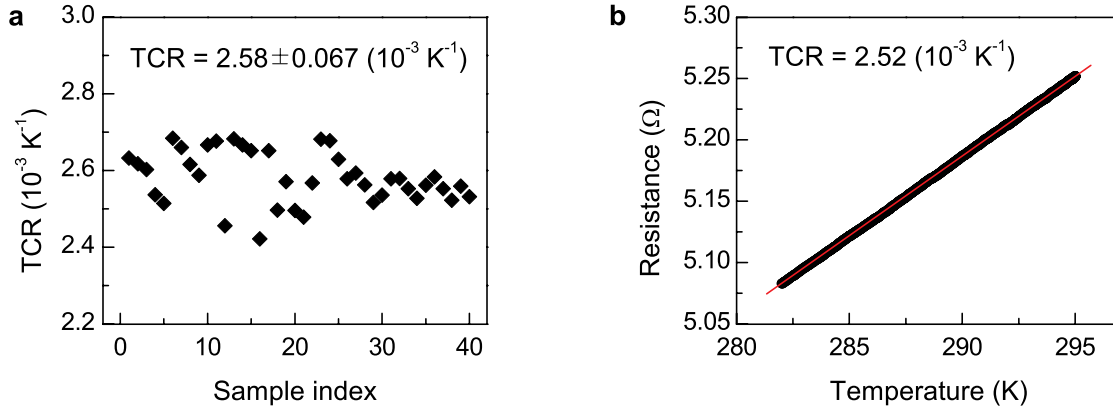


Figure 2.8 | Temperature coefficient of resistance (TCR) of the metal line heater. (a) TCR measured in 40 heater lines with an average value of $2.58 \pm 0.067 (10^{-3} \text{ K}^{-1})$ at room temperature. **(b)** Resistance measured from 282 to 295 K (symbols), which was used to obtain each TCR value. Data courtesy of Kejia Zhang (University of Michigan).

prevent oxidation in air that can alter the TCR. Regarding the effect of metal morphology on TCR, it should be measured whenever a new deposition system is used or the properties of the underlying surface are significantly different. Figure 2.8 shows the TCR measured in 40 gold lines deposited by the same evaporator under the same deposition conditions. It should be noted that the magnitude of the TCR measured in the gold lines (0.00258 K^{-1}) is considerably smaller than the bulk value (0.0034 K^{-1}), since the effect of grain boundaries on electrical transport becomes large in a thin metal film [54].

The differential 3ω method (Eq. 2.10c) assumes a uniform $\Delta T_{substrate}$, which bears on its reliability. Possible factors that can lead to a discrepancy in $\Delta T_{substrate}$ are variations in thermal properties within the substrate, deviations in thickness of any other thin layers within the sample (e.g., oxide layer, buffer layer), and different boundary conditions at the bottom of the substrate. In order to reduce the influence of these factors on the overall accuracy of the differential 3ω method, the magnitude of $\Delta T_{substrate}$ with respect to ΔT_{film} should be minimized (i.e., $\kappa_{substrate}/\kappa_{film} \gg 1$). Therefore, a thermally conductive (large $\kappa_{substrate}/\kappa_{film}$) single crystal (uniform $\Delta T_{substrate}$)

substrate should be used for the differential 3ω measurement; the thin oxide layer, needed for electrical isolation, should also have a uniform thickness. To further minimize the variation of $\Delta T_{substrate}$, the two metal lines for $d_{film,1}$ and $d_{film,2}$ should be deposited at the same time (to yield the same TCR in the two metal lines) and located as close as possible to minimize the effects of any substrate non-uniformity; the reference and the sample metal lines were typically separated by 10 mm in this thesis, as shown in Fig. 2.7. Additionally, the AC frequency range should be carefully chosen to make the heat penetration depth smaller than the substrate thickness; otherwise, the boundary condition at the substrate bottom must be identical for all measurements.

2.4.4 Circuitry for the 3ω method

During a differential 3ω measurement, $V_{3\omega}$ and $V_{1\omega}$ are converted to the applied heat flux and the generated temperature gradient. Since change in the metal line resistance is small, $V_{3\omega}$ is a small signal. This small $V_{3\omega}$ signal can be precisely measured using a lock-in amplifier (SR830, Stanford Research Systems), which can generate the AC signal at ω and collect the phase-locked signal at 3ω . When the output current of the SR830 is not large enough to produce the desired electric power, a voltage-to-current amplifier can be inserted between SR830 and the metal line.

2.4.5 3ω method for measuring the anisotropic thermal conductivity

The orientation of molecules strongly affects the electrical properties of OSCs [9, 10], and many organic devices including thermoelectric device are designed to operate in the direction of large carrier mobility. Since the thermal conductivity also tends to be larger in the direction of the

molecular alignment [41, 42, 55], anisotropy in thermal conductivity should be addressed when characterizing a thermoelectric material.

The 3ω method can measure anisotropy in thermal conductivity by measuring the temperature rise of a metal line with a width comparable to the sample layer thickness. In Equation 2.10, the additional temperature rise due to the thin sample layer is calculated neglecting the in-plane heat transfer, a good approximation for a film thickness much smaller than the metal line width. However, when the metal line width is comparable to the sample layer thickness, the contribution of the in-plane heat transfer to total heat transfer becomes significant. For this case, both the cross-plane and in-plane modes of heat transfer affect the temperature rise of the metal line; the magnitude of temperature rise for the narrow metal line is smaller than that for the wide metal line due to the additional in-plane heat transfer (i.e., lateral heat spreading). The ratio of the temperature rises in the narrow metal line and in the wide metal line is given by [52]:

$$\frac{\Delta T_{2D}}{\Delta T_{1D}} = \left(\frac{\kappa_x}{\kappa_y} \right)^{1/2} \frac{w_{narrow}}{d_f} \frac{K(\xi)}{2K'(\xi)}, \quad (2.12)$$

where x and y are the in-plane and cross-plane axes, respectively, and w_{narrow} is the width of the narrow metal line. To account the significant difference in the metal line area that determines the heat flux, ΔT_{2D} (narrow metal line) and ΔT_{1D} (wide metal line) in Eq 2.12 are normalized by a given heat flux. $K(\xi)$ and $K'(\xi)$ are the complete and complementary complete elliptical integrals of the first kind, and ξ is given by [52]:

$$\frac{1}{\xi} = \cosh \left[\frac{\pi}{4} \frac{w_{narrow}}{d_f} \left(\frac{\kappa_x}{\kappa_y} \right)^{1/2} \right]. \quad (2.13)$$

ΔT_{2D} and ΔT_{1D} can be experimentally determined using Eq. 2.7, and the anisotropy in the thermal conductivity can then be extracted by fitting Eq. 2.12 to the ratio of ΔT_{2D} and ΔT_{1D} (Fig. 2.9).

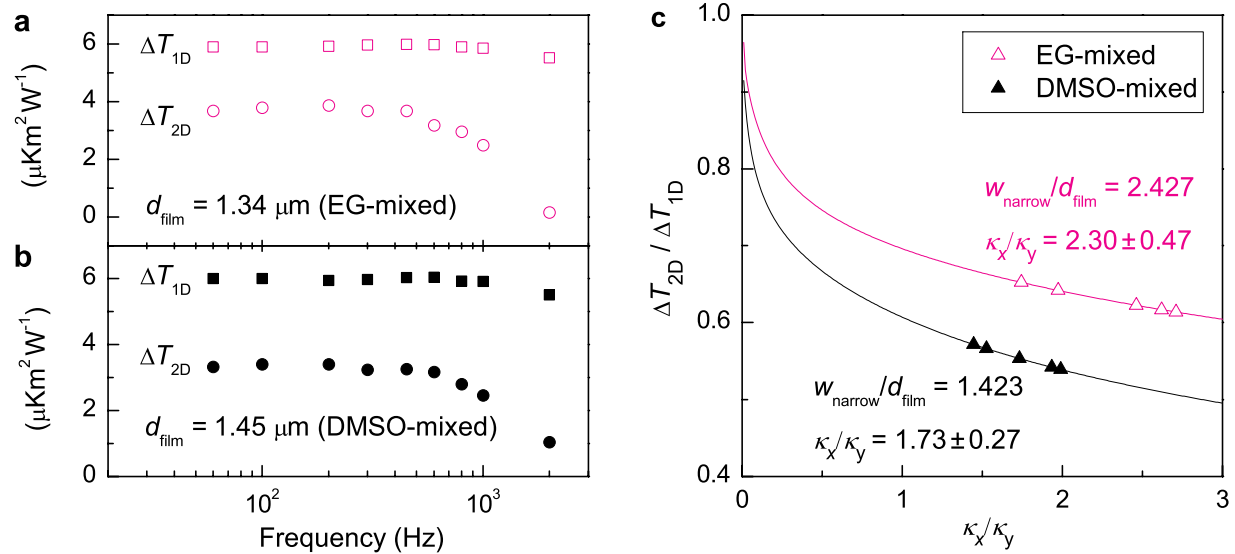


Figure 2.9 | Anisotropic ratio of the thermal conductivity. (a-b) Normalized temperature rise in the narrow line and the wide line for EG-mixed (a) and DMSO-mixed (b) PEDOT:PSS; materials plotted here are discussed in Chapter 5. (c) A fit of Eq. 2.12 to the measured $\Delta T_{2D} / \Delta T_{1D}$, from which the anisotropic ratio κ_x / κ_y is obtained.

Chapter 3

Charge carrier transport in organic semiconductors

Improving electronic device performance often involves the art of increasing charge carrier mobility (μ). For instance, μ itself is a device figure-of-merit for field-effect transistors, larger μ leads to higher recombination rate in light-emitting diodes, and the quantum efficiency in photovoltaic devices strongly depends on μ [56]. Even in thermoelectric devices, in which higher mobility generally results in lower Seebeck coefficient (S) ($S \sim$ effective mass of charge carriers in ISCs, and S decreases for less localized carriers in OSCs), the thermoelectric power factor ($S^2\sigma$) generally increases with carrier mobility [57]. Therefore, a primary requirement for high performance organic devices is high charge carrier mobility, the achievement of which requires a good understanding of carrier transport.

The structure of organic solids is fundamentally different from that of inorganic semiconductors (ISCs), leading to different characteristics of charge carrier transport. Whereas the electronic wavefunction is fully extended and its coherence is limited by various scattering mechanisms in ISCs, long-range order is absent in organic semiconductors (OSCs) either due to crystal imperfections or intermolecular thermal fluctuations. This absence of long-range order leads to the localization of charge carriers, the degree of which should be quantitatively addressed in order to properly describe carrier transport.

This chapter presents a theoretical model and methodology that can quantitatively determine the carrier localization length [7]. A survey of many literature data based on this methodology provides insight on recent developments in OSCs.

3.1 Transport of localized charge carriers

Charge carriers in OSCs are spatially localized due to several reasons as discussed below. For a localized carrier, external energy is needed to escape the localized state. A theoretical description for the resulting charge carrier tunneling process is hopping transport. Many traditional hopping transport models were developed when OSCs being studied were primarily amorphous, and the assumption of strong localization fit the experimental data. However, this assumption of strong localization has failed recently in several OSCs with high crystallinity, and the nature of carrier localization in these crystalline OSCs is now under academic debate. Later in this chapter, I develop a charge transport model for the Seebeck coefficient in OSCs, and show how fits of data to this model suggest that carrier localization (and hopping transport) remains valid even in crystalline OSCs due to dynamic disorder.

3.1.1 Carrier localization in disordered materials (Anderson localization)

The fundamental basis of band transport is the extended charge carrier wavefunction. The spatial wavefunction of a charge carrier in a solid is given by the time-independent Schrödinger equation:

$$E\Psi(\mathbf{r}) = -\frac{\hbar^2}{2m_e}\nabla^2\Psi(\mathbf{r}) + V(\mathbf{r})\Psi(\mathbf{r}), \quad (3.1)$$

where E is the energy scalar, \hbar is the reduced Plank constant, m_e is the electron mass, and $\Psi(\mathbf{r})$ is the spatial wavefunction at the coordinate \mathbf{r} . $V(\mathbf{r})$ describes the Coulomb interaction between the charge carrier and the lattice, and its shape represents the crystal structure of a solid. For a perfect crystal, which makes $V(\mathbf{r})$ periodic, $\Psi(\mathbf{r})$ can be expressed by a Bloch wave which follows the periodicity of $V(\mathbf{r})$:

$$\psi_{n,\mathbf{k}}(\mathbf{r}) = u_n(\mathbf{r})e^{i\mathbf{k}\cdot\mathbf{r}}, \quad (3.2)$$

where $\psi_{n,\mathbf{k}}(\mathbf{r})$ is the eigenfunction of $\Psi(\mathbf{r})$, $u(\mathbf{r})$ is the periodic function that follows the periodicity of $V(\mathbf{r})$, and \mathbf{k} is the wave vector. The standing wave component in Eq. 3.2 ($e^{i\mathbf{k}\cdot\mathbf{r}}$) yields the infinitely extended probability distribution ($|\Psi(\mathbf{r})|^2$) over the entire crystal. In a real solid, this spatially infinite wavefunction is reduced to finite size by phonon or impurity scattering. These scattering processes cause a crystal to have nonzero electrical resistivity.

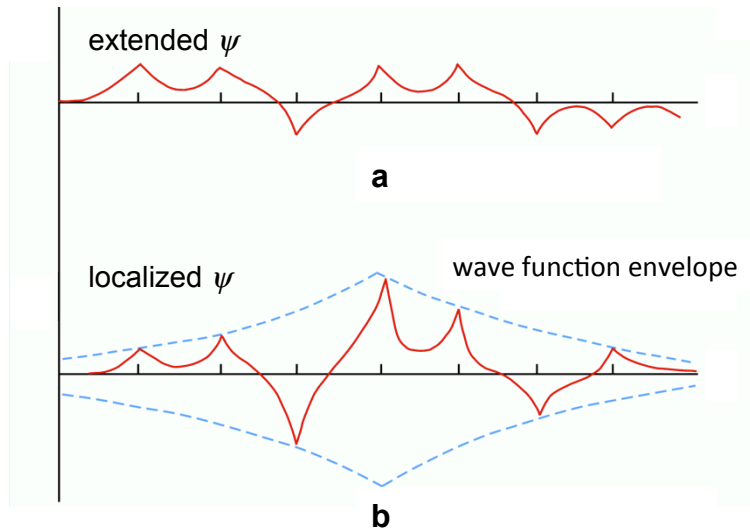


Figure 3.1 | Anderson localization. (a) Extended wave function in crystalline materials with negligible dynamic disorder. **(b)** Wave function localized either by static disorder or dynamic disorder. The size of the wave function envelope defines the localization length. Adapted with permission from ref. [58] (Copyright © 1971 Oxford University Press).

Boltzmann transport theory mathematically describes the scattering processes, which determine the mean free path (or relaxation time); the magnitude of carrier mobility is mainly governed by scattering mechanisms in the band transport model. However, if the randomness in a solid is sufficiently large, the electronic wavefunction loses its coherence, and hence carrier transport is not limited by scattering mechanisms (i.e., Anderson localization).

In 1958, Anderson presented the theory of electronic wavefunction localization in a disordered material [27]. Before his work, the poor electrical conductivity measured in disordered materials had traditionally been interpreted by a very small mean free path due to intense scattering, while the fundamental nature of the extended wavefunction still held. Anderson argued that scattering plays no role on carrier transport when the degree of disorder in a solid is greater than a critical point. The randomness of $V(\mathbf{r})$ at this critical disorder was shown to make the probability distribution ($|\Psi(\mathbf{r})|^2$) remain only within a small volume, beyond which it becomes infinitesimal. This phenomenon of a spatially localized wavefunction in a disordered material is now known as Anderson localization (Fig. 3.1).

3.1.2 Static and dynamic disorder

Any mechanism that can destroy the periodicity of $V(\mathbf{r})$ to the level of critical randomness over a certain time interval can cause Anderson localization. For example, a large concentration of crystal imperfections (e.g., impurities, grain boundaries, dangling bonds) destroys the periodicity of a crystal without a time dependence, and fluctuations of atomic position due to finite temperature destroy the periodicity of a crystal over a certain timescale. The former is known as static disorder, while the latter is known as dynamic disorder. Static disorder is believed to be the primary source of Anderson localization in metals and ISCs.

In an inorganic crystal, dynamic disorder does not significantly alter the periodic arrangement of atoms, since the covalent bonding energy (~ 1 eV) is far greater than the thermal energy at typical temperatures. For this reason, the intrinsically extended wavefunction is preserved, and the band transport model is a proper description for charge transport. In contrast to ISCs, dynamic disorder is considerable in a typical OSC and can easily destroy long-range order, since OSCs normally contain a significant amount of weak van der Waals (VDW) bonds, which have a bonding energy of a few tens of meV. The thermal energy at room temperature (25 meV) is comparable to the VDW bonding energy, and therefore significant dynamic disorder can exist in an OSC regardless of its static crystallinity, which causes Anderson localization. For example, the carrier wavefunction in an organic single crystal (i.e., negligible static disorder) was shown to localize due to dynamic disorder [28, 29, 59].

3.1.3 Transport of localized charge carriers

For a localized carrier, the role of external energy (usually from a phonon) is essential to activate the electric current. The Miller-Abrahams transition rate (v_{ij}), which has been the basis of many hopping models, describes this energy exchange process between the external energy source and charge carrier. The Miller-Abrahams rate depends first on the tunneling probability:

$$v_{ij} \sim \exp\left(-2\frac{R_{ij}}{\alpha}\right), \quad (3.3a)$$

and second on the energy exchange rate between the localized carrier and thermal energy source (phonon):

$$v_{ij} \sim v_0 \exp\left(-\frac{E_j - E_i}{kT} \theta(E_j - E_i)\right). \quad (3.3b)$$

The total probability of the transition is the product of Eqs. 3.3a and 3.3b [34]:

$$v_{ij} = v_0 \exp\left(-2\frac{R_{ij}}{\alpha} - \frac{E_j - E_i}{kT} \theta(E_j - E_i)\right), \quad (3.3c)$$

where α is the carrier localization length (which determines the wavefunction overlap), v_0 is the intrinsic attempt-to-jump rate, R_{ij} is the inter-site distance, E_i is the energy at site i , and $\theta(E_i - E_i)$ is the Heaviside unit step function. Equation 3.3a represents the tunneling nature of hopping transport that exponentially decreases with the ratio of R_{ij} and α . In Eq. 3.3b, v_0 describes the energy transfer rate between an electron and phonon (which depends on the mean phonon frequency). The latter term in Eq. 3.3b represents the probability of phonon occupation quantified by the Boltzmann statistics (i.e., low phonon concentration limit), while the Heaviside unit step function removes the need of phonon energy when a charge carrier jump to a lower energy state. As can be seen in Eq. 3.3, the Miller-Abrahams rate assumes constant α and v_0 that are independent of energy and direction, and hence α and v_0 are scalars that represent the averages of the localization length tensor and attempt-to-jump rate tensor, respectively, over energy and space domains. While this assumption of constant α and v_0 cannot describe the directional dependence of carrier transport on a molecular scale, it simplifies the transport formula; otherwise, considerable computational efforts are required (and physical information to support these efforts is unknown for many materials). Since the nanoscale directional dependences of α and v_0 often do not significantly affect averaged transport quantities on a bulk scale, the assumption of constant α and v_0 is acceptable for a sample with macroscale

homogeneity; the Miller-Abrahams rate has been shown to agree well with experimental data for OSCs [60, 61]. If molecules are aligned over a macro scale [9, 10], the magnitude of the scalar α may have a directional dependence which may need to be considered.

Despite of the simplicity of the Miller-Abrahams rate, the direct solution of Eq. 3.3 still requires appreciable computation power, since R_i , R_j , E_i , and E_j are all independent variables. Many averaging methods based on various integration techniques and percolation theory have been applied to solve Eq. 3.3 [32, 62-66]. Pasveer et al. provided a full computational calculation without averaging, known as the master equation approach [33]. These previous models commonly assume strong localization (i.e., α much less than the monomer or small molecule size), leading to a positive temperature dependence of the carrier mobility.

3.1.4 Uncertainties in previous hopping models

In the hopping model, three material parameters describe the carrier transport: the degree of carrier localization (α), the energy exchange rate between phonons and charge carriers (ν_0), and the degree of energetic disorder in the electronic density of states (DOS), as specified by the standard deviation of a Gaussian distribution (a_{DOS}). Since all three parameters directly affect the carrier mobility, these parameters are difficult to independently determine from measured electrical conductivity or mobility. This uncertainty has led to quantitative disagreement in ν_0 , which varies many orders of magnitude depending on assumed values for the other parameters [32, 33, 60, 66, 67] and broad qualitative disagreement regarding the nature of charge transport in OSCs. For example, α has been assumed to be much smaller than the molecular size, yet this assumption is not consistent with measurements of several high mobility OSCs that indicated that the wavefunction is larger than the molecular size [31, 68]. Furthermore, the negative

temperature dependence of mobility measured in these OSCs [31] cannot be explained under the assumption of small α (as assumed in previous hopping models), which predicts a positive temperature dependence of mobility.

3.2 Thermoelectric model

Likewise other organic electronic devices, understanding the carrier transport mechanism is critical to improving the thermoelectric performance in OSCs. While many thermoelectric models have been developed for ISCs based on the band transport theory, these models are not proper to describe the thermoelectric transport in OSCs, since charge carriers in OSCs are likely localized near room temperature. Few thermoelectric models have been developed for OSCs in the regime of the hopping transport [69], yet their lack of quantitative description for the carrier localization limits their scope for recently developed high mobility OSCs.

Since the magnitude of the localization length strongly affects the hopping transition rate (Eq. 3.3), the evaluation of this magnitude is a fundamental step for the proper description of hopping transport, and further needed for better understanding of recent high performance organic thermoelectric materials (e.g., PEDOT:Tos [13]). In this chapter, I developed a model for the Seebeck coefficient and the electrical conductivity in the regime of the hopping transport that provides their explicit dependences on the carrier localization length and the shape of the Gaussian DOS. Using this model, I quantitatively determine the degree of the carrier localization in several high mobility OSCs, which explains their weak dependence of carrier mobility on temperature.

3.2.1 Model for the Seebeck coefficient

Like electrical conductivity, the Seebeck coefficient (S) is a macroscopic transport quantity that is relatively straightforward to measure. Because the magnitude of electric voltage is related to the average energy of conducting charge carriers, S is strongly affected by the shape of the carrier DOS (e.g., a_{DOS}) and the wavefunction overlap between localized states at a particular energy (e.g., α). It is not, however, sensitive to v_0 , since v_0 is independent of carrier energy under the normal assumptions of thermally activated hopping [70, 71]. Therefore, a model for S that provides its explicit dependences on α and a_{DOS} offers a means to quantitatively study the degree of the carrier localization in OSCs. Combining this with a model for σ , which depends not only on α and a_{DOS} but also on v_0 , allows all three hopping parameters to be independently determined from S and σ data.

The Seebeck coefficient represents asymmetry in the energy distribution of conducting charge carriers with respect to the Fermi energy (E_F):

$$S = -\frac{k}{q} \int_{-\infty}^{\infty} \frac{(E - E_F)}{kT} \frac{\sigma(E)}{\sigma} dE, \quad (3.4)$$

where k and q are the Boltzmann constant and unit charge, respectively, and $\sigma(E)$ is the energy dependent electrical conductivity. Equation 3.4 can be rewritten by defining the transport energy, which is the average energy of conducting charge carriers:

$$S = -\frac{1}{qT} (E_{tr} - E_F), \text{ where } E_{tr} = \frac{1}{\sigma} \int_{-\infty}^{\infty} E \sigma(E) dE. \quad (3.5)$$

The definition used for E_{tr} in Eq. 3.5 is rather straightforward compared to other definitions (such as the fastest hopping energy [67]), and allows straightforward derivation of the

relationship between the hopping parameters and S . The energy dependent electrical conductivity ($\sigma(E)$), which is the key transport parameter governing S , μ , and σ , can be calculated in the weak field limit by the Miller-Abrahams transition rate (Eq. 3.3). Since the Miller-Abrahams rate depends on both spatial and energy variables, it is convenient to average this rate in the spatial domain first. The energy dependent hopping rate is then given by:

$$v_{\downarrow}(E) = v_0 \exp\left(-2\frac{R(E)}{\alpha}\right), \quad (3.6a)$$

$$v_{\uparrow}(E) = \int_E^{\infty} \exp\left(-\frac{\varepsilon - E}{kT}\right) v_{\downarrow}(\varepsilon) h(\varepsilon) d\varepsilon, \quad h(\varepsilon) = \frac{g(\varepsilon)(1 - f(\varepsilon))}{\int_E^{\infty} g(\varepsilon)(1 - f(\varepsilon)) d\varepsilon}, \quad (3.6b)$$

where $g(\varepsilon)$ is the carrier density of states (DOS) and $f(\varepsilon)$ is the Fermi-Dirac distribution. Two different hopping rates, $v_{\downarrow}(E)$ and $v_{\uparrow}(E)$, represent the downward hopping rate (for which the energy of the initial site is higher than the final site) and the upward hopping rate (for which the energy of the initial site is lower than the final site), respectively. The energy-dependent hopping distance, $R(E)$, is the hopping distance in the original Miller-Abrahams rate (R_{ij}) averaged in the spatial domain. Since the spatial dependence of the Miller-Abrahams rate appears only in R_{ij} , this averaging process causes the original rate to depend only on energy. $R(E)$ is calculated by the percolation criterion that the number of vacant states exceeds the percolation threshold (B) within the sphere of radius $R(E)$:

$$\left[\frac{4\pi}{3}R(E)^3\right]\left[\int_{-\infty}^E g(\varepsilon)(1 - f(\varepsilon)) d\varepsilon\right] \geq B, \text{ or}$$

$$R(E) = \left(\frac{4\pi}{3B} \int_{-\infty}^E g(\varepsilon)(1 - f(\varepsilon)) d\varepsilon\right)^{-1/3}. \quad (3.7)$$

The percolation threshold (B) ranges from 0.24 to 3.0 depending on the model used [72]; $B = 2.7$ is appropriate for the spherical (i.e., isotropic hopping conduction) case, and is used in the following calculations. Compared to other hopping models [32, 33, 60, 62-67, 70, 71], the formulation of Eqs. 3.6 and 3.7 enables straightforward derivation of the energy-dependent electrical conductivity $\sigma(E)$, which is crucial to calculate S .

Whereas the DOS in ISCs with static disorder is commonly modeled by a parabolic band of extended states with a small percentage of localized states in an exponential tail [58], the DOS in OSCs consists mostly of localized states due to dynamic disorder [28, 29], and is typically described by a Gaussian distribution [71, 73, 74]:

$$g(\varepsilon) = \frac{N_t(n_d)}{\sqrt{2\pi a_{DOS}^2}} \exp\left(-\frac{\varepsilon^2}{2a_{DOS}^2}\right), \quad (3.8)$$

where a_{DOS} represents the energetic disorder of localized states, which depends on material morphology [75]. $N_t(n_d)$ is the total DOS within the Gaussian envelope, which depends on the concentration of dopants (n_d), since dopants easily break the weak van der Waals bonding and increases the intermolecular distance of host molecules. The effect of this increase in intermolecular distance on carrier mobility is significant, since the hopping probability exponentially decreases with intermolecular distance (Eq. 3.3a). To quantify this effect of finite dopant volume on the carrier transport, a total DOS (N_t) is introduced that depends on the dopant concentration and the ratio of the dopant molecule volume to the host molecule volume (r):

$$N_t(n_d) = \frac{N_0}{1 + rn_d / N_0} = \eta(r, n_d) N_0, \quad (3.9)$$

where N_0 is the total DOS at $n_d = 0$, typically equal to the molecular density; for a small molecular OSC, one molecule occupies one state, while for a polymer, one monomer occupies one state. It should be noted that the decrease in N_t due to nonzero dopant volume is assumed to be isotropic, and Eq. 3.9 is valid for a macroscopic scale as is the Miller-Abrahams rate. Using Eq. 3.6 and the generalized Einstein relation ($\mu = Rv^2 \frac{q}{n} \frac{\partial n}{\partial E_F}$, which is valid up to high carrier concentrations [76]), the carrier mobility is given by:

$$\mu(E) = \frac{q}{kT} (1 - f(E)) \left[R(E)^2 v_{\downarrow}(E) + \int_E^{\infty} R(\varepsilon)^2 \exp\left(-\frac{\varepsilon - E}{kT}\right) v_{\downarrow}(\varepsilon) h(\varepsilon) d\varepsilon \right]. \quad (3.10)$$

The electrical conductivity can be calculated by integrating $qn(E)\mu(E)$ over an infinite energy interval, from which the carrier concentration dependent mobility can be derived:

$$\mu(n) = \eta^{1/3} \exp\left(2 \frac{l(1 - \eta^{-1/3})}{\alpha}\right) \left[\frac{\int_{-\infty}^{\infty} \sigma(E) dE}{qn} \right]_{r=0}, \quad (3.11)$$

where l is the molecular spacing, typically assumed to be $N_t^{-1/3}$ (i.e., cubic lattice) [33]. The term outside the bracket in Eq. 3.11 is the analytic expression for the effect of dopant volume on the carrier mobility. The carrier concentration is calculated using the Fermi-Dirac distribution:

$$n = bn_d = \int_{-\infty}^{\infty} g(\varepsilon) f(\varepsilon) d\varepsilon, \quad (3.12)$$

where b is the effective dopant ionization fraction that quantifies the number of conducting charge carriers per dopant. In OSCs, b is typically much smaller than unity due to the weak van der Waals characteristics [77], leading to a significant increase in the hopping distance due to the presence of many non-ionized dopants at high carrier concentrations.

Figure 3.2 compares the carrier mobility numerically calculated by the averaged hopping rate (Eqs. 3.6 and 3.7) with the mobility calculated by the master equation approach [33] that does not use averaging approximations. Since the master equation approach assumes nearest neighbor hopping, $R(E_{tr})$ is set equal to l and incorporated into the numerical calculations for this figure, a method previously employed to compare other models with the master equation approach [67]. The model presented here agrees well with the master equation approach up to $n/N_0 = 10^{-1}$, beyond which the decrease in the number of final states at high concentrations is known to reduce the carrier mobility [32]. This good agreement between the model and the master equation approach validates the approximations used in Eqs. 3.6 and 3.7.

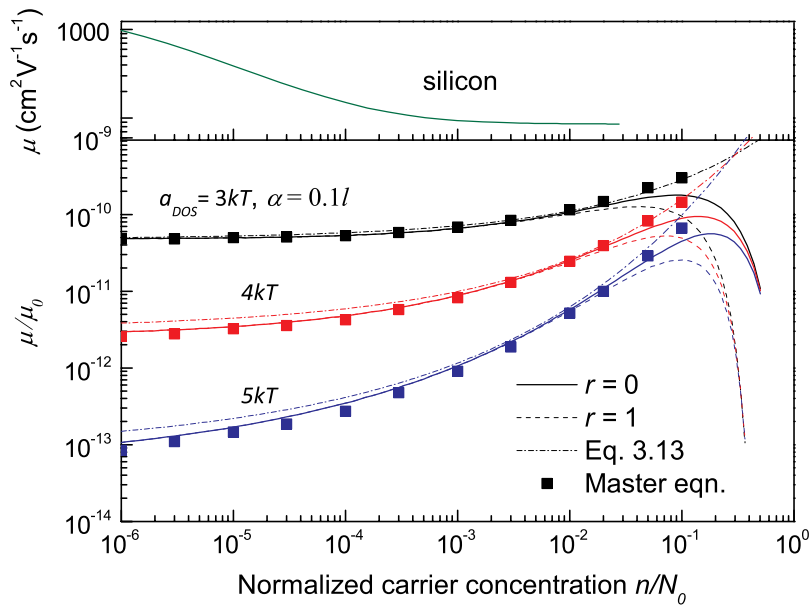


Figure 3.2 | Dependence of the carrier mobility on the normalized carrier concentration. Lower: carrier mobility as a function of the normalized carrier concentration (n/N_0) for various Gaussian DOS widths. To compare with the master equation approach [33], α is assumed to be equal to l as is assumed in Ref. [33], and b is assumed to be unity. Upper: the carrier mobility in doped silicon as a function of n/N_0 [24]. N_0 for silicon is assumed to be equal to its atomic density ($5 \times 10^{22} \text{ cm}^{-3}$).

At low carrier concentrations, semi-analytical expressions can be found for σ and S . For strongly localized carriers at relatively low concentrations ($(l/\alpha)^3 \gg 1$ and $n/N_0 < 10^{-2}$), the carrier mobility and electrical conductivity are given by:

$$\sigma = qn\mu = qn\mu_0 \exp\left(-p_0 - C_1 \hat{a}_{DOS} - \left(C_2 - \frac{C_3}{p_0}\right) \hat{a}_{DOS}^2\right) \exp\left(\frac{1}{2}(\hat{a}_{DOS}^2 - \hat{a}_{DOS}) \left(\frac{2n}{N_t}\right)^\delta\right), \quad (3.13)$$

where $\mu_0 = ql^2\nu_0/a_{DOS}$, $p_0 = C_4(B/N_t\alpha^3)^{1/3}$, $\delta = (2/\hat{a}_{DOS}^2)(\ln(\hat{a}_{DOS}^2 - \hat{a}_{DOS}) - \ln(\ln 4))$, and $\hat{a}_{DOS} = a_{DOS}/kT$. Constants C_1 , C_2 , C_3 , and C_4 have best-fit values of 0.26, 0.51, 1, and 1.44, respectively; the associated numerical values for this four-constant parameterization agree well with a range of transport models [32]. The Seebeck coefficient (valid for $n/N_t \ll 10^{-6}$) is given by:

$$S = \frac{1}{qT} \left([E_F] - [E_r] \right) = \frac{1}{qT} \left\{ \left[kT \ln \frac{n}{N_t} - \frac{1}{2} \frac{a_{DOS}^2}{kT} \right] - \left[\frac{a_{DOS}}{4} \left(\ln \left(\sqrt{\frac{2}{\pi}} \frac{2B}{9\pi^2} \right) - \frac{7}{5} \sqrt{\hat{a}_{DOS}} \ln \hat{a}_{DOS} + \ln \frac{1}{N_t \alpha^3} \right) \right] \right\}. \quad (3.14)$$

3.2.2 Dependence of the Seebeck coefficient on the hopping parameters

As can be seen in the analytical form of the Seebeck coefficient (Eq. 3.14), S is sensitive to α and a_{DOS} , while it is not dependent on ν_0 , allowing the independent extraction of α and a_{DOS} . Figure 3.3 plots the Seebeck coefficient, numerically calculated based on Eqs. 3.4 and 3.10, as a function of carrier concentration for several different α and a_{DOS} . As shown in Fig. 3.3, it is clear that the slope of S ($dS/d(\ln n)$) is mainly governed by a_{DOS} and is almost unchanged as α is varied.

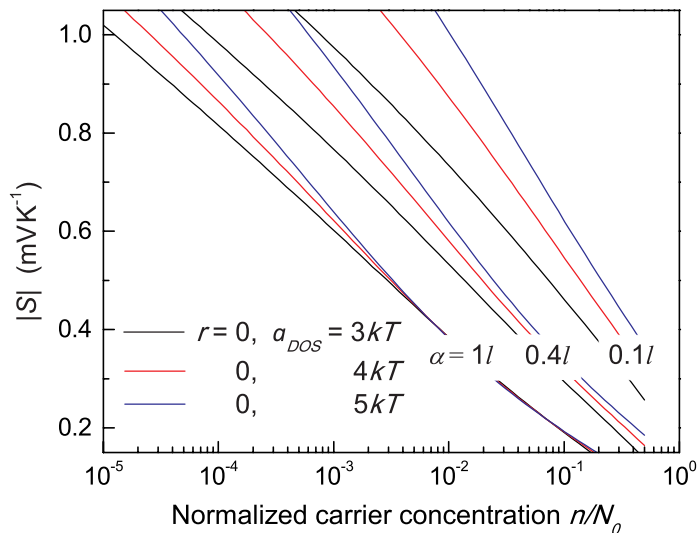


Figure 3.3 | Seebeck coefficient versus n/N_0 for different a_{DOS} and α . dS/dn is primarily governed by a_{DOS} .

Therefore, one can first determine the DOS width (a_{DOS}) by a slope fit and subsequently determine α by a magnitude fit. With these two independently determined parameters, v_0 can be independently determined by a fit to measured carrier mobility or electrical conductivity data.

3.3 Weak carrier localization in high mobility OSCs

The model for the Seebeck coefficient presented here provides a mean to independently determine the three hopping parameters (α , a_{DOS} , and v_0), and hence allows one to assess the degree of carrier localization in OSCs. To demonstrate this method, the three hopping parameters are quantitatively derived as described below in the high mobility small molecular OSC pentacene and the high mobility polymer OSC poly(3,4-ethylenedioxythiophene) (PEDOT). The carrier localization lengths in these OSCs were predicted by the model to be comparable to the molecular spacing (i.e., the distance between pentacene molecules or the distance between PEDOT monomers), which is much larger than previously assumed. With this weak localization,

the model accurately predicts a very weak (band-like) temperature dependence of mobility. The effects of dopant type and chemical additive on carrier localization are also discussed.

3.3.1 Pentacene bulk films and field-effect transistors

Pentacene is one of the high mobility OSCs that shows a very weak or negative temperature dependence of mobility. Since this band-like temperature dependence cannot be explained by previous hopping models, many researchers have explained this phenomenon with a band transport model based on empirical evidence [30]. However, evidence of carrier localization was reported in crystalline pentacene films [28, 29, 59] and in high mobility pentacene field-effect transistors (FETs), even those in which a negative temperature dependence of mobility was experimentally observed. It was found that the effect of dynamic (thermal) disorder on electronic structure is profound, leading to carrier localization regardless of crystallinity.

To provide further insight on the controversial nature of carrier transport in pentacene, the model for the Seebeck coefficient described above was fit to the data for a pentacene FET [78] and a 2,3,5,6-tetrafluoro-7,7,8,8-tetracyanoquinodimethane (F4-TCNQ) doped bulk pentacene film [79] at room temperature (Fig. 3.4). By a slope fit, a_{DOS} was found to be 0.12 eV for both the FET and the bulk film, while the magnitude fit yielded $\alpha = 1.5l$. While a cubic lattice was assumed to calculate the molecular spacing ($l = N_l^{-1/3}$), this assumption does not reduce the validity of the derived $\alpha = 1.5l$ for pentacene, since the quantity that determines S is not the absolute value of α or l itself, but their ratio (α/l); even if a shorter l is used in the π - π stacking direction, the relative value $\alpha = 1.5l$ still holds. Using these two values, $v_0 = 2.2 \times 10^{13} \text{ s}^{-1}$ for the FET and $v_0 = 2.5 \times 10^{11} \text{ s}^{-1}$ for the doped bulk film are derived from fits to σ (or μ). For the bulk film, r is found to be 8 by a fit to σ at high carrier concentrations; this is a reasonable volume

expansion for an impurity in pentacene [80] since the volume expansion caused by a dopant includes not only the dopant volume itself but also the volumes of the voids that the dopant creates by distorting the well-packed pentacene herringbone structure. For the pentacene FET, $r = 0$, since no dopant is present in it.

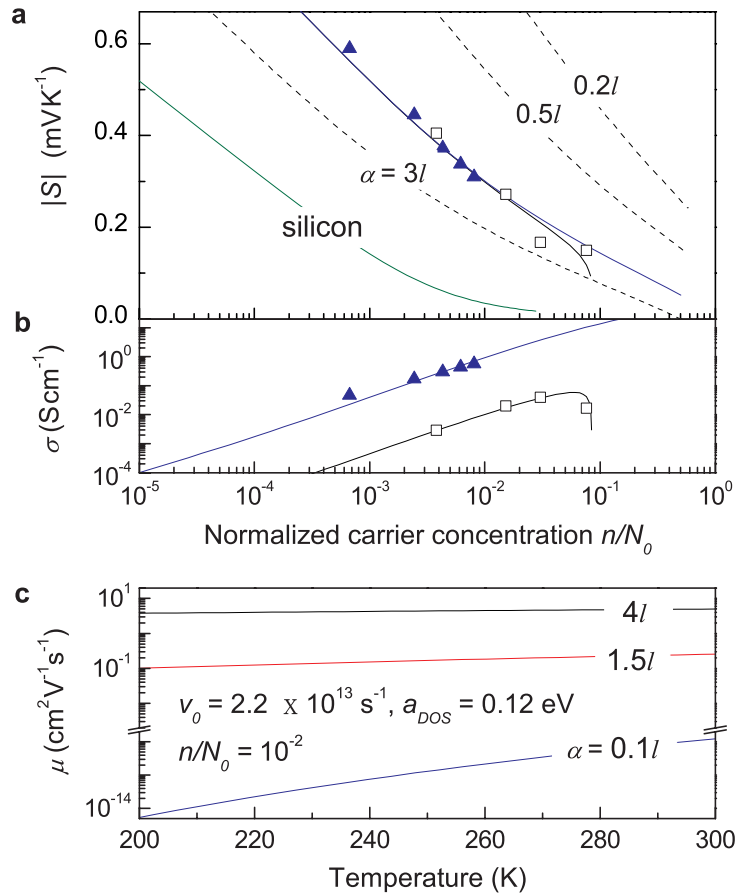


Figure 3.4 | Seebeck coefficient, electrical conductivity, and mobility in pentacene FETs and bulk films. (a-b) S and σ measured at room temperature in pentacene FETs [78] (closed symbols) and doped bulk pentacene films [79] (open symbols); also shown is silicon data [23]. $N_0 = 2.9 \times 10^{21} \text{ cm}^{-3}$ is used for pentacene [81]. The effective FET channel thickness (3 nm) [82] is used to convert measured FET channel densities to carrier concentrations. $b = 0.76$ as reported for F₄-TCNQ in pentacene [79] is used to convert measured dopant mole fractions to carrier concentrations. σ for the FET is calculated from the measured field effect mobility, since it is typically similar to the Hall mobility for small molecular FETs [78, 83]. **(c)** Temperature dependence of mobility for several values of α at $n/N_0 = 10^{-2}$, a typical concentration for operating FETs.

The derived value of α suggests that the previous assumption of strong localization ($\alpha = 0.1l$) may not be applicable to high mobility pentacene. Also, α in pentacene exceeds the molecular size, which is consistent with prior measurements of the large carrier wavefunction size in pentacene FETs [68]. With this large α derived from S , the model further predicts the very weak temperature dependence of mobility (Fig. 3.4c), which is consistent with previous studies of pentacene FETs in which the mobility showed a band-like temperature dependence even when carriers were known to be localized [31]. It should be noted that the contribution of phonons as a scattering source, while not incorporated in the model presented here, should be considered if the carrier localization length is larger than the phonon wavelength. As dynamic disorder decreases at low temperatures and α becomes large, phonon scattering becomes more significant, explaining why the negative temperature dependence of carrier mobility in pentacene FETs was mainly observed only at low temperatures [31, 78].

Furthermore, the derived hopping parameters for the pentacene FET and the bulk pentacene film suggest that the carrier localization length is not significantly affected by the presence of dopants but is instead primarily governed by the conducting molecules between which hopping takes place. The fact that the FET and the doped bulk film are predicted to have the same α regardless of the presence of ionized dopants is consistent with prior work on polyaniline in which α was found to remain nearly constant regardless of the type of dopant used [84]. In contrast, v_0 is strongly affected by dopants, differing by more than an order of magnitude for the two pentacene samples. It is reasonable that v_0 in the doped bulk pentacene film is smaller than in the FET since ionized dopants in pentacene distort the highly packed herringbone structure, soften the material, and hence red-shift the dominant phonon frequency [85] at which electron-phonon coupling

occurs. This change in ν_0 is predicted to be responsible for the difference in carrier mobility in the FET ($0.15 \text{ cm}^2 \text{ V}^{-1} \text{ s}^{-1}$) [78] and the doped bulk film (0.0016 to $0.0028 \text{ cm}^2 \text{ V}^{-1} \text{ s}^{-1}$) [79].

Anisotropic transport along various molecular directions is often present in a real material, and the hopping parameters derived in this work may not fit for each direction in the microscopic crystal. However, the derived values still represent the averaged bulk transport that includes the effects of grain boundaries and different molecular orientations in the path along which S and σ were measured. Carrier transport in an FET is not quite 3D conduction, since the effective channel thickness in an FET is typically very small (a few molecular layers). To compare 3D and 2D conduction models, the percolation threshold B was set to 4.5, which represents a circular rather than spherical network (i.e., 2D conduction), resulting in $\alpha = 1.8l$. Since the carrier transport in the FET is neither completely 3D nor completely 2D, the real α in the FET channel is predicted to be between $1.5l$ and $1.8l$. The temperature dependence of mobility predicted by the model does not change significantly as α is increased from $1.5l$ to $1.8l$, and the predicted ν_0 does not change at all. For these reasons, the interpreted effect of dopants on the hopping parameters are not invalidated by assuming a 2D percolation threshold.

3.3.2 PEDOT bulk film doped by various chemicals

Poly(3,4-ethylenedioxythiophene) is one of the most promising OSCs [13, 86], as it is a solution processable OSC that has an electrical conductivity comparable to indium tin oxide (ITO). The effects of dopant type [13] and chemical additive [87] on carrier transport in PEDOT have been found experimentally to be profound, yet their underlying effects on carrier localization and electronic structure have not yet been elucidated.

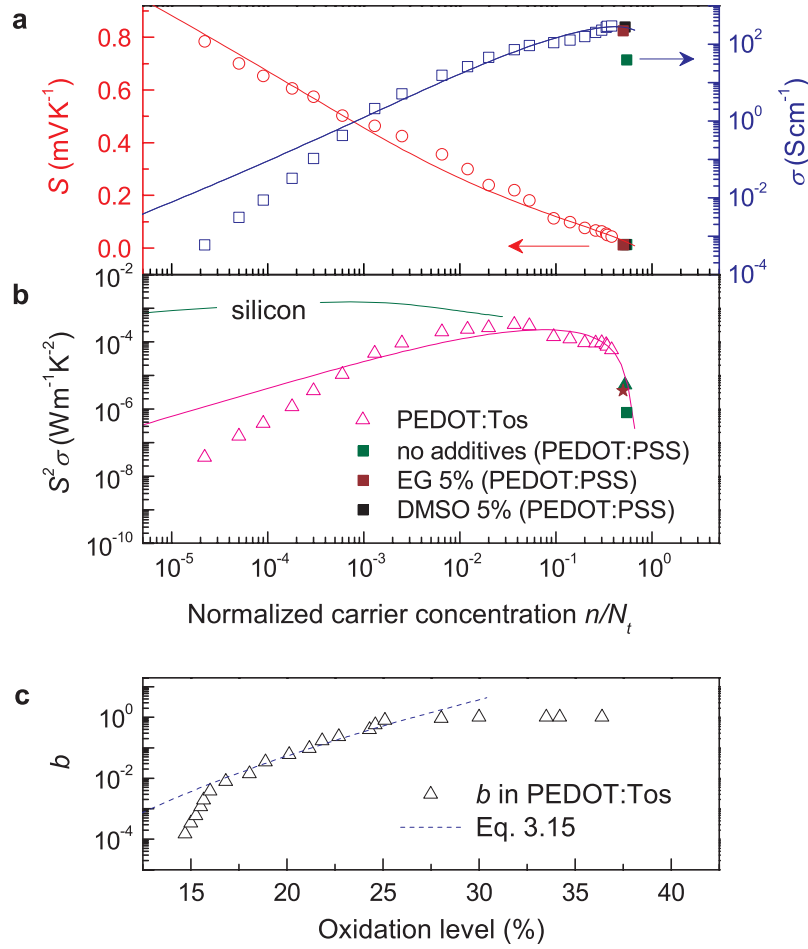


Figure 3.5 | Hopping parameters in PEDOT. (a) S and σ vs n/N_t for PEDOT:Tos [13] (open symbols) and PEDOT:PSS [17] (closed symbols). $N_t = 10^{21} \text{ cm}^{-3}$ and $r \approx 1$ (based on molecular weights of Tos and EDOT) are used for numerical calculations [88]. **(b)** Room temperature $S^2\sigma$ measured in PEDOT:Tos [13] (open symbols) and PEDOT:PSS [17] (closed symbols), and calculated for $a_{DOS} = 3.5kT$, $\alpha = 2.1l$ and $r = 1$. Also shown is $S^2\sigma$ calculated for silicon (lines) [23, 24]. **(c)** Effective ionization fraction calculated for PEDOT:Tos (symbols) and a fit to Eq. 3.15 (dashed line).

Literature studies of S in PEDOT and other polymer OSCs often do not measure a free carrier concentration directly but instead measure an oxidation level, which defines the fraction of ionized dopants ($ox = n_d/N_{t,dopant}$). However, not every dopant induces a free charge carrier [89], leading to an effective dopant ionization fraction (b) less than unity [77]:

$$\frac{n}{n_d} = b = \exp(-E_a / kT) = \exp\left[-\left(E_{a,max} - \beta n_d^{1/3}\right) / kT\right], \quad (3.15)$$

where $E_{a,max}$ is the maximum activation energy of the dopant at a dilute concentration and β captures the dependence of E_a on dopant concentration. Since the oxidation level itself does not directly relate to S , it must be converted to free carrier concentration in order to interpret the $ZT = 0.25$ measured in PEDOT:Tos [13], the highest value reported among stable OSCs as of 2011. Given the fact that $dS/d(\ln ox)$ is constant in PEDOT:Tos at high oxidation levels ($> 25\%$) [13], which implies constant b , α and a_{DOS} can first be determined from the data measured at these high oxidation levels, where the constant b is assumed to be unity (i.e., one ionized dopant contributes one free charge carrier). For low oxidation levels, $dS/d(\ln ox)$ is much larger in magnitude than the characteristic value of $-k/q$, implying that b increases with oxidation level, likely due to charge screening. Using the α and a_{DOS} derived for high oxidation levels, the change in b at low oxidation levels is derived as a function of oxidation level. Simultaneous fitting of the measured S and σ data to the model given above yields $E_{a,max} = 0.83$ eV, which is on the order of the exciton binding energy in OSCs [90], and $\beta = 1.3 \times 10^{-7}$ eV·cm, which is similar to its value in other OSCs [77]. Below 16% oxidation level, b changes more rapidly, and Eq. 3.15 cannot explain this high rate as it leads to a non-physical value for $E_{a,max}$. This rapid change in b is presumably due to the strong binding energy of the accumulated tetrakis(dimethylamino)ethylene (TDAE) species used to dedope the PEDOT:Tos. The effect of TDAE residues is evident on σ but not on S , since the remaining TDAE has a strong electrostatic force and likely distorts the nano-crystalline PEDOT:Tos morphology, decreasing v_0 as F4-TCNQ does in pentacene.

A slope fit yields $a_{DOS} = 3.5 \pm 0.4 kT$, which is typical for PEDOT [66]. Fits to S vs. n and σ vs. n yield $\alpha = 2.1l$ and $v_0 = 1 \pm 0.2 \times 10^{14} \text{ sec}^{-1}$, respectively. While literature data for S in PEDOT doped by polystyrene sulfonate (PSS) is not available over a wide range of carrier

concentrations, the magnitude of S does not vary with a_{DOS} at high concentrations (Fig. 3.3) and hence α can be derived from the single data point without significant uncertainty. As shown in Fig. 3.5a, the magnitude of S measured in PEDOT:PSS without additives, PEDOT:PSS with 5 volume% ethylene glycol (EG), and PEDOT:PSS with 5 volume% dimethyl sulfoxide (DMSO) all fall on the same S curve [17], indicating that α remains the same regardless of dopant type and chemical additive used. However, as is clear from the plot of σ , the dopant type and chemical additive strongly affect the magnitude of ν_0 : the sample without additives has a predicted ν_0 of $1.4 \pm 0.2 \times 10^{13}$, while the sample with EG additive has $7.9 \pm 0.2 \times 10^{13}$ and the sample with DMSO additive has $1 \pm 0.2 \times 10^{14} \text{ sec}^{-1}$. DMSO and EG are known to produce rod-like conformations in PEDOT:PSS that increase the polymer's elastic modulus [91], suggesting a higher phonon mean frequency and hence a reason for larger ν_0 in PEDOT:PSS with DMSO or EG additives used.

Together with the analysis of pentacene data, these results suggest that the carrier localization is almost independent of dopants and chemical additives, whereas they strongly alter an OSC's vibronic characteristics, which is responsible for the different σ values measured in OSCs with various dopants and additives. The significant enhancement of the maximum $S^2\sigma$ in PEDOT:Tos [13] compared to previous work [17] is mainly due to a change in the electron-phonon coupling or the mean phonon frequency rather than carrier delocalization.

3.4 Three regimes of the charge carrier transport in OSCs

Like the charge carrier mobility, the nature of carrier transport in OSCs can be also characterized by the temperature dependence of the Seebeck coefficient. Three distinct temperature

dependences were found for the different magnitudes of α : the activated regime of $\alpha \ll l$, the intermediate hopping regime of $\alpha \sim l$, the variable range hopping (VRH) regime of $\alpha \gg l$.

Figure 3.6 shows the Seebeck data (normalized to the value at 300 K) for several OSCs. For Naphthalenetetracarboxylic dianhydride NTCDA [92], the carrier transport is found to be the activated regime as it $\alpha = 0.2l$ and $n/N_t = 5.2 \times 10^{-7}$. This highly localized, low carrier concentration regime is analogous to Case 1 in ISCs, since E_{tr} locates far away from E_F . Both the numerical (Fermi-Dirac) and analytical (Eqs. 3.13 and 3.14) solutions for σ (not shown) and S are accurate in this activated regime, and correctly predict the activated ($\sim 1/T$) temperature dependence. The activation energies derived by the model for the values of α and n/N_t given above are $\varepsilon_{a,\sigma} = 404$ meV and $\varepsilon_{a,S} = 326$ meV, which are very close to the measured values of $\varepsilon_{a,\sigma} = 400$ meV and $\varepsilon_{a,S} = 330$ meV [92]. For polyacetylene [93], the transport occurs in the VRH regime as its $\alpha = 4.7l$ and $n/N_t = 2.34 \times 10^{-1}$. This relatively delocalized, high carrier concentration regime is analogous to the VRH transport developed by Mott. While the analytical solutions (Eqs. 3.13 and 3.14) are not applicable for these large α and n/N_t , the numerical calculation accurately shows that S increases with T (which is consistent with VRH) and that the increase is approximately linear (which is similar to the finding for the exponential tail DOS [62]). For pentacene, $\alpha = 1.5l$, extracted by the S fitting shown in Fig. 3.4, is incorporated into the numerical calculation of S , since α is primarily determined by host molecule but not by dopants and morphology (section 3.3). With this separately derived α , my model predicts the very weak temperature dependence of the Seebeck coefficient, which is distinct from well-known two extreme cases. Using $n/N_t = 2.1 \times 10^{-2}$, which is a reasonable carrier concentration in an operating OFET, my model does fit the measured Seebeck coefficients in the pentacene FETs [94]. This distinct transport regime, in which $\alpha \sim l$ and $d\mu/dT, dS/dT \sim 0$, is named as the intermediate

hopping regime. The intermediate hopping regime is believed to uniquely appear in OSCs when the static disorder is sufficiently low but their van der Waals characteristic still causes the dynamic disorder. Consequently, the size of the localized wavefunction is on the order of molecular spacing (i.e., $\alpha \sim l$), since the wavelength of the dynamic disorder is on the order of l .

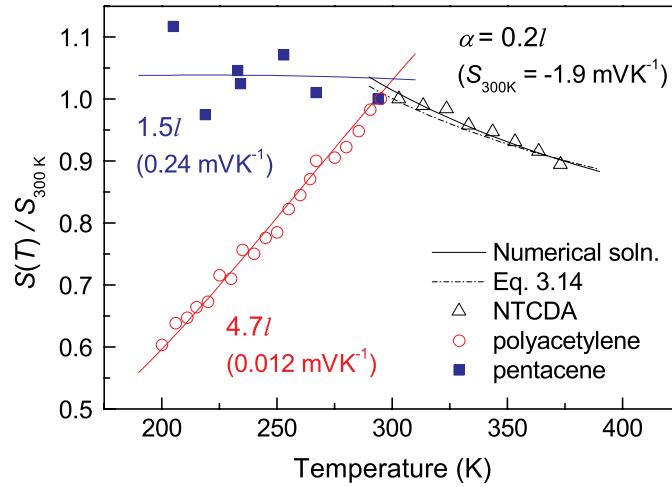


Figure 3.6 | Three regimes of hopping transport. As α increases, $d|S|/dT$ changes from an activated regime ($|S| \sim 1/T$) in NTCDA [92] to an intermediate regime ($|S| \sim \text{constant}$) in pentacene [94] to a VRH regime ($|S| \sim T$) in polyacetylene [93].

Chapter 4

Weak carrier localization in doped pentacene bulk films

Organic semiconductors (OSCs) can be classified as amorphous or crystalline depending on the degree of their crystallinity (static disorder). In crystalline OSCs, the localization of charge carriers is mainly caused by intermolecular thermal fluctuations (dynamic disorder). For this carrier localization due to dynamic disorder, the size of the localized wave function (α) is expected to be on the order of the molecular spacing (which is on the order of the phonon wavelength), and transport in this weakly localized carrier regime is classified as “intermediate hopping transport regime” (Chapter 3). Since α extends at or beyond a single molecule in the intermediate hopping regime, phonons can act not only as an external energy source for tunneling transport but also as scatterers at low temperatures [31]. Furthermore, impurity scattering also may occur at high doping concentrations for materials in which α is larger than the inter-dopant distance.

Carrier transport in pentacene can be classified by this intermediate hopping regime when its static disorder is sufficiently low. By varying the degree of static disorder in pentacene bulk films (e.g., grain size), I experimentally demonstrate the transition from an activated to an intermediate hopping regime [95]. A new approach based on spontaneous dedoping was used to measure bulk carrier mobility over a wide range of carrier concentrations in doped pentacene films.

4.1 Sample preparation and characterization

The typical approach to demonstrate the band-like transport is to measure $d\mu/dT$, which represents the effect of phonon scattering. Like phonon scattering, impurity scattering also indicates the intermediate hopping regime, since impurity scattering can occur when the magnitude of α is comparable to the distance between impurities. To study this impurity scattering in doped bulk pentacene films, the Seebeck coefficient (S) and electrical conductivity (σ) were simultaneously measured over a wide range of carrier concentrations. The static disorder in pentacene films was controlled by the deposition condition, and the spontaneous dedoping of iodine was adopted to enable a wide range of carrier concentrations to be measured in the same sample, all of which provide a means to measure the bulk carrier mobility.

4.1.1 Pentacene films with various degrees of static disorder

The temperature dependence of pentacene field-effect-transistors (FETs) has been shown to obey either activated or intermediate hopping transport [96] depending on static disorder [97]. These observations imply that the nature of carrier transport can shift from an activated regime to an intermediate hopping regime when the static disorder is sufficiently low. To experimentally demonstrate the effect the static disorder on carrier transport, pentacene was thermally evaporated at different deposition rates (0.04 to 0.4 \AA s^{-1}), which produced different grain sizes. Since pentacene molecules have more time to congregate at lower deposition rates, lower deposition rates lead to larger grain sizes, as shown in Fig. 4.1. For the particular rate of 0.4 \AA/s which yielded an average grain size of 0.2 μm , the morphology of the grain is distinct from other samples as it contains small sub-grain structures (~ 30 nm) within the 0.2 μm grain, which may considerably increase the static disorder and hence result in transport that is distinct from the

other samples (section 4.2). A shadow mask was used to define a pentacene sample area of 2×2 mm², on which two gold electrodes were thermally evaporated (50 nm thick, 1 mm width \times 2.5 mm long), separated by a channel of a certain length ($L = 25, 50,$ or 75 μm).

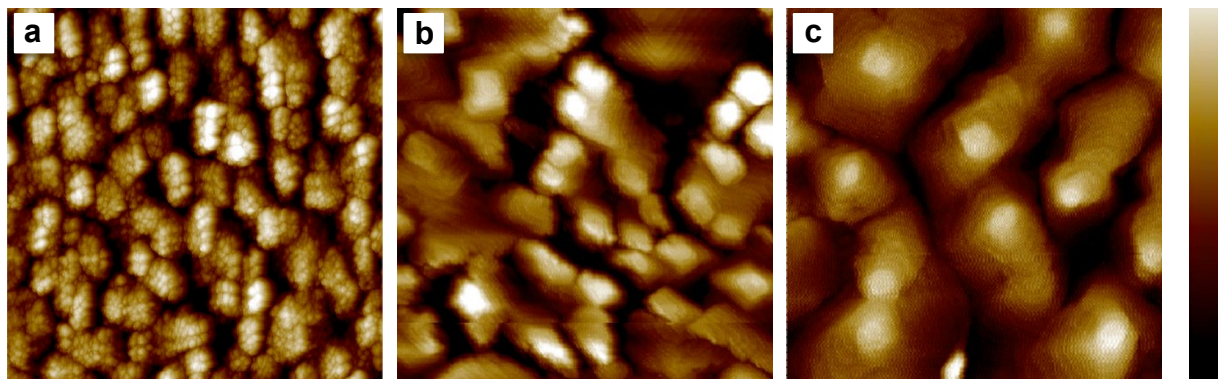


Figure 4.1 | AFM topography images in pentacene films. (a-c) AFM topography images ($2\mu\text{m} \times 2\mu\text{m}$, color scale: ± 20 nm) for pentacene films deposited at (a) 0.4 \AA^{-1} (average grain size: $0.2 \mu\text{m}$), (b) 0.1 \AA^{-1} (average grain size: $0.5 \mu\text{m}$), and (c) 0.04 \AA^{-1} (average grain size: $0.8 \mu\text{m}$).

4.1.2 Spontaneous dedoping technique

Spontaneous dedoping allows properties to be measured in a single sample at various doping levels and thus provides an efficient route to measure the bulk mobility over a wide range of carrier concentrations. To examine impurity scattering, the carrier mobility needs to be measured over a wide range of impurity (doping) concentrations. This large range of doping concentrations requires numerous samples at different doping levels, leading to considerable effort and time. Furthermore, uncertainty exists because of sample-to-sample variation, since pentacene is not stable in air. Iodine is a strong oxidant, and hence easily alters the hole concentration in pentacene. While iodine is not a stable dopant due to its high vapor pressure larger than 1 atm at room temperature, the continuous evaporation of iodine vapor from pentacene results in a doping

concentration that changes over time, and therefore provides a means to obtain a wide range of carrier concentrations in a single pentacene sample.

To facilitate iodine doping and dedoping, a thin pentacene film was stored in a glass jar filled with saturated iodine vapor for 60 minutes at room temperature. After the 60 minutes of iodine doping, the electrical properties of the doped pentacene sample were measured in air, during which time iodine vapor continuously evaporated from the pentacene film, leading to a continuously decreasing dopant (carrier) concentration. This spontaneous dedoping is a slow process, taking approximately 100 hours to reduce the iodine concentration by half [98]. It should be noted however that the rate of decreasing carrier concentration is much faster, since the effective ionization fraction of iodine decreases with as its concentration decreases (Eq. 3.15).

4.1.3 Simultaneous measurement of S and σ

While the iodine dedoping process is sufficiently slow to preform real-time measurements of S and σ at a certain doping concentration, an automated measurement run by computer software is required to track the continuously changing S and σ . A LABVIEW program that controls the simultaneous measurement of S and σ was written, and the electrical properties of doped pentacene films were recorded during iodine dedoping. Figure 4.2 shows a single measurement period, in which two measurement sequences are taken. During the first measurement sequence (“I” in Fig. 4.2), two Peltier units were turned on to make a 1-dimensional temperature gradient across the sample, and the thermal voltage across the gap (ΔV) started being recorded at 2 Hz, after which the I-V curve was measured by a semiconductor analyzer (HP 4156B) to determine σ . Temperature data was manually recorded after it stabilized using two microthermocouples (25

μm diameter) which were separated by a distance D_{TC} , and the temperature difference between these two thermocouples (ΔT_{TC}) was recorded. The temperature difference across the gap (ΔT) was calculated by $\Delta T = \Delta T_{TC} \times L / D_{TC}$. A larger temperature gradient (“II” in Fig. 4.2) was then applied, and the same measurements were performed as during the sequence “I”. Afterward, the Peltier units were turned off and the thermal voltage was monitored until it returned to zero. The measured S and σ in the sequences “I” and “II” were averaged to determine their magnitude at a certain doping concentration; the difference in data measured during these two sequences was observed to be small, indicating the reliability of the dynamic measurement. Sequences “I” and “II” (which composed one period of the measurement) typically took 300 seconds and were repeated until the sample resistance became too high to be tested ($50 \text{ M}\Omega$). This measurement time of 300 seconds was reduced for the sample at high doping concentrations by skipping the exponential tail part in Fig. 4.2, as the iodine dedoping rate is fast at these concentrations.

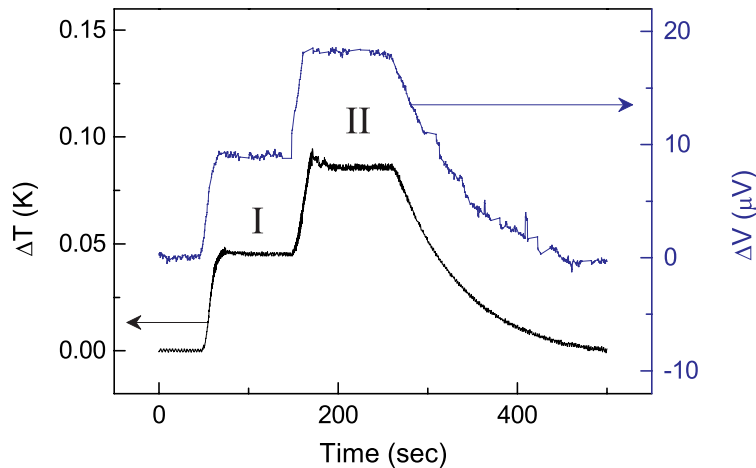


Figure 4.2 | Seebeck voltage measurement during iodine dedoping. Two different temperature gradients were applied during the one period of measurement, which consisted of sequences I and II.

4.2 Transition of the transport regime in bulk pentacene films

As can be seen in Eq. 3.14, the Seebeck coefficient relates to several material parameters, such as the carrier concentration, the degree of carrier localization, and the shape of electronic density of states (DOS). Within a single pentacene sample, change in the latter two parameters (α and a_{DOS}) are negligible as they are primarily determined by the host molecule (Chapter 3), and therefore changes in S are primarily governed by changes in carrier concentration. By simultaneously measuring S and σ , from which the carrier concentration was deduced, the carrier mobility μ was extracted over a wide range of doping concentrations. Two distinct dependences of the carrier mobility on the dopant concentration were observed, indicating the transition from an activated (small grain) regime to an intermediate hopping transport (large grain) regime.

4.2.1 Bulk mobility measurement

The Seebeck coefficient is proportional to the average energy of conducting charge carriers with respect to the Fermi level:

$$S = -\frac{1}{qT}(E_{tr} - E_F), \text{ where } E_{tr} = \frac{1}{\sigma} \int_{-\infty}^{\infty} E\sigma(E)dE, \quad (4.1)$$

where q is the unit charge and E_{tr} is the transport level, which represents the average energy of conducting charge carriers. It should be noted that Eq. 4.1 is valid regardless of the transport mechanism, as it is based on the definition of electric voltage. In non-degenerate ISCs, E_{tr} is very close to the band edge (or the mobility edge, E_V), and the Seebeck coefficient is proportional to

$E_F - E_V$ [58]. For lightly doped ISCs, Boltzmann statistics can be used to approximate the carrier (hole) concentration (n):

$$n = N_V \exp\left(-\frac{E_F - E_V}{kT}\right), \quad (4.2)$$

where k is the Boltzmann constant and N_V is the effective DOS at E_V . Note that E_V is a fixed energy state whereas E_{tr} changes with carrier concentration. An equation similar to Eq. 4.2 can be used to approximate the carrier concentration in OSCs by replacing E_V with E_{tr} :

$$n = N_0 \exp\left(-\frac{E_F - E_{tr}}{kT}\right), \quad (4.3)$$

where N_0 is the total DOS within the Gaussian envelope, which is typically equal to the pentacene molecular density (i.e., one pentacene molecule occupies one electronic state) [81]. The validity of Eq. 4.3 can be tested by comparing the carrier concentration calculated using Fermi-Dirac statistics (which is exact) with Eq. 4.3. Figure 4.3 shows the comparison between an approach using Fermi-Dirac statistics and one using Eq. 4.3; Eq. 4.3 is shown to agree well with the Fermi-Dirac solution from $n/N_0 = 10^{-6}$ to 0.5. It should be noted that Eq. 4.3 has a best fit for weakly localized carriers ($\alpha \sim l$) and small a_{DOS} ; for strongly localized carriers with a large a_{DOS} , Eq. 4.3 has a significant deviation from the exact solution. Combining Eqs. 4.1 and 4.3, the hole concentration can be written as:

$$n = N_0 \exp\left(-\frac{S}{k/q}\right), \quad (4.4)$$

and the relation between S and σ can be derived by incorporating Eq. 4.4 into $\sigma = qn\mu$:

$$S = -\frac{k}{q} \ln \sigma + \frac{k}{q} (\ln \mu + \ln q N_0). \quad (4.5)$$

Equation 4.5 demonstrates the characteristic slope of $-k/q$ in the plot of S vs. $\ln \sigma$, illustrated by the dotted lines in Fig. 4.4a, in which other parameters (e.g., μ) are constant. Since q and P_0 are known constants, μ can be extracted from the y-intercept in the S vs. $\ln \sigma$ plot, and the bulk mobility (in contrast to the field effect mobility) can be estimated.

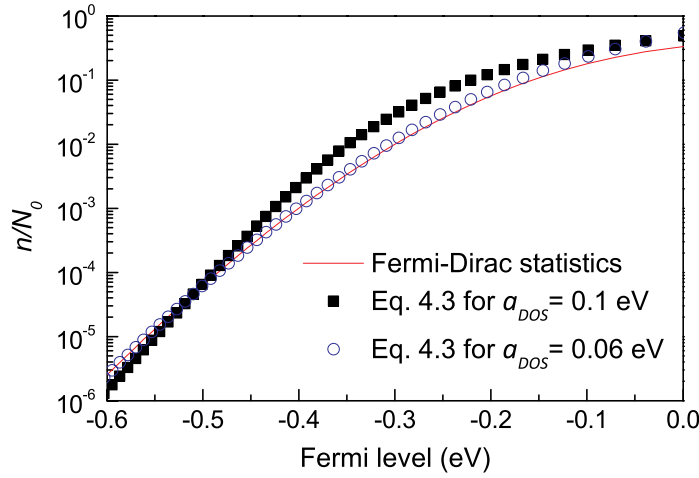


Figure 4.3 | Comparison between n/N_0 calculated by Fermi-Dirac statistics and the Boltzmann approximation. n/N_0 calculated by Fermi-Dirac statistics (solid line), by Eq. 4.3 for $a_{DOS} = 0.1\text{eV}$ (closed squares), and by Eq. 4.3 for $a_{DOS} = 0.06\text{eV}$ (open circles). The center of the Gaussian DOS is set to 0 eV (i.e., $n \approx 0.5N_0$ at $E_F = 0$), and $E_{tr} - E_F$ was numerically calculated for $\alpha = 1.5l$ (Chapter 3) and $r = 1$, which was incorporated in Eq. 4.3.

4.2.2 Transition from an activated to an intermediate hopping regime

Figure 4.4a plots S over a wide range of σ (measured during iodine dedoping), from which two distinct transport regimes are observed for different grain sizes (explained below). The characteristic slope, $-k/q$, in Eq. 4.5 is valid only when μ is independent of the hole concentration. If μ changes with carrier concentration, the slope of the S vs. $\ln \sigma$ plot changes depending on the sign of $d\mu/dn$. As can be seen in Fig. 4.4a, the majority of data follows the $-k/q$

line, implying that μ is constant for these data points. However, the data starts deviating from the $-k/q$ line at low electrical conductivities for the film with larger grain sizes (0.5 and 0.8 μm), while this deviation occurs at high electrical conductivities for the smaller grain size sample (0.2 μm). These deviations fall above the $-k/q$ line and therefore indicate an increase in carrier mobility.

This increase in carrier mobility is further supported by examining the different dependences of S and σ on dedoping time (Fig. 4.4b). The high vapor pressure of iodine has been shown to lead to spontaneous evaporation (dedoping) of iodine from a pentacene film at a rate of $Ct^{-\delta}$, where C and δ are positive constants and t is the dedoping time [98]. Assuming that the carrier concentration is proportional to the iodine concentration, S in Eq. 4.4 can be expressed as a function of the dedoping time:

$$S = \frac{k}{q} \delta \ln t - \frac{k}{q} \ln \frac{bC}{P_0}. \quad (4.6)$$

Equation 4.6 demonstrates a linear increase in S with logarithmic dedoping time. As can be seen in Fig. 4.4b, S measured during dedoping indeed linearly increase with $\ln t$, demonstrating that the spontaneous iodine dedoping occurs at the rate of $Ct^{-\delta}$. Similar to S , $\ln \sigma$ is expected to linearly increase with $\ln t$ if μ is constant, as σ is a linear function of carrier concentration: $\sigma = p\mu q = bCt^{-\delta}(\mu q)$. However, the measured $\ln \sigma$ deviates from this linear line, suggesting a change in carrier mobility (Fig. 4.4b).

The doping concentration at which deviation of measured data from the $-k/q$ line occurs depends on the degree of static disorder. For the small grain sample (0.2 μm), the carrier mobility

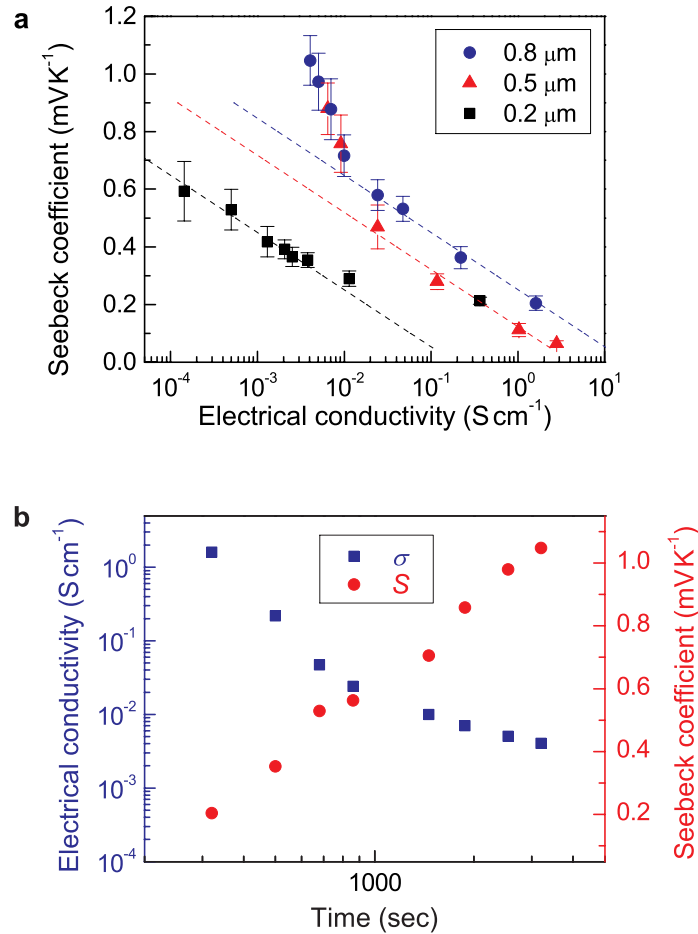


Figure 4.4 | Seebeck coefficient and electrical conductivity during iodine dedoping. (a) Seebeck coefficient versus electrical conductivity in doped pentacene films of various grain sizes. **(b)** The rate of change in the Seebeck coefficient and the electrical conductivity during iodine dedoping.

increases at high doping concentrations, which is consistent with hopping transport by strongly localized carriers. This carrier mobility increment at high carrier concentrations occurs more strongly for the highly localized carrier, since the dependence of the hopping probability on the inter-site distance becomes stronger for smaller α . In contrast to small grain pentacene, negligible deviation from the $-k/q$ line was observed at high doping concentrations in the large grain samples (0.5 and 0.8 μm), indicating negligible increase in mobility at high carrier concentrations, which is consistent with weakly localized carriers. Instead, the data in these large grain pentacene samples noticeably deviates from the $-k/q$ line at low electrical conductivities,

which suggests increased carrier mobility at low doping concentrations. This increased carrier mobility at low doping concentrations is direct evidence of impurity scattering, which further indicates that the size of the carrier wave function is on the order of the molecule spacing (i.e., an intermediate hopping regime). To the best of the author's knowledge, this is the first observation of impurity scattering in a doped OSC.

Figure 4.5 plots the carrier mobility as a function of carrier concentration in doped pentacene bulk films with various grain sizes. As is clear from the figure, the dependence of charge carrier mobility on dopant (carrier) concentration in large grain pentacene is distinct from that in the small grain pentacene. For small grain pentacene, the size of the localized wave function is small due to considerable static disorder; the carrier concentration dependence of mobility follows the activated regime as it increases at high carrier concentrations. For large grain size pentacene, the size of the localized wave function is on the order of the molecular spacing, since the static

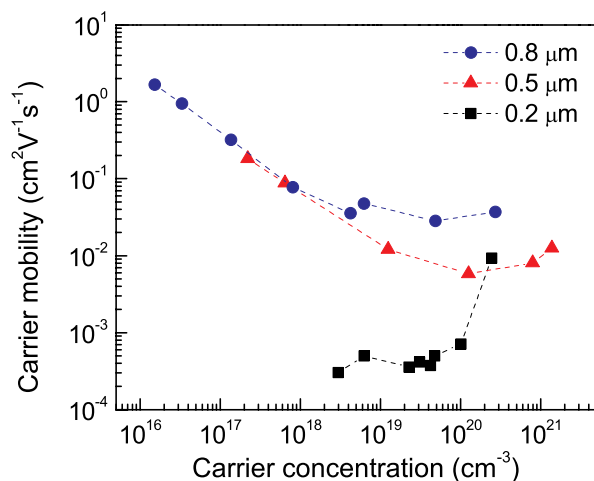


Figure 4.5 | Dependence of carrier mobility on carrier concentration for various grain sizes. The increase in carrier mobility at low concentrations in large grain size pentacene indicates the presence of impurity scattering and hence a weakly localized carrier wave function (i.e., $\alpha > l$).

disorder is small and the wave function size is primarily governed by dynamic disorder. For this weakly localized carrier, carrier transport follows the intermediate hopping regime as the carrier mobility is nearly constant at high carrier concentrations and increases at low impurity concentrations. These two distinct transport regimes found in pentacene films with different grain sizes show the effect of static disorder on carrier localization as well as the transition from an activated to an intermediate hopping regime depending on the static disorder.

In order for a localized wave function to experience impurity scattering, its size must be similar to or larger than the inter-dopant distance. As can be seen in Fig. 4.5, impurity scattering occurs down to the carrier concentration of 10^{16} cm^{-3} , implying that α is comparable to the inter-dopant distance at a dopant concentration (n_d) of $1/b \times 10^{16} \text{ cm}^{-3}$, where b defines the number ratio of free charge carriers to dopants. To estimate the inter-dopant distance ($\approx n_d^{-1/3}$), the dopant concentration (n_d) must first be calculated, for which we can recall Eq. 3.15 [77]:

$$\frac{n}{n_d} = b = \exp(-E_a / kT) = \exp\left[-(E_{a,\max} - \beta n_d^{1/3}) / kT\right], \quad (4.7)$$

where $E_{a,\max}$ is the maximum activation energy of the dopant at dilute concentrations and β captures the dependence of E_a on n_d . For $E_{a,\max}$, the exciton binding energy for the pentacene, (0.5 eV [99]) is used. To calculate β , the ratio of iodine to pentacene that saturates the electrical conductivity is used (i.e., σ does not increase after iodine/pentacene = 3, [98]), leading to $\beta = 3.9 \times 10^{-8} \text{ eV cm}^{-1}$. With these two parameters, the carrier concentration in Fig. 4.5 is converted to iodine concentration, and their relationship is plotted in Fig. 4.6. As can be seen Fig. 4.6, a carrier concentration of 10^{16} cm^{-3} occurs at an Iodine concentration of $2.35 \times 10^{20} \text{ cm}^{-3}$ (i.e., $b = 4.26 \times 10^{-5}$). Assuming that the ratio of the iodine volume to the pentacene molecule is proportional to their weight ratio ($V_{\text{Iodine}}/V_{\text{pentacene}} \approx M_{w,\text{Iodine}}/M_{w,\text{pentacene}} = 0.46$), this iodine

concentration of $2.35 \times 10^{20} \text{ cm}^{-3}$ yields an inter-dopant distance of $1.8l$. While Fig. 4.5 does not provide the carrier concentration at which μ stops increasing, the derived α of $1.8l$ indeed represents the intermediate hopping regime, and furthermore is very close to the α ($= 1.5l$) derived for the $\text{F}_4\text{-TCNQ}$ doped pentacene bulk films and the pentacene FETs using the Seebeck model in Chapter 3.

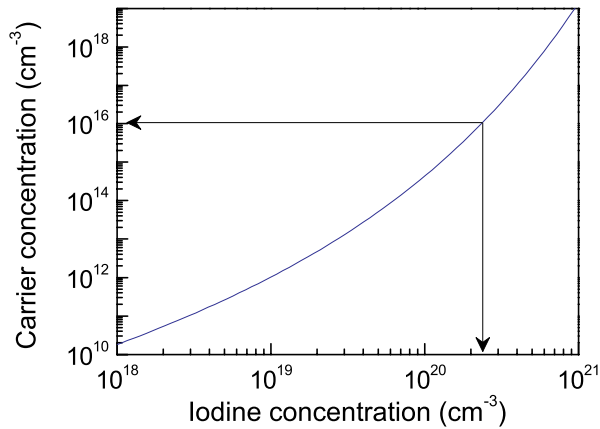


Figure 4.6 | Required iodine concentration for $n = 10^{16} \text{ cm}^{-3}$. The dependence of n on the Iodine concentration is calculated by Eq. 4.7, based on which the required iodine concentration for $n = 10^{16} \text{ cm}^{-3}$ is $2.35 \times 10^{20} \text{ cm}^{-3}$.

Chapter 5

High-performance polymer-based thermoelectric materials

A thermoelectric device is a solid-state heat engine that directly converts heat to electricity and vice versa. Since thermoelectric generators can easily utilize heat at low temperatures (i.e., waste heat), which is a large portion of the available heat energy, they are expected to play an important role in meeting future green energy needs. Nanostructuring [1, 2] and other advanced techniques and ideas such as phonon-glass/electron-crystal [100] have dramatically increased the thermoelectric figure-of-merit (ZT) in inorganic semiconductors (ISCs), yet material scarcity and hence high price hinder their practical usage. In order to utilize the abundant waste heat using a thermoelectric heat engine, both their performance and cost-effectiveness should be improved.

Organic semiconductors (OSCs) are based on earth-abundant elements and have other benefits such as low weight, mechanical toughness, and capability for large-area deposition. ZT in OSCs has rapidly been improving since 2011 [13, 20, 22, 25], and their device-level energy conversion efficiency has this year been proven by Fujifilm to be high enough for practical applications (2013) [21]. This chapter will present the minimization of dopant volume as a new approach to enhance thermoelectric efficiency in OSCs [20].

5.1 Previous achievements and limitations in thermoelectric materials

A thermoelectric material should be a good electrical conductor to carry electricity efficiently, and at the same time, a poor thermal conductor to minimize energy leakage from a heat source to a heat sink. These two requirements are usually in conflict with each other, since they are linearly proportional to each other (i.e., Wiedemann-Franz law), and while the electrical conductivity (σ) increases with material crystallinity, this also increases the thermal conductivity (κ). Furthermore, the Seebeck coefficient (S) usually has an inverse relationship with carrier concentration, causing an increase in S to generally lead to a decrease in σ . These conflicts between the thermoelectric parameters result in difficulties in maximizing ZT ($= S^2\sigma T/\kappa$, where S , σ , T , and κ are the Seebeck coefficient, electrical conductivity, absolute temperature, and thermal conductivity, respectively). Therefore, improving one of the three parameters without sacrificing the others has been a primary goal in the thermoelectric community.

In the early 1990s, Hicks and Dresselhaus pointed out the positive effects of nanostructures on thermoelectric efficiency [1, 2], which was later experimentally demonstrated as a means to alter one thermoelectric parameter without significantly affecting the others [101], leading to relatively large enhancements in the thermoelectric efficiency [102-105]. A new material class, the so-called phonon-glass/electron-crystal, was shown to reduce κ without decreasing σ by using heavy ions with large vibrational amplitudes in the lattice cage to create effective phonon scattering sites [100, 106].

Despite these notable improvements in thermoelectric materials, their impact has been questioned because of the currently low thermoelectric energy conversion efficiency compared to other existing technologies for power generation [107]. Also, it has been pointed out that the

high efficiencies gained in nanostructured materials are often difficult to scale-up with reasonable cost [3]. All these arguments boil down to the question of the cost-effectiveness in thermoelectric devices, since a thermoelectric power generator can utilize abundant waste heat energy at low temperatures that cannot in general run a traditional steam engine. If a thermoelectric device were reasonably cheap, it would have an economic advantage over conventional heat engines for many applications.

The fact that traditional thermoelectric materials are mostly based on elements which are rare in the earth's crust is a major obstacle to widening their applications. For example, one of the most popular elements in current thermoelectric materials, tellurium, is as rare as gold (Fig. 1.3). Many abundant elements have been investigated to lower the cost of thermoelectric materials; the second most abundant element (silicon) got much attention as its κ was found to be 2 orders of magnitude smaller in a nanowire geometry than its bulk value [5, 108]. Recently, OSCs, which are primarily based on carbon, hydrogen, and oxygen, have begun to be considered as promising candidate thermoelectric materials [13, 20, 21, 25]. Since OSCs are solution-processible, their manufacturing costs are low and large-area deposition on a complicated shape is relatively straightforward.

5.2 Sample preparation and characterization

Accurate measurement of the three thermoelectric parameters is essential to characterizing a material's thermoelectric properties; their amplitudes should be accurate and all three parameters should be measured in the same direction. To satisfy these requirements, S , σ , and κ were all

differentially determined (i.e., the sample length was varied to obtain a signal only from the sample), and were measured in the same direction (in-plane, i.e., parallel to the substrate).

5.2.1 Sample preparation

Samples were first prepared by mixing pristine poly(3,4-ethylenedioxythiophene) :poly(stylenesulphonate) (PEDOT:PSS) (Clevios PH1000 from H. C. Stark; 1:2.5 mass ratio) with 5 volume% of EG or dimethyl sulphoxide (DMSO) to enhance σ [88]. These mixtures were subsequently filtered by a syringe filter (0.45 μm pore-size PVDF membrane), then vigorously shaken using a vortex mixer for 15 minutes, and kept in vacuum for 15 minutes to remove air bubbles. For electrical measurements (S and σ), thin films were prepared by spin-coating at 4000 rpm for 30 seconds on a glass, pre-cleaned with detergent, deionized water, acetone, and isopropanol. For thermal measurements (κ), thick films were prepared by spin-coating multiple layers (each layer spin-coated with the same conditions of 4000 rpm for 30 seconds) in order to achieve a large thickness. A pre-cleaned silicon substrate ($\kappa \approx 150 \text{ W m}^{-1} \text{ K}^{-1}$) was used for thermal conductivity measurements to reduce the temperature rise across the substrate and thereby increase the measurement signal-to-noise ratio. The silicon substrate was capped by a 100 nm SiO_2 layer to have similar surface properties as the glass substrate used for the electrical measurement samples. All substrates (glass and silicon) were UV-ozone treated for 15 minutes after the cleaning process. To maintain the film anisotropy between the electrical and thermal samples, the spin coating conditions were kept the same, and the film thickness was controlled by the number of spin-coated layer rather than the spin-coating parameters (time and RPM). For doping-dependent cross-plane thermal conductivity (κ_y) measurements, a film thickness of approximately 180 nm was made by spin-coating three times. For in-plane thermal conductivity

(κ_x) measurements, a film thickness of approximately 1.4 μm (required to probe the anisotropic thermal conductivity using a metal line heater with 3 μm width) was made by spin-coating 45 times. Note that the multi spin-coating yielded a smaller individual layer thickness since the topmost annealed layer was partially removed during each spin-coating. Each spin-coated layer was thermally annealed at 130 $^{\circ}\text{C}$ for 15 minutes. These heated samples were immediately immersed in an ethylene glycol (EG) bath for a given time to induce a desired doping level. All of the above film preparation procedures including EG treatment were done in nitrogen gas, while the electrical and thermal measurements were done under atmospheric conditions.

5.2.2 Sample geometry

To perform differential measurements for S and σ , two gold electrodes were deposited by an electron-beam evaporator and separated by various lengths ($L = 60, 80, 100, \text{ or } 120 \mu\text{m}$) (Fig. 2.4b). The width of each electrode was 1.2 mm and its length was $(3\text{mm} - L)/2$. After gold deposition, the spin-coated PEDOT:PSS film was trimmed to have an area of 2.2 mm width \times 3 mm length, in order to isolate the electrically conductive PEDOT:PSS film from the thermocouples with which temperature data was collected. Given the fact that the PEDOT:PSS thickness was much smaller than L and the conductances of the gold electrodes were much larger than that of the PEDOT:PSS film, 1-dimensional (1D) electric conduction between the two electrodes was assumed, and the sample geometries were defined by 1.2 mm width \times L length \times d thickness. Even though the films were quite smooth and flat as shown in AFM images (Fig. 5.3)), the thickness of each was measured in three different regions using a Dektak profilometer and the average thickness was used for d . To facilitate 1D electric conduction and test whether the electrode geometry influenced the measured results, the PEDOT:PSS film was further

trimmed to have an area of 1.2mm width \times 3mm length, making the width of the PEDOT:PSS identical to 1.2mm electrode width. No significant changes in the measured S and σ were observed. Additionally, electrodes with a different aspect ratio (1.2mm width \times 100 μm length) were also tested, and the measured S and σ remained almost unchanged.

5.2.3 Determination of S

A Peltier cooler ($300\text{ K} - \Delta T_0$) and Peltier heater ($300\text{ K} + \Delta T_0$) were used to produce a 1D temperature gradient across the substrate. A liquid-cooled copper heat sink was thermally anchored to the bottom of the two Peltier units to produce a stable temperature gradient. Two microthermocouples of 25 μm diameter were mechanically attached to the sample surface and separated by D_{TC} . Note that these thermocouples have a sufficiently small diameter that error due to air convection is minimal (Chapter 2). A linear 1D temperature gradient across the sample was confirmed by measuring the temperature difference between two thermocouples (ΔT_{TC}) separated by different values of D_{TC} (1, 2, 3, 4, and 5 mm); $\Delta T_{TC}/D_{TC}$ was found to be constant over the tested D_{TC} . This linear temperature gradient ($\Delta T_{TC}/D_{TC}$) was then used to calculate the temperature difference across the electrode spacing ($\Delta T = L \times \Delta T_{TC}/D_{TC}$). Error in ΔT is small, since the magnitudes of D_{TC} and ΔT_{TC} are much larger than their errors. Two thermocouples were placed outside of the trimmed PEDOT:PSS film to electrically isolate them from the voltage probes with which the thermal voltage was measured.

To measure the thermal voltage across the electrode spacing (ΔV) induced by ΔT , two thin gold wires (25 μm diameter, 20 mm length), one end of which was thermally and electrically shorted to a bulk probe, were brought into contact with the gold electrodes. The main reason this thin gold wire was used (rather than directly contacting the electrodes with the bulk probes) is to

remove the parasitic thermal voltage across the gold electrode. Since no oxide layer forms on the gold electrode and it therefore has a very low thermal interface resistance with the gold wire, and the heat leakage to the thin gold wire is very small, the temperature differences across the electrodes are mostly cancelled out by the temperature differences along the thin gold wires. They (electrode and thin gold wire) have the same S , and therefore the parasitic thermal voltages across the electrodes and gold wires are cancelled out by each other (Chapter 2). The separation distance between two thin gold wires was set to make the thermal voltage for $L = 0$ negligible (Fig. 2.4d). The Seebeck voltage across the electrode spacing (ΔV) was found to linearly increase with the spacing length L (Fig. 2.6b) indicating negligible net parasitic Seebeck voltage, and S was derived by a linear fit to measured ΔV versus ΔT for various L (Fig. 2.6c).

5.2.4 Determination of σ

A differential measurement technique was used to determine the electrical conductivity according to its definition; resistance = $\rho \times L/A$, where A is the cross-sectional area of the PEDOT:PSS film and ρ is the electrical resistivity, and $\sigma = 1/\rho$. The electrical resistance for each electrode spacing was determined by the standard 4-point probe method and found to linearly increase with L (Fig. 2.6a).

5.2.5 Determination of doping-dependent cross-plane thermal conductivity κ_y

A differential 3ω method was used to remove uncertainties in the thermal properties of other layers when measuring the doping-dependent cross-plane thermal conductivity κ_y . A sample region that has a PEDOT:PSS film and a reference region that does not have a PEDOT:PSS film

were prepared near each other to minimize effects of substrate variation on the measured data (Chapter 2). A gold line of 50 μm width \times 2.6 mm length was patterned on both the sample and the reference region. To electrically isolate the heater line from the conductive PEDOT:PSS film, a thin Al_2O_3 layer was deposited on the sample by atomic layer deposition. Figure 2.7 illustrates the sample geometries for the κ_y measurement. The temperature rise across the PEDOT:PSS film (ΔT_f) due to the heating power (P_s) was calculated by subtracting the temperature rise measured on the reference region (ΔT_r) from the temperature rise measured on the sample region (ΔT_s) [109]:

$$\frac{\Delta T_f}{P_s} = \frac{\Delta T_s}{P_s} - \frac{\Delta T_r}{P_r}, \quad (5.1)$$

where the subscripts f , s , and r denote the PEDOT:PSS film, sample region, and reference region, respectively. ΔT_r was found to decrease with the logarithm of frequency [53], and ΔT_s was found to be offset from ΔT_r by a frequency-independent constant that corresponds to ΔT_f . As can be seen in Fig. 5.1, the magnitude of ΔT_f is larger than the sum of the other temperature rises (i.e., $\Delta T_f > \Delta T_s - \Delta T_r$), improving the reliability of the measurement. Heat conduction from the 50 μm wide heater line to the substrate via a very thin PEDOT:PSS layer (< 200 nm) is likely 1D, for which κ_y can be simply calculated by Fourier's conduction law:

$$\kappa_y = P_s \cdot d_f / (w_h l_h \cdot \Delta T_f), \quad (5.2)$$

where d_f is the film thickness and w_h and l_h are the width and length of the line heater, respectively. The film thickness was measured in 3 different regions by a Dektak profilometer, and the average value was used for d_f .

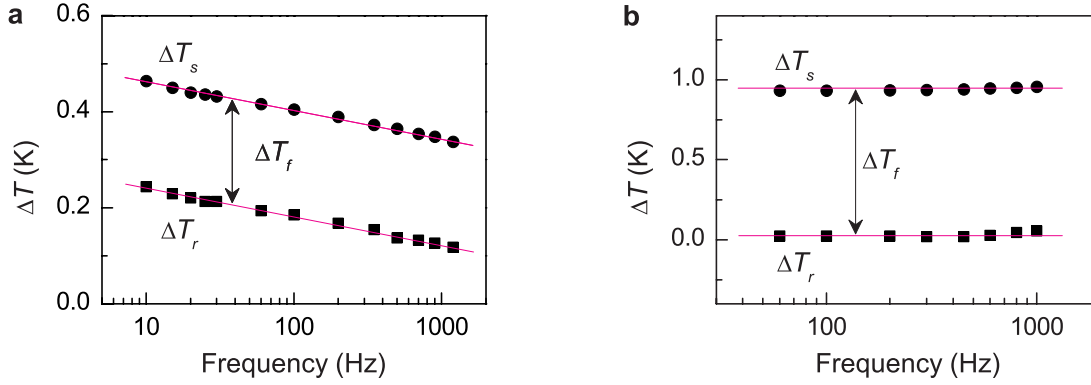


Figure 5.1 | Temperature rise across the PEDOT:PSS layer. (a) Temperature rise across the thin sample used for the cross-plane κ measurement, and **(b)** across the sample used for the in-plane κ measurement. The difference between the temperature rise of the heater line on the sample region (circles) and that on the reference region (squares) was used to calculate the frequency-independent temperature rise across the sample layer (ΔT_f).

5.2.6 Determination of in-plane thermal conductivity κ_x

Electrical samples were prepared by spin-coating, and S and σ were measured in the in-plane direction. Since the centrifugal force during spin-coating is expected to cause a morphological anisotropy and hence an anisotropic thermal conductivity, κ should be measured in the same in-plane direction in order to obtain a true value of ZT . To probe the anisotropic thermal conductivity, two metal lines of different widths were deposited on the sample and the reference regions (Fig. 2.7). For the wide line (50 μm width), heat conduction was 1D and the temperature rise in the heater line was measured by the same procedures as described in Section 5.2.4. For the narrow line (2.1 μm width for DMSO-mixed samples and 3.0 μm width for EG-mixed samples), additional heat conduction in the in-plane direction is not negligible, and hence its temperature rise is smaller than that of the wide heater line. The magnitude of the difference in temperature rise between the narrow and the wide heater lines can be related to the anisotropy in heat conduction, from which the in-plane thermal conductivity (κ_x) can be derived (Fig. 2.9); detailed equations are given in the Section 2.4.5.

For pristine EG-mixed PEDOT:PSS, the anisotropy ratio κ_x/κ_y was found to be 2.30 ± 0.47 , while $\kappa_y = 0.227\pm 0.002 \text{ Wm}^{-1}\text{K}^{-1}$, yielding $\kappa_x = 0.52\pm 0.11 \text{ Wm}^{-1}\text{K}^{-1}$. For pristine DMSO-mixed PEDOT:PSS, the anisotropy ratio κ_x/κ_y was found to be 1.73 ± 0.27 , while $\kappa_y = 0.242\pm 0.002 \text{ Wm}^{-1}\text{K}^{-1}$, yielding $\kappa_x = 0.42\pm 0.07 \text{ Wm}^{-1}\text{K}^{-1}$. Note that κ_y in these thick films were measured to be smaller than those measured in the thin films, which is presumably caused by the larger interface density in the thick films. Since the spin-coating conditions used for the thick films and thin films were kept the same, the measured κ_y in the thick films was assumed to be equal to κ_y in the thin films [110, 111], yielding the anisotropy ratio $\kappa_x/\kappa_y = 1.62\pm 0.35$ for the pristine EG-mixed PEDOT:PSS thin sample and $\kappa_x/\kappa_y = 1.40\pm 0.22$ for the pristine DMSO-mixed PEDOT:PSS thin films. Given the fact that the dedoping is expected to occur isotropically, these anisotropy ratios were assumed to not change during EG treatment, and used to calculate κ_x from the measured κ_y at different dedoping levels. These derived κ_x at different dedoping levels were then used to derive the doping-dependent ZT in the in-plane direction.

5.2.7 Analysis of XPS spectra

X-ray photoelectron spectroscopy (Kratos Axis Ultra XPS) was used to analyze the chemical compositions of PEDOT:PSS at different dedoping levels. The known intensity ratio of the S_{2p} doublet in PEDOT:PSS ($S_{2p,3/2} : S_{2p,1/2} = 2:1$ [112]) was fixed during the deconvolution, and the relative intensity ratios at known different binding energies (PEDOT: 162-166 eV and PSS: 166-170 eV) were used to obtain monomer ratios. These monomer ratios were then used to determine the ratio of PSS to PEDOT (χ) in PEDOT:PSS at different dedoping levels (Fig. 5.2).

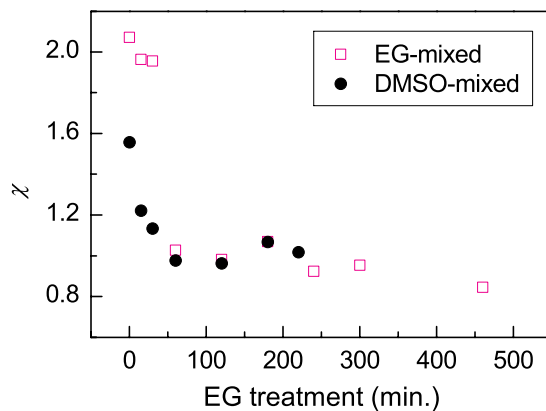


Figure 5.2 | Ratio of the PSS monomer to PEDOT monomer (χ) at different EG treatment times. XPS was used to obtain χ .

5.2.8 Morphology of EG-treated PEDOT:PSS

Film morphology and chemical composition were investigated by atomic force microscopy (AFM) using a Bruker ICON AFM. The AFM phase image is known to distinguish areas of PEDOT and PSS, as they have different viscosities [111]. As can be seen in Figs. 5.3a and 5.3c, no significant change in morphology was observed after EG treatment, whereas the chemical composition changed considerably based on their AFM phase images; the area of the bright regions significantly increases after 120 minutes of EG treatment. Since PSS is electrically insulating, this increase in the PEDOT-rich (bright) region reduces the tunneling distance and hence exponentially enhances carrier mobility.

5.2.9 Stability of EG-treated PEDOT:PSS in atmosphere

PEDOT:PSS is known to be stable in air. To assess the effect of EG treatment on its air-stability, S and σ in the 180 minute EG-treated PEDOT:PSS were measured at different air-exposure

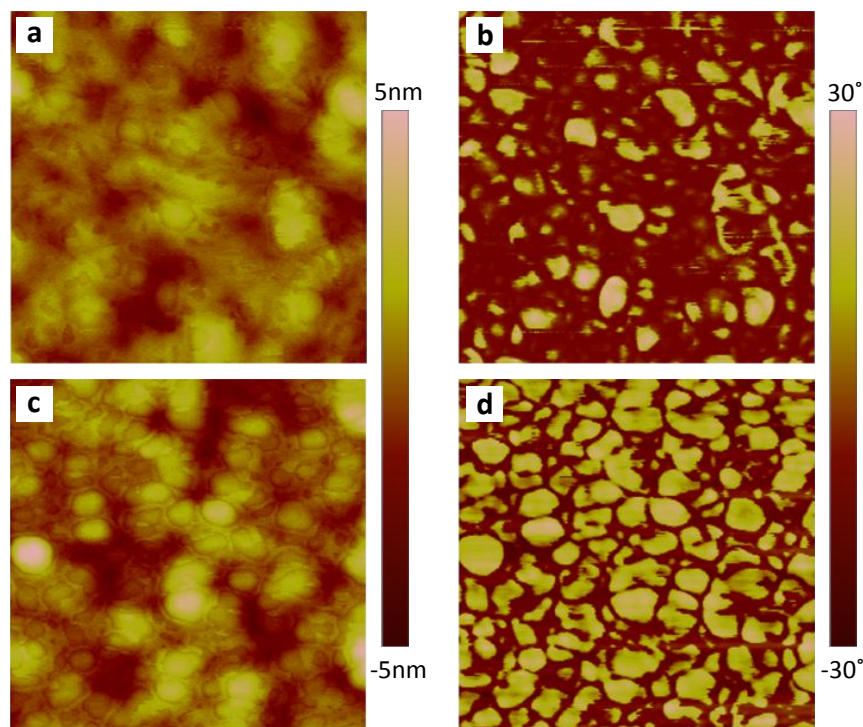


Figure 5.3 | Tapping-mode AFM images (500nm × 500nm) for PEDOT:PSS. (a) Tapping-mode AFM topography (surface roughness $R_a = 0.81\text{nm}$) and (b) phase images in a pristine PEDOT:PSS film. (c) Tapping-mode AFM topography (surface roughness $R_a = 1.16\text{nm}$) and (d) phase images in a PEDOT:PSS film EG-treated for 120 minutes. The bright regions in the phase images correspond to PEDOT-rich areas, while the dark regions correspond to the PSS-rich matrix. The samples used for the AFM measurement are made of EG-mixed PEDOT:PSS. $r\chi$, S , and σ were measured to be 3.34, 19.7 $\mu\text{V K}^{-1}$, and 597 S cm^{-1} in the pristine PEDOT:PSS (a and b), while they are measured to be 1.48, 36.2 $\mu\text{V K}^{-1}$, and 1309 S cm^{-1} in the EG-treated sample (c and d).

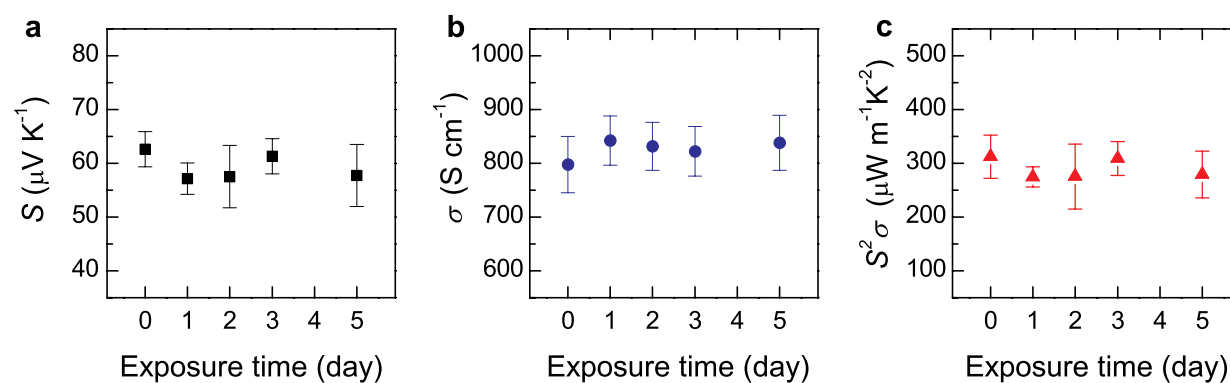


Figure 5.4 | Effect of the EG treatment on the air-stability of PEDOT:PSS. (a-c) S , σ , and $S^2\sigma$ measured at different air-exposure times in PEDOT:PSS which had been EG-treated for 180 minutes.

times. The measured S and σ were found to be nearly constant for 5 days (Fig. 5.4), indicating that PSS dedoping does not compromise the air-stability of PEDOT:PSS.

5.3 Dopant volume as an engineering parameter for organic thermoelectric materials

Together with the carrier concentration (n), carrier mobility (μ) is a fundamental engineering parameter in thermoelectric materials and governs the maximum possible ZT . While optimizing n is a well-known step required for maximizing $S^2\sigma$, the effect of finite dopant volume on μ and hence on $S^2\sigma$ in OSCs has not previously been explored, although the hopping probability exponentially decreases with hopping distance. Below, the effect of dopant volume on $S^2\sigma$ in OSCs is quantified and used to calculate the optimal doping (or dedoping) trajectory.

5.3.1 Optimal carrier concentration for maximum $S^2\sigma$ in OSCs

In thermoelectric materials, an optimal carrier concentration ($n_{optimal}$) that maximizes $S^2\sigma$ exists, because S and σ have opposite dependences on n . To realize $n_{optimal}$, the carrier concentration is tuned by chemical doping, which often affects μ and thereby leads to a dependence of μ on n which can vary depending on the nature of carrier transport. For crystalline ISCs, the carrier wave function is fully extended, and μ decreases with n because of increased impurity scattering at high dopant concentrations. For OSCs in which the carrier wave function is localized, the dependence of μ on n is opposite; μ continuously increases with n until the detrimental effect of dopant volume on μ becomes overwhelming.

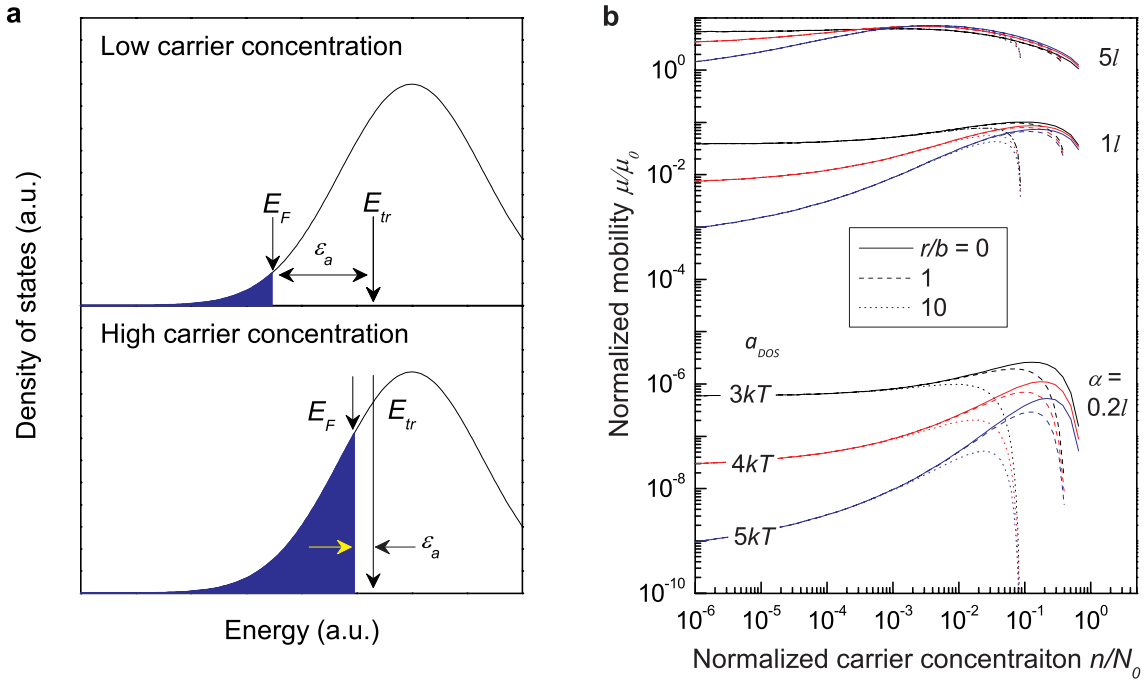


Figure 5.5 | Hopping activation energy (ϵ_a), carrier mobility (μ), and carrier concentration (n). (a) Dependence of ϵ_a on n . (b) Dependence of μ on n/N_0 for various degrees of carrier localization, Gaussian DOS widths (a_{DOS}), and dopant volumes required for a certain n (r/b). While μ increases with n in general, a small b (or large r) leads to a profound decrease in μ at high n . This effect of r/b is greater for strongly localized carriers (i.e., small α).

Since the hopping probability exponentially decreases with hopping distance, a localized carrier tends to hop to the nearest vacant site near room temperature. In the energy domain, this preference of a small hopping distance encourages carriers to jump to higher energy states at which the number of vacant state is large and hence the averaged distance between vacant states is small: the averaged inter-state distance = (density of state)^{-1/3}. Because of the exponential characteristic of the Gaussian DOS tail, a reasonably small hopping distance occurs at energy states roughly within a standard deviation of the center of the Gaussian DOS. In other words, the localized carrier needs to hop to an energy state near the center of the Gaussian DOS in order to find a vacant site within a small spatial distance (Fig. 5.5a), and the difference between the average energies of the initial states ($\sim E_F$) and the final states ($\sim E_{tr}$) defines the hopping

activation energy. As carrier concentration increases, E_F approaches E_{tr} , and the hopping activation energy becomes smaller, leading to a larger carrier mobility. Figure 5.5b shows the super-linear increase in the carrier mobility with n , the magnitude of which depends on the degree of carrier localization (α).

This additional mobility enhancement in OSCs makes the dependence of $S^2\sigma$ on n very strong, and results in a much larger $n_{optimal}$ (relative to the total DOS) compared with $n_{optimal}$ in ISCs (Fig. 5.6). For this reason, OSCs need to be both heavily and precisely doped in order to maximize $S^2\sigma$. It should be noted however that heavily doped OSCs can be quite different from heavily doped ISCs; heavily doped OSCs can have more dopants than host conductive molecules because of inefficient ionization of the molecular dopants.

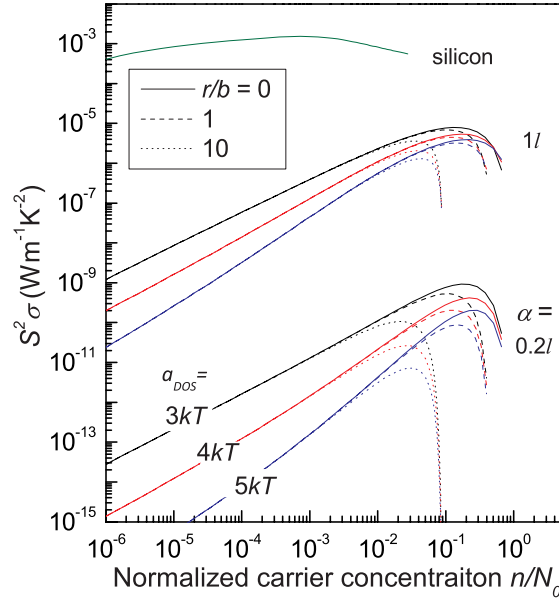


Figure 5.6 | Thermoelectric power factor for various α and r/b . The strong dependence of $S^2\sigma$ on n and very large optimal concentrations in OSCs are shown and compared with a typical ISC (silicon). Also shown is the significant effect of dopant volume (r/b) on $S^2\sigma$ in OSCs. $v_0 = 10^{13} \text{ s}^{-1}$ was used for OSCs.

5.3.2 Inefficiency of molecular doping

In a sense, doping an OSC is similar to making a composite material rather than replacing only a tiny percent of host element by impurities as in ISCs. The dielectric constant is typically much larger in ISCs than in OSCs, and therefore charge carriers contributed by dopants in ISCs are less bound to ionized dopants compared to OSCs. The dopant activation energy in ISCs is typically less than kT at room temperature, while it can be as high as several hundred meV in OSCs. At low carrier concentrations, this binding energy between the dopant and induced charge carrier is on the order of the exciton binding energy. For a range of dopant concentrations, the fraction of free charge carriers that contribute to electric conduction is given by [77]:

$$\frac{n}{n_d} = b = \exp(-E_a / kT) = \exp\left[-(E_{a,\max} - \beta n_d^{1/3}) / kT\right], \quad (5.3)$$

where $E_{a,\max}$ is the maximum activation energy of the dopant at its dilute concentrations (\sim exciton binding energy) and β captures the dependence of E_a on the dopant concentration. Given the fact that the exciton binding energy in OSCs ranges from 0.2 to 1.4 eV [90], Eq. 5.3 predicts $b \ll 10^{-3}$ at dilute concentrations, indicating that most dopants do not contribute to electrical conduction. This inefficiency of molecular doping results in the fact that the number of electrically insulating dopants in heavily doped OSCs is larger than the number of conducting host molecules [89]. In other words, heavily doped OSCs are a composite of insulating dopants (which can be over 50 volume%) and conducting conjugated molecules. For example, heavily iodine doped pentacene contains 3.5 times more iodine atoms than pentacene molecules [98], and a typical weight ratio between PEDOT and its dopant PSS is 1:2.5, 1:6, or even 1:20 [88] (Fig. 5.7).

Figure 5.5b depicts the profound effect of this dopant volume on the carrier mobility. While the carrier mobility tends to increase with the carrier concentration, the inefficiency of molecular doping (i.e., $b \ll 1$) increases the dopant volume required to obtain a certain n , and consequently creates a large reduction in carrier mobility at high dopant densities.

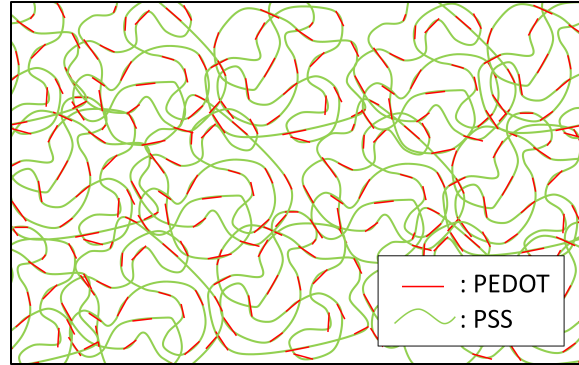


Figure 5.7 | Ratio of PSS to PEDOT in typical PEDOT:PSS. A typical PEDOT:PSS mass ratio of 1:2.5 is used for this illustration.

5.3.3 Strong dependence of $S^2\sigma$ on dopant volume

This poor doping efficiency (section 5.3.2) makes it challenging to achieve the large $n_{optimal}$ in OSCs (section 5.3.1), since excess dopants increase the hopping distance and hence significantly decrease μ (and consequently $S^2\sigma$). To quantify this increase in the hopping distance due to the finite dopant volume, we can recall Eqs. 3.7, 3.8, and 3.9:

$$R(E) = \left(\frac{4\pi}{3B} \int_{-\infty}^E g(\varepsilon) (1 - f(\varepsilon)) d\varepsilon \right)^{-1/3}, \quad (5.4)$$

where $g(\varepsilon)$ is the Gaussian DOS:

$$g(\varepsilon) = \frac{N_t(r\chi)}{\sqrt{2\pi a_{DOS}^2}} \exp\left(-\frac{\varepsilon^2}{2a_{DOS}^2}\right), \quad (5.5)$$

and the total DOS (which depends on dopant volume) is:

$$N_t(r\chi) = \frac{N_0}{1+r\chi} = \eta(r\chi)N_0, \quad (5.6)$$

where N_0 is the total DOS of the undoped host material. The variable $r\chi$ is the ratio of total dopant volume to total host molecule volume, and is given by the product of the subunit (e.g., monomer for the polymer case) volume ratio (r) and the subunit number ratio (χ). Whereas the effect of dopant volume on N_t is negligible in ISCs, the inefficiency of molecular doping leads to a large χ that significantly decreases N_t and hence increases the hopping distance (Eq. 5.4). By incorporating Eqs. 5.4, 5.5, and 5.6 in numerical calculations (Chapter 3), the dependence of $S^2\sigma$ on $r\chi$ and n can be calculated, and is illustrated in Fig. 5.8. The fact that the color contour is almost circular in an OSC means that the dependence of $S^2\sigma$ on $r\chi$ is just as strong as it is on n/N_0 , making $r\chi$ a primary engineering parameter for maximizing $S^2\sigma$. Furthermore, this plot shows the most efficient 2-dimensional doping (or dedoping) trajectory to follow for the best possible $S^2\sigma$ in a particular OSC. For example, a doping strategy should focus on increasing b for an OSC located at the upper part of the color map (i.e., vertical doping trajectory), whereas the carrier concentration should be optimized for an OSC located at the right or left part of the color map (i.e., horizontal doping trajectory). For a heavily doped OSC located at the upper right part of the color map (such as PEDOT:PSS), the dedoping trajectory should be diagonal, reducing not only n/N_0 but also $r\chi$.

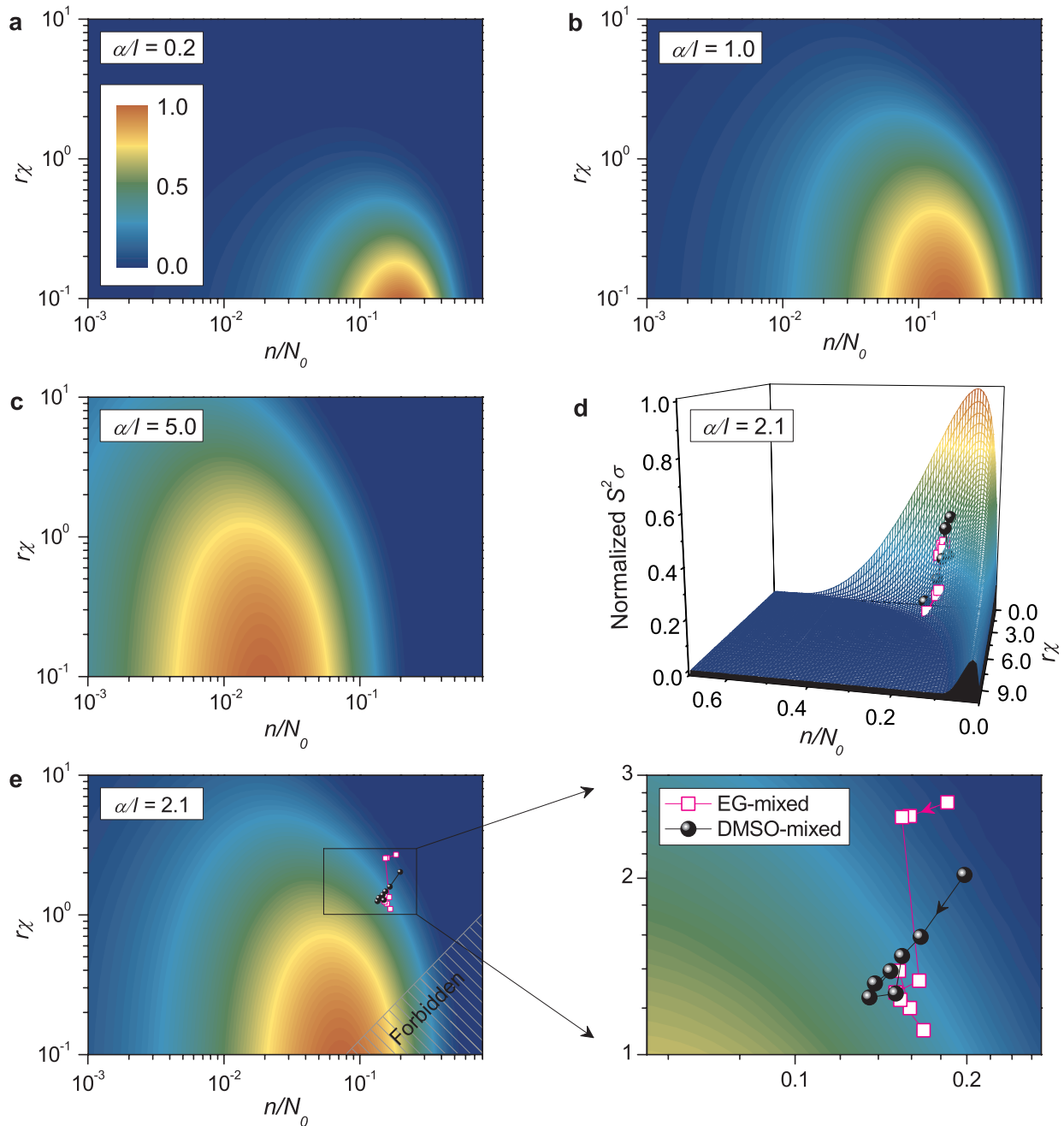


Figure 5.8 | The 2D trajectory of doping (or dedoping) for efficient maximization of thermoelectric power factor in an OSC. (a–c) Calculated [7] dependence of $S^2\sigma$ on the ratio of total dopant volume to total host volume ($r\chi$) and the normalized carrier concentration (n/N_0), for different degrees of carrier localization (α/l). Normalized $S^2\sigma$ is illustrated by the colour bar. **(d)** Three-dimensional plot of normalized $S^2\sigma$, which demonstrates the steep ascent of the dedoping trajectory along both n/N_0 and $r\chi$ axes in the direction of maximum $S^2\sigma$. **(e)** Measured dedoping trajectory for DMSO-mixed (circles) and EG-mixed (squares) PEDOT:PSS. χ is determined by XPS data and numerical calculation [7] is used to derive n/N_0 from a fit to the measured S . The non-physical condition of $n/N_0 > \chi$ for $r = 1.3$ is indicated by the forbidden area. The arrows in the magnified image represent the time evolution of the data during the EG treatment dedoping process.

5.4 Effects of reduction in dopant volume on ZT

In general, enhancement in one thermoelectric parameter leads to unfavorable changes in the other two parameters. For example, an increase in σ typically results in both a decrease in S by its characteristic dependence on σ (the $-k/q$ slope appearing in Eqs. 3.14 and 4.6) and also an increase in κ by the Wiedemann-Franz law. In OSCs, these general trade-offs are not necessarily true; for example, the Wiedemann-Franz law has been found to be invalid in OSCs [113]. Below, the positive effects of minimizing dopant volume on thermoelectric performance in OSCs are experimentally demonstrated; it is shown that all three parameters (S , σ , κ) vary in a manner that increases ZT , leading to a very high ZT at room temperature [20].

5.4.1 Selective removal of PSS

Minimizing total dopant volume is key to improving low values of $S^2\sigma$ measured previously in PEDOT:PSS (1 to 50 $\mu\text{W m}^{-1}\text{K}^{-2}$ [17, 19, 114, 115]), while control of PSS concentration and hence carrier concentration is difficult owing to the large molecular weight and long chain length of PSS [111].

The hydrophilic nature of PSS allows a hydrophilic solvent such as ethylene glycol (EG) to separate PSS from PEDOT (which is hydrophobic) [116]. After thermal annealing, samples for electrical and thermal measurements were immediately immersed in an EG bath for a given time to induce desired dedoping levels. As the dedoping time increases, the sample thicknesses (for both the electrical and thermal samples) decreased as shown in Fig. 5.9, indicating the selective removal of PSS during the EG treatment. This selective removal of PSS from PEDOT:PSS was

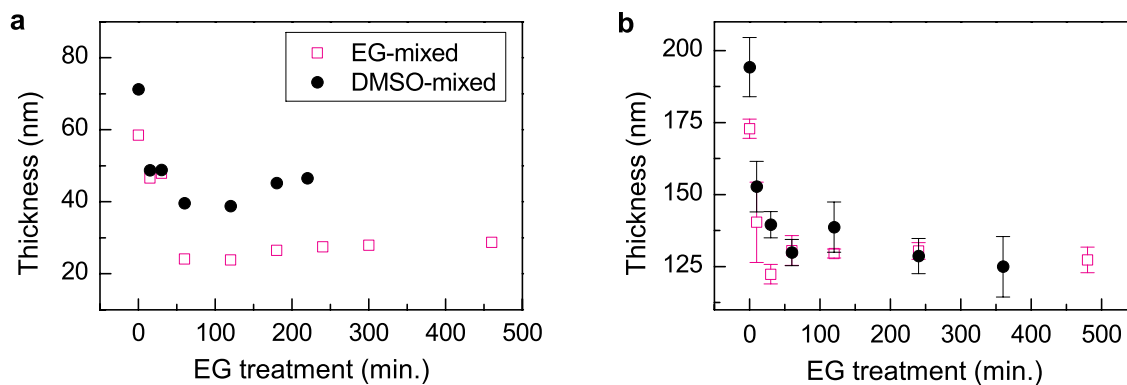


Figure 5.9 | Thicknesses of PEDOT:PSS at different EG treatment times. (a) PEDOT:PSS used for electrical measurements. **(b)** PEDOT:PSS used for the cross-plane thermal conductivity measurement. The error bar for the thermal sample thickness is calculated by the standard deviation of thicknesses measured at 3 different regions, while the electrical samples are very smooth (surface roughness $R_a \sim 1$ nm (Fig. 5.3)).

confirmed by separate XPS measurements, as the intensity of the sulphur atom (S_{2p}) from the sulphonate group in PSS (166-170 eV) decreased with respect to the intensity of the S_{2p} from the thiophene group (162-166 eV) with longer EG treatment time (Fig. 5.10). This decrease in the PSS peak intensity with respect to the PEDOT peak intensity is direct evidence of PSS dedoping by the EG treatment. While the PSS peak intensity decreased with respect to the PEDOT peak intensity during the first 60 minutes of the EG treatment, the relative intensity of the PSS and PEDOT became 1-to-1 and remained almost unchanged after 60 minutes of EG treatment, indicating that the EG treatment no longer removed PSS after this time. It is likely that, as more PSS is removed by EG treatment, a larger area of the hydrophilic PSS chain is surrounded by the hydrophobic PEDOT, making the hydrophilic EG solvent less effective in selectively removing PSS. After the PEDOT and PSS reached a 1-to-1 ratio, the EG treatment was no longer effective, and therefore the film thickness (Fig. 5.9), XPS data (Figs. 5.2 and 5.10), and Seebeck coefficient (Fig. 5.11a) all remained nearly constant after this point.

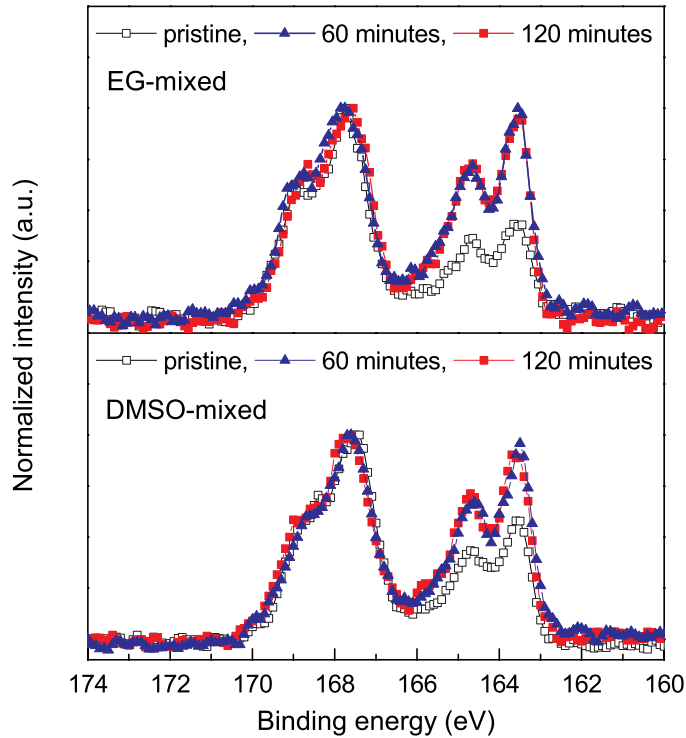


Figure 5.10 | S_{2p} XPS spectra in pristine PEDOT:PSS and EG-treated PEDOT:PSS. The intensity ratio of the high binding energy peak (sulfur atom in PSS) to the low binding energy peak (sulfur atom in PEDOT) decreases with longer EG treatment times.

5.4.2 S and σ increase while κ decreases, causing ZT to increase

The dedoping trajectory during the EG-treatment was tracked in order to examine its effectiveness. Assuming that the volume ratio of the PSS monomer to the PEDOT monomer is equal to their molecular weight ratio (PSS: 182, PEDOT: 140), $r\chi$ during the dedoping process was calculated. The normalized carrier concentration (n/N_0) was obtained by fitting the measured S to a numerically calculated value [7]. The carrier localization length normalized by the molecular spacing (α/l) was set to 2.1, because its magnitude is not significantly affected by dopant type and chemical additives, as discussed in Section 3.3 [7, 84].

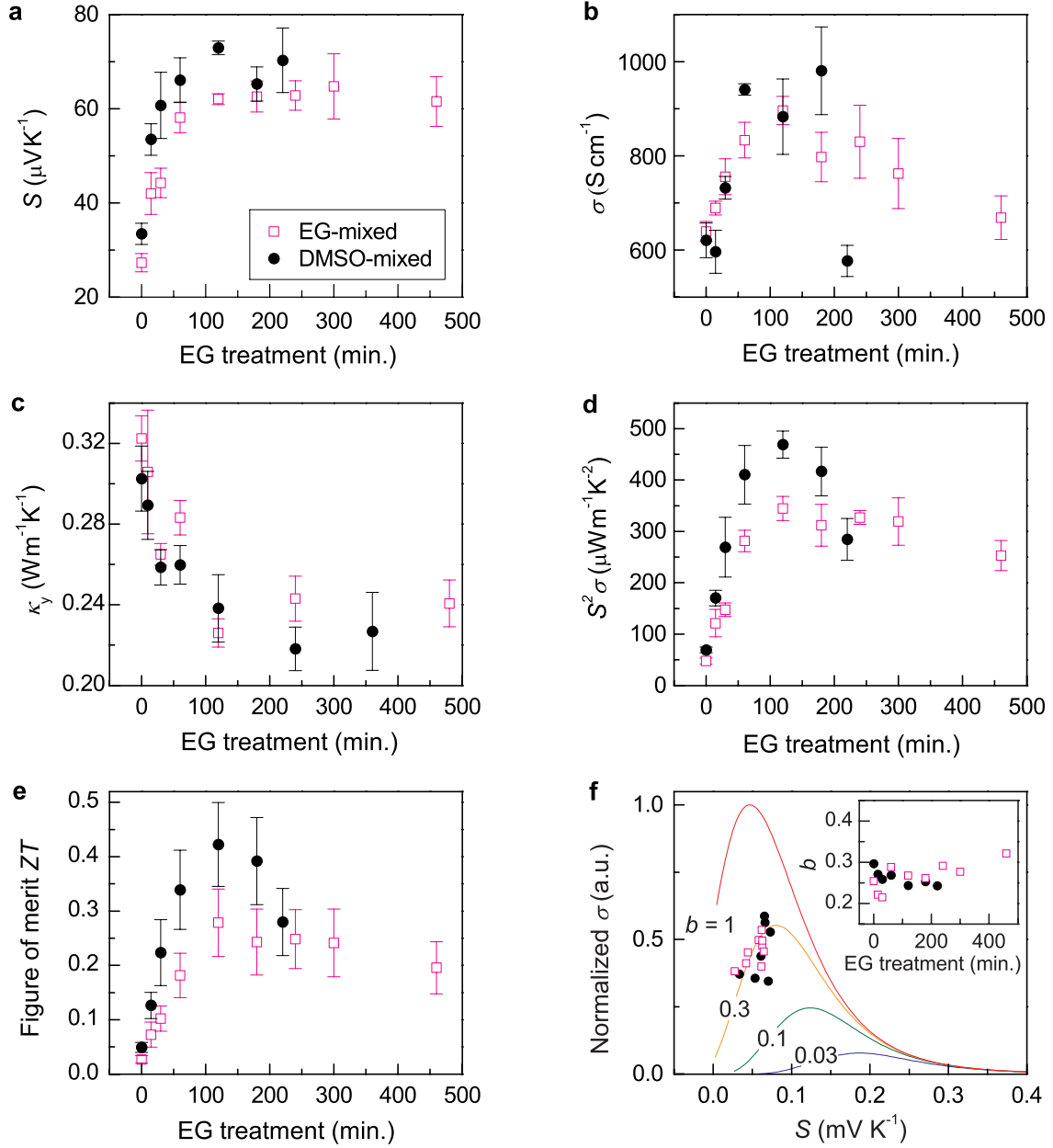


Figure 5.11 | Thermoelectric properties of PEDOT:PSS at various dedoping times. (a) Seebeck coefficients, **(b)** electrical conductivities, **(c)** cross-plane thermal conductivities, **(d)** thermoelectric power factors, and **(e)** thermoelectric figure-of-merit at $T = 297$ K in EG-mixed and DMSO-mixed PEDOT:PSS. ZT was derived from in-plane thermal conductivities (same direction of measured $S^2\sigma$). The standard deviation of measured data from the linear fit line (Fig. 2.6) was used to determine error bars for S and σ . The standard deviations of measured temperature rise at different frequencies and thicknesses (Fig. 5.9) were used to determine error bars for κ_y . **(f)** Calculated [7] σ (normalized by maximum value for $b = 1$) as a function of S for different magnitudes of b (assuming $r = 1.3$). Also shown are S and σ measured in EG-mixed and DMSO-mixed PEDOT:PSS. Inset: derived b during EG-treatment.

As can be seen in Fig. 5.8e, the dedoping trajectory for both EG-mixed and DMSO-mixed PEDOT:PSS aims directly at the maximum $S^2\sigma$, resulting in significant enhancements in $S^2\sigma$ (Figs. 5.8d and 5.11d). As the EG treatment was not able to reduce PSS below the 1-to-1 ratio, the dedoping trajectory stopped at $\chi = 0.96$ and $n/N_0 = 0.13$; at this point, $S^2\sigma$ in the DMSO-mixed PEDOT:PSS reaches $469 \mu\text{Wm}^{-1}\text{K}^{-2}$, which is approximately half of the calculated maximum $S^2\sigma$. If the n/N_0 is reduced to 0.07 and $b \sim 1$ (i.e., $r\chi$ is minimized), $S^2\sigma$ is predicted to be as high as $1100 \mu\text{Wm}^{-1}\text{K}^{-2}$, which is close to the measured $S^2\sigma = 1270 \mu\text{Wm}^{-1}\text{K}^{-2}$ in electrochemically modulated PEDOT transistors [25]. Although transistor geometries are not practical as thermoelectric devices, achieving such high performance in a bulk OSC (which would bring ZT close to 1) could have large impact.

In ISCs, $d\sigma/dS$ is typically negative, particularly near $n_{optimal}$ since μ is almost constant there ($\sim 10^{-3}N_0$, Figs. 3.2 and 5.6) and hence the opposite dependences of S and σ on n are preserved. In OSCs, $n_{optimal}$ is very large ($\sim 0.1N_0$), and the typically large number of dopants present due to small b (Eq. 5.3) strongly affects μ (Fig. 5.5b). In both EG-mixed and DMSO-mixed PEDOT:PSS, S and σ were found to simultaneously increase as PSS was removed (Figs. 5.11a and 5.11b), indicating that the significant increase in μ due to reduced hopping distance overwhelms the reduction in n . This unique trend of positive $d\sigma/dS$ occurs in OSCs at high doping concentrations (Fig. 5.11f) and is caused by their large $n_{optimal}$, small b , and large molecular dopant volume.

In addition to this simultaneous increase in S and σ , the cross-plane thermal conductivity κ_y was found to decrease with decreasing PSS concentration (Fig. 5.11c). Measured κ_y in the pristine EG-mixed and DMSO-mixed PEDOT:PSS were 0.32 and $0.30 \text{ Wm}^{-1}\text{K}^{-1}$, respectively, which decreased to 0.23 and $0.22 \text{ Wm}^{-1}\text{K}^{-1}$, respectively, as PSS dedoping progressed. This decrease in

κ is ascribed to the much larger molecular weight of PSS ($\sim 400000 M_w$) than PEDOT ($\sim 2000 M_w$) and to changes in nanostructures within the PEDOT:PSS. The much larger molecular weight of PSS implies that PEDOT:PSS with less PSS contains a greater ratio of VDW bonds to covalent bonds compared to PEDOT:PSS with more PSS. Since the bonding strength of the VDW bond is much weaker than the covalent bond, κ in PEDOT:PSS with less PSS is expected to be smaller. Additionally, PEDOT:PSS films are known to form nanostructures in which PEDOT-rich regions are surrounded by PSS-rich shells [111]. During PSS removal, the thicknesses of the PSS-rich shells likely decrease, leading to a larger nano-interface density and hence smaller κ .

The derived anisotropy ratio κ_x/κ_y was used to convert κ_y , measured at different doping levels to κ_x , which was then used to derive ZT . Using the three thermoelectric parameters that were measured in the in-plane direction, a maximum ZT of 0.42 was derived for the DMSO-mixed PEDOT:PSS and 0.28 for the EG-mixed PEDOT:PSS, the former being the highest ZT yet reported among OSCs. This high value of ZT suggests the importance of minimizing dopant volume ($r\chi$) in maximizing ZT , which has been shown above to simultaneously enhance all three parameters constituting ZT .

Chapter 6

Thermally conductive amorphous plastics

While previous chapters primarily discussed methods to tune the electronic portion of ZT ($S^2\sigma$), the thermal portion (κ) likewise shows promise for tunability, as shown by its dependence on doping discussed earlier (Fig. 5.11c). In fact, tuning of thermal conductivity has been the primary means by which ZT has been increased in ISCs over the past several decades. Beyond the field of thermoelectric materials, however, the impact of improving thermal conductivity in organic materials on their applications and product price is significant. Previous efforts on this topic have mainly focused on adding species that have high κ [36, 117, 118], yet this approach has the potential problems of increasing product price and altering other physical properties (e.g., physical strength, electrical conductivity, transparency) in an undesirable manner. Very large values of κ were measured in crystalline polymer fibers [41, 42], but this crystallization is hard to achieve using a traditional low-cost thermal molding process.

This chapter discusses a method to alter the thermal conductivities of amorphous organic materials by engineering intermolecular interactions [119]. While the primary context for the work discussed is to strengthen intermolecular interactions in order to improve κ in amorphous organic materials, analogous methods to weaken intermolecular interactions could be developed to reduce κ (and thus improve ZT) in thermoelectric polymers. Since the method discussed is primarily based on polymer chemical structure and does not require the additional crystallization

of polymer chains, it can be directly applied to common manufacturing processes such as thermoforming and injection molding. The experimental demonstration of the proposed strategy shows a significant increase in κ for mixtures of several commercially popular polymers: poly(methyl methacrylate) (PMMA) mixed with poly(vinyl alcohol) (PVA) and poly(acryloyl piperidine) (PAP) mixed with poly(acrylic acid) (PAA). Furthermore, replacing van der Waals bonding to hydrogen bonding results in simultaneous enhancement in the polymer chain packing in a nanoscale, leading to κ for the mixtures over $1 \text{ Wm}^{-1}\text{K}^{-1}$ ($1.17 \text{ Wm}^{-1}\text{K}^{-1}$ for the PMMA/PVA mixture and $1.72 \text{ Wm}^{-1}\text{K}^{-1}$ for the PAA/PAP mixture), more than a factor of 5 larger than the thermal conductivities of the individual constituents ($\sim 0.2 \text{ Wm}^{-1}\text{K}^{-1}$). These high values of κ suggest that improving intermolecular interactions can be a powerful engineering route to increasing κ in organic materials.

6.1 Impacts of thermally conductive organic materials on the plastics industry

As discussed in previous chapters, organic-based materials have numerous benefits compared to other materials. They are based on earth-abundant elements, are solution processible, and can be easily formed to various shapes at relatively low temperatures, all of which contribute to low cost. In addition to this cost advantage, plastics (which are primarily made of organic materials) have other performance attributes such as low weight, mechanical toughness, and flexibility. These benefits have made plastic products ubiquitous in modern life, where cheap and tough plastic materials continue to replace conventional materials (e.g., metals and ceramics) in many applications. The market size of the plastics industry also continues to grow; for example, the

current market size of plastic automobile parts is estimated to be \$15.1 billion, which is expected to grow to \$32.9 billion by 2018 [120].

Applications requiring efficient heat transfer are one of the relatively few remaining areas in which organic materials cannot effectively replace metals and ceramics. Components used at high power densities (e.g., automobile cooling systems and high power density electronics) need to dissipate heat efficiently in order to achieve high performance and long-term reliability. For these applications, current organic materials are not adequate, since their low thermal conductivity leads to undesirable temperature increases and can also contribute to product failure due to the low melting temperatures of most organic materials; the aforementioned market size of plastic automobile parts mainly involves interior and exterior furnishings. For this reason, thermal interface materials used in high power density conditions are mainly composed of metals or ceramics, yet their high price, weight, and limited machinability motivate the continued study of alternative thermal interface materials.

Given the aforementioned benefits of organic materials, developing a method to increase κ in these materials without significant added cost will contribute to a reduction in cost for certain thermal management applications and further improve the functionality of existing plastic products. Efforts have been made to replace the metal-based cooling system in vehicles with alternative materials in order to reduce weight and hence increase fuel efficiency [121]; for these efforts, increasing the currently low thermal conductivities of organic materials is a main challenge. Encapsulation of electronic components is another application that typically uses plastics due to their low cost and machinability; likewise, device performance and lifetime could benefit from plastic encapsulants with increased thermal conductivity. Many other products

require efficient heat dissipation (e.g., smartphone cases and LED bulb housings) yet are made of plastic due to low cost and machinability, and could benefit from increased thermal conductivity.

In addition to better performance in applications for which heat management is important, high thermal conductivity in organic materials is expected to decrease the price point of plastic products, as most plastic products are thermally machined (e.g., thermoforming, injection molding). In general, the price of plastic products increases super-linearly with their size, since the time required for heating and cooling the plastic part during thermal molding increases the manufacturing time, causing the final product price to be more than the cost of the plastic material used. The limitation of heat transfer during thermal molding is particularly significant for thick plastic products. For example, the molding cycle of an automobile part, which includes the heating time to form the part and the cooling time to solidify the part, is on the order of minutes rather than seconds [35], greatly increasing the manufacturing time and hence the part's cost. Since the molding time decreases with increasing κ of the solid polymer [122], developing a method for increasing thermal conductivity that is applicable to typical manufacturing methods (e.g., thermoforming, injection molding) and which does not sacrifice other physical properties (e.g., mechanical strength) may decrease the overall cost of plastic products and therefore significantly affect the plastics industry.

6.2 Previous efforts to improve κ in organic materials

Since high κ has numerous potential benefits in the plastics industry, many researchers and companies have tried to improve κ in organic materials. Primarily two different approaches have

been taken for this purpose: one using a filler of high κ (e.g., silver particles or graphene flakes), and the other using aligned polymer chains.

6.2.1 High- κ filler method

In general, dispersing high- κ fillers randomly within a polymer matrix leads to an increase in κ . Common materials studied as fillers include high- κ metal particles [36], carbon nanotubes (CNTs) [117], and graphene (or graphite) flakes [118], the basic purpose being to form a continuous thermally conductive pathway [38]. This percolation mechanism implies that a minimum volume fraction of fillers is required to improve κ in a composite. Unfortunately, the κ resulting from this filler method is far lower than a simple average of the thermal conductivities of the polymer matrix and filler; for spherical metal particle fillers, κ of the polymer-filler composite above the percolation threshold is on the order of $1 \text{ Wm}^{-1}\text{K}^{-1}$ [36]. CNT and the graphene flake fillers achieve similarly low values of κ [117, 118], suggesting the presence of a large interface thermal resistance between the filler and polymer matrix that presents a barrier to overall heat conduction [123]. In addition to this inefficiency of the filler method, a large amount of filler material is required to exceed the percolation threshold, leading in some cases to a large increase in the material cost (e.g., CNTs cost \sim \\$1000/kg while nylon66 costs \sim \\$2/kg) and undesirable changes in other physical properties (e.g., color, electrical conductivity). For example, the percolation threshold is approximately 20–30 volume% for spherical fillers, which corresponds to over 90 weight% for typical metal and polymer densities.

6.2.2 Crystalline organic materials

Another approach is to crystallize a plastic to increase κ . The thermal conductivity of an individual polymer chain has been predicted to be as high as hundreds of $\text{Wm}^{-1}\text{K}^{-1}$ in the chain

direction [40], indicating that a crystalline plastic may have large κ in the direction of polymer chain alignment. Mechanical stretching has been shown to align polymer chains in a thin film, leading to a fewfold increase in κ in the stretched direction [124]. For plastic fibers composed of aligned polymer chains, thermal conductivities in the direction of chain alignment were measured to be between 20 and 100 $\text{Wm}^{-1}\text{K}^{-1}$ [41, 42]. Unfortunately, crystalline plastics are practically hard to realize on a large scale with reasonable cost. Furthermore, most industrial plastic products are currently made by thermoforming and injection molding, which results in a plastic that is amorphous, thereby limiting the potential impact of crystalline plastics in their current form.

6.3 A design principle for enhanced thermal conductivity in organic materials

The large values of κ predicted for individual polymer chain (\sim few hundred $\text{Wm}^{-1}\text{K}^{-1}$) reduce to a few $0.1 \text{ Wm}^{-1}\text{K}^{-1}$ when the chains are dangled with each other and form a bulky material. This drastic decrease in κ of 3 orders of magnitude is evidence of a large contribution to low κ in plastics: the weak van der Waals (VDW) interactions between polymer chains. This motivates the consideration of improving this weak VDW intermolecular interaction as a means to improve κ in plastic materials.

6.3.1 Model for κ as a function of intermolecular junction conductance

Polymeric materials can be thought of as a bundle of randomly dangled 1-dimensional (1D) polymer chains. The junction between two chains is defined by the VDW interaction, which has a certain thermal conductance. Given the huge difference in κ between an individual polymer

chain and its bulk form, the temperature drop across the junction is expected to be much larger than the temperature drop along the chain for a given heat flux. For this junction-dominated heat conduction, the overall heat transfer can be expressed as [125]:

$$\langle q_{H,x} \rangle = -\sigma_H \langle n_x \rangle \langle N_J \rangle \langle \Delta T \rangle / 2, \quad (6.1)$$

where $\langle q_{H,x} \rangle$ is the heat flux through a given plane (A) that is perpendicular to the x -coordinate, $\langle n_x \rangle$ is the average number of polymer chains that pass through plane A , $\langle N_J \rangle$ is the average number of junctions on a polymer chain, and $\langle \Delta T \rangle$ is the average temperature difference between two junctions. The quantity σ_H is the junction thermal conductance (unit: WK^{-1}), which is expected to be proportional to the junction strength [123]. For a plastic in which two polymers are randomly mixed, the total heat flux is the sum of three heat fluxes:

$$\langle q_{H,x,1} \rangle = -\sigma_{H,1} \langle n_{x,1} \rangle \langle N_{J,1} \rangle \langle \Delta T_1 \rangle / 2, \quad (6.2a)$$

$$\langle q_{H,x,2} \rangle = -\sigma_{H,2} \langle n_{x,2} \rangle \langle N_{J,2} \rangle \langle \Delta T_2 \rangle / 2, \quad (6.2b)$$

$$\langle q_{H,x,C} \rangle = -\sigma_{H,C} \langle n_{x,C} \rangle \langle N_{J,C} \rangle \langle \Delta T_C \rangle, \quad (6.2c)$$

$$\langle q_{H,x,total} \rangle = \langle q_{H,x,1} \rangle + \langle q_{H,x,2} \rangle + \langle q_{H,x,C} \rangle, \quad (6.2d)$$

where the subscripts “1”, “2”, and “C” denote the heat flux between chains of polymer 1, between chains of polymer 2, and between polymer 1 and polymer 2 chains. $\langle \Delta T \rangle$ can be split into two components: ∇T_x , which is the temperature gradient along the x -axis, and $\langle \Delta x_J \rangle$, which is the orthogonal projection of the average distance between junctions on the x -axis: $\langle \Delta T \rangle = \nabla T_x \langle \Delta x_J \rangle$ [125]. The three quantities $\langle n_x \rangle$, $\langle N_J \rangle$, and $\langle \Delta x_J \rangle$ are dependent on polymer

geometry; to enable analytic expressions, the polymer chain is assumed to be a perfect 1D rod with a radius of R_P and a length of L_P . This assumption of a 1D rod is later adjusted by correction factors. Assuming the same L_P and R_P for two polymer chains ($L_{P1} = L_{P2} = L_P$ and $R_{P1} = R_{P2} = R_P$), these three quantities can be expressed for $R_P/L_P \approx 0$ (since the polymer chain is assume to be very long) as:

$$\langle n_{x,1,2} \rangle = f_a \frac{n_{1,2} L_P}{2}, \quad (6.3a)$$

$$\langle n_{x,C} \rangle = f_a \frac{n_1 L_P}{2}, \quad (6.3b)$$

where n_I is the concentration of polymer 1, and the concept of excluded volume [126] can be used to calculate $\langle N_J \rangle$ and $\langle \Delta x_J \rangle$:

$$\langle N_{J,1,2} \rangle = n_{1,2} \pi R_P L_P^2, \quad (6.4a)$$

$$\langle N_{J,C} \rangle = n_2 \pi R_P L_P^2, \quad (6.4b)$$

with $\langle \Delta x_J \rangle$ given by:

$$\langle \Delta x_{J,1,2} \rangle = \langle \Delta x_{J,C} \rangle = f_b \frac{L_P}{\pi^2}. \quad (6.5)$$

The correction factor f_a is an unitless constant which represents a decrease in the number of polymer chains passing through plane A due to their randomly coiled shape; its magnitude is inversely proportional to the chain length: $f_a \sim 1/L_P$. The correction factor f_b is a unitless constant which represents the finite temperature drop along the chain that becomes non-negligible for large L_P ; its magnitude is inversely proportional to the chain length: $f_b \sim 1/L_P$.

The total heat flux for the randomly dangled semi-infinite 1D chains is expressed by:

$$\langle q_{H,x,total} \rangle = -C \frac{R_p L_p^2 \nabla T_x}{4\pi} (\sigma_{H,1} n_1^2 + \sigma_{H,2} n_2^2 + 2\sigma_{H,C} n_1 n_2), \quad (6.6)$$

where C is a constant (unit: m^2) originating from the correction factors f_a and f_b . From Eq. 6.6, κ_x for a di-polymeric material is given by:

$$\kappa_x = C \frac{R_p L_p^2}{4\pi} (n_1^2 \sigma_{H,1} + n_2^2 \sigma_{H,2} + 2n_1 n_2 \sigma_{H,C}). \quad (6.7)$$

For a mono-polymeric material, κ_x can be calculated by setting $\sigma_{H,1} = \sigma_{H,2} = \sigma_H$ and $n_1 + n_2 = n$:

$$\kappa_x = C \frac{R_p L_p^2}{4\pi} (n_1 + n_2)^2 \sigma_H = C \frac{R_p}{4\pi} (n L_p)^2 \sigma_H \sim \rho_m^2 \sigma_H, \quad (6.8)$$

where ρ_m is the mass density of the polymer (which is proportional to $n L_p$) and the pre-factor $C R_p / 4\pi^2$ remains nearly constant for different polymers. For amorphous organic materials, the derived κ_x is expected to represent the isotropic scalar value of the thermal conductivity (κ) in all directions. It should be noted that Eq. 6.7 does not consider percolation, and therefore κ is expected to increase more rapidly when $\langle N_{J,C} \rangle$ exceeds the bonding percolation threshold for $\sigma_{H,1,2} \ll \sigma_{H,C}$.

6.3.2 van der Waals bonding

It is clear from Eq. 6.8 that the thermal junction conductance (σ_H) and the material mass density (ρ_m) directly determine the thermal conductivities of organic materials. For a mono-polymeric material, σ_H and ρ_m remain almost constant and correspond to the strength and the length of VDW bonding, making κ of numerous mono-polymeric materials fall within the narrow window

of 0.1 to 0.5 $\text{Wm}^{-1}\text{K}^{-1}$ [127]. In these materials, rapid heat conduction along the polymer chain (which can be considered as a stiff spring made of strong covalent bonds) is considerably damped by soft VDW springs between polymer chains. Moreover, the large VDW bonding length results in low polymer chain packing density and thereby low mass density. In this way, VDW bonding is a main factor that limits heat conduction in organic materials, suggesting that replacing VDW bonding by other types of bonding that has a larger bonding strength and a shorter bonding length such as hydrogen, ionic, or covalent bonding could greatly increase κ .

6.3.3 Hydrogen bonding

Hydrogen bonding (H-bonding) is a particularly strong dipole-dipole interaction commonly observed in polymers; its bonding strength ($12 - 30 \text{ kJmol}^{-1}$) is an order of magnitude stronger than VDW bonding ($0.4 - 4 \text{ kJmol}^{-1}$). Since interface thermal conductance has been shown to increase super-linearly with bonding strength [123], it is expected that one can manipulate $\sigma_{H,C}$ (which appears in Eq. 6.7) by replacing VDW bonds with H-bonds. To effectively increase $\sigma_{H,C}$, this H-bonding must present as inter-chain rather than intra-chain bonding. To promote this inter-chain H-bonding, two polymer chains, one containing the H-bonding acceptor (e.g., C=O) and the other containing the H-bonding donor (e.g., OH), can be mixed, with the mixture ratio tuned to maximize n_1n_2 (which corresponds to the concentration of bonds having junction thermal conductance $\sigma_{H,C}$). Furthermore, polymer packing density is known to linearly increase with H-bonding concentration because of its shorter bonding length [128], the square of which is linearly proportional to the polymer thermal conductivity because polymer mass density (ρ_m) linearly increases with the packing density (Eq. 6.7). Therefore, replacing VDW to H-bonding is expected to increase not only $\sigma_{H,C}$ but also ρ_m in Eq. 6.8, thereby leading to synergistic increase

in κ . In addition to the expected increase in κ , this strategy of enhanced inter-polymer interaction is expected to improve the mechanical toughness of the polymer, while it is not expected to decrease the thermal molding time because an increase in κ would be compensated by an increase in heat capacity (i.e., the heat diffusivity ($=\kappa/\rho_m/\text{specific heat capacity}$) remains unchanged).

6.4 Sample preparation and characterization

The goal of the sample preparations described below was to maximize $\sigma_{H,C}$ and n_1n_2 . Several commercially available polymers were chosen and mixed for this purpose, the primary pairs being:

- Mixtures of isotactic-PMMA (i-PMMA) (which contains C=O) and PVA (which contains OH)
- Mixtures of atactic-PMMA (a-PMMA) (which contains C=O) and PVA (which contains OH)
- Mixtures of PAP (which contains C=O) and PAA (which contains OH).

All mixing mol% shown below represents the molar ratio of the H-bonding acceptor and donor (i.e., monomer mol%). The differential 3ω technique was used to measure κ in samples at various mixture ratios.

6.4.1 Sample preparations

Materials

For mixtures containing PMMA, i-PMMA ($M_w = 120$ kg/mol), a-PMMA ($M_w = 15$ kg/mol), and

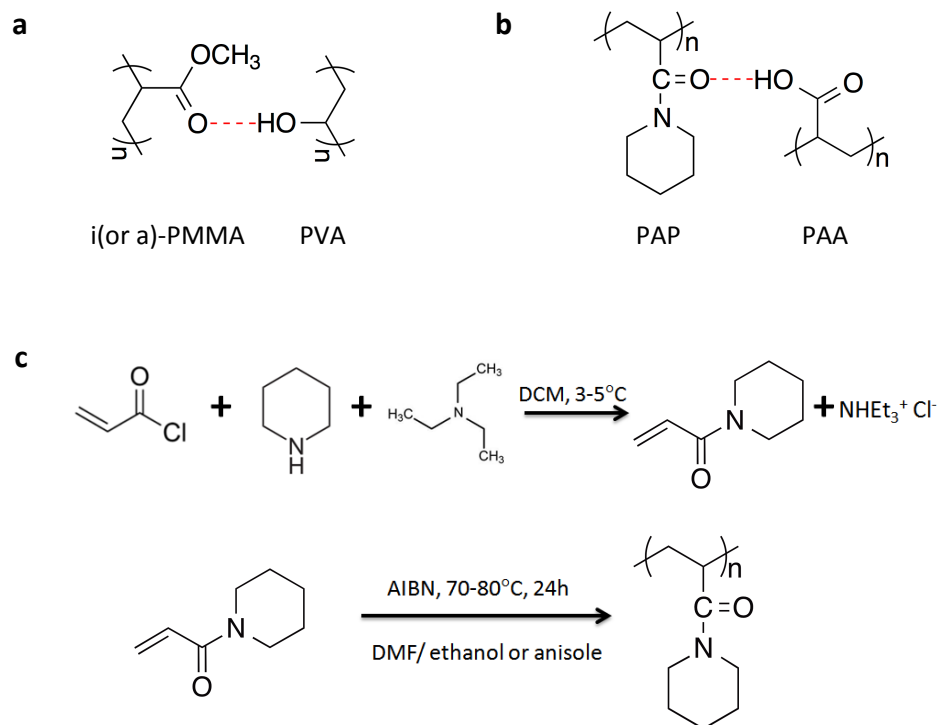


Figure 6.1 | Schematics of PMMA:PVA and PAP:PAA mixtures. (a-b) Polymer pairs that can create inter-chain H-bonding. PAA is capable of self Hydrogen-bonding within its chain, while the others are not; the self H-bonding in PVA is expected to be very weak. **(c)** Polymerization processes for PAP.

PVA (80% hydrolyzed, $M_w = 10$ kg/mol) were procured from Aldrich and used without further purification. For mixtures containing PAP, acryloyl chloride was procured from Fluka, and azobisisobutyronitrile (AIBN), piperidine, tri-ethyl amine, and PAA (viscosity averaged molecular weight $M_v = 45000$ Da) were procured from Aldrich. Dichloromethane (DCM), diethyl ether, hexane, ethyl acetate and anisole used for PAP synthesis were solvent grade. For all polymer mixtures, N,N-Dimethylformamide (DMF) (Aldrich, anhydrous, 99.8%) was used as a solvent without further purification.

PMMA:PVA solutions

1 w% of each polymer was first dissolved in DMF and heated at 150°C for 10 minutes to ensure complete dissolution. Solutions of each polymer were then mixed together with a certain

monomer molar ratio, followed by heating at 150 °C for 5 min. DMF was chosen as the solvent since both PMMA and PVA dissolve well in DMF but do not interact with each other in a solution, thereby aiding the even distribution of PMMA and PVA in a solidified film.

PAP:PAA solutions

Monomer acryloyl piperidine was synthesized according to a previously reported method [129] with some modifications (Fig. 6.1). In a typical reaction, 0.11 mol of piperidine and 0.12 mol of triethyl amine were dissolved in 100 mL dichloromethane. The solution was then added dropwise over 3 hours under constant stirring to a 7.5 mL dichloromethane solution of acryloyl chloride maintained at 3-5°C. After complete addition, the reaction mixture was stirred at room temperature for 24 hours. The product acryloyl piperidine was solvent extracted in a dichloromethane-water mixture and column separated (hexane- ethyl acetate 1:1) to yield colorless to light yellow liquid.

Acryloyl piperidine was polymerized via free radical polymerization using AIBN as an initiator (Fig. 6.1). In the polymerization process, acryloyl piperidine and AIBN were dissolved in DMF/ethanol (5:1 – 10:1) or anisole, and the solution was purged with Ar for 30 minutes. The monomer/solvent weight ratio was kept at ~20% and the reaction was carried out at 70-80°C for 24 hours. The polymer was precipitated from diethyl ether and dried under vacuum overnight.

1 w% of PAP and PAA were individually dissolved in DMF, and heated to 150°C for 10 minutes to ensure complete dissolution of the polymers. Solutions of each polymer were then mixed together with a certain monomer molar ratio, and the mixed solution was heated to 150°C for 5 minutes. Likewise PMMA:PVA mixtures, DMF was chosen as solvent, because PAP and PAA do not interact in a DMF solution, helping their even distribution in a solidified film.

Thin film formation

Solutions of mixed polymers (e.g., PMMA:PVA, PAP:PAA) were spin-coated on a Si/SiO₂ substrate pre-cleaned by detergent, acetone, and iso-propanol. The thin (100 nm) SiO₂ capping layer on which the polymers were coated was deposited on the silicon wafer to electrically isolate the bulk silicon substrate from the 3 ω metal heater. After sonication cleaning, the substrate was treated by UV-ozone to enhance the adhesion between the polymer layer and substrate. Spin-coating conditions were kept the same for all samples: 1500 rpm for 30 seconds. The resultant film thickness is plotted as a function of the mixture ratio (Fig. 6.2). Thin gold lines (50 μ m width, 2.6mm long, and 300 nm thickness) were deposited on top of the polymer film (which acted as the sample region) in one region of the substrate and on the bare SiO₂ surface (which acted as the reference region) in another region of the substrate, using an electron-beam evaporator. The sample gold line and the reference gold line were separated by about 10mm.

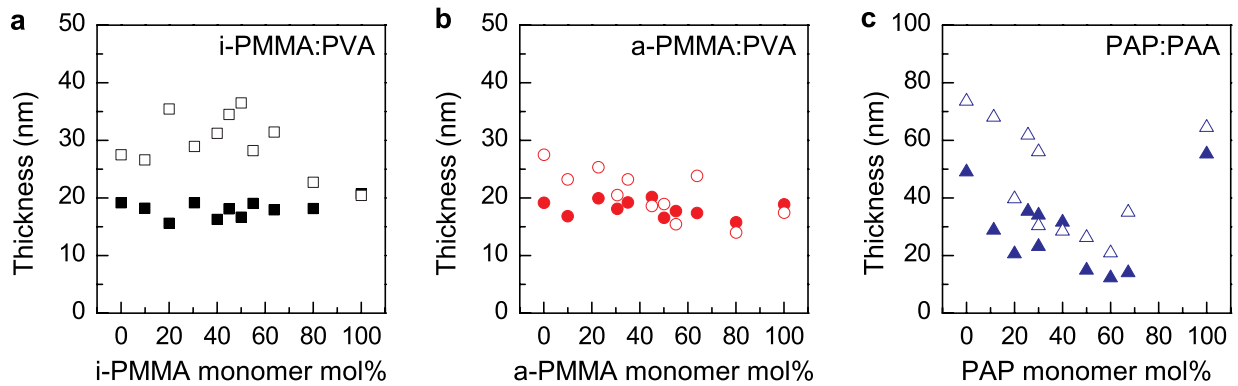


Figure 6.2 | Thickness of i- and a-PMMA:PVA and PAP:PAA. Thicknesses measured by a Dektak profilometer (open symbols) and by an ellipsometer (closed symbols) in mixtures at various mol% of the H-bonding acceptor (i.e., monomer mol% of i- and a-PMMA and PAP). Data courtesy of Lei Shao (University of Michigan).

6.4.2 Sample characterization

In this work, measurements of thermal conductivity, the film thickness, AFM, and XPS were taken on the same sample with no uncertainty in the sample variation.

Thermal conductivity measurement

As discussed in Section 2.4, the 3ω method has proven to be a reliable method for measuring κ in films with thicknesses down to several nanometers [49, 50, 130]. The differential 3ω method is particularly useful for subtracting out the thermal properties of a substrate and all layers in a sample other than those of a particular thin film of interest. By subtracting the temperature rise in the heater line on the reference region from that of the heater line on the sample region, the temperature rise across the polymer film was extracted. Since the width of the heater line ($50\ \mu\text{m}$) is much larger than the polymer film thickness (which ranged from 12.1 to 55.1 nm, measured by ellipsometry), heat conduction through the polymer film is 1D, and κ can be

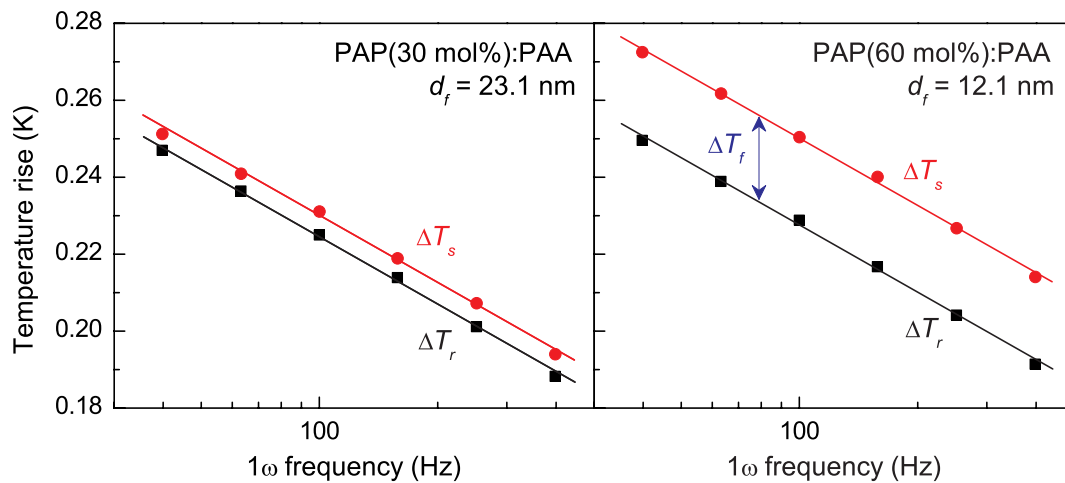


Figure 6.3 | Measured temperature rise across the PAP:PAA film. Temperature rise of the $50\ \mu\text{m}$ width heater line on the sample region (ΔT_s) (circles) and on the reference region (ΔT_r) (squares), the difference of which was used to calculate the temperature rise across the PAP:PAA film (ΔT_f). All temperature rises were induced by the same power of 0.05 W.

calculated from the measured temperature rise using Fourier's 1D conduction law (Eq. 5.2). Figure 6.3 shows the temperature rise in the heater line on the sample region (ΔT_s) and that of the heater line on the reference region (ΔT_r). Both ΔT_s and ΔT_r decrease with logarithmic frequency (ω) [53], and a frequency independent offset exists between ΔT_s and ΔT_r which represents the temperature rise across the thin polymer film ($\Delta T_f = \Delta T_s - \Delta T_r$). Note that the input powers in both the sample and reference heater lines were kept the same (0.05 W); otherwise, ΔT_f would have to be calculated using Eq. 5.1. Further experimental details are described in Chapter 2.

Thickness measurement

Thickness data is essential to the calculation of the temperature gradient from the measured ΔT_f , and therefore its accuracy is critical to the thermal conductivity data. Three different methods that are surface profilometry (Dektak surface profilometer), ellipsometry (Woollam M-2000DI ellipsometer), and atomic force microscopy (AFM) (Bruker ICON AFM) were used to measure the thickness of polymer films (d_f). Given the fact that the hardness of steel is smaller than glass but larger than plastic, a steel surgical knife was used to scratch the polymer film and make a thin groove. We tested the scratched surface by AFM, and this steel knife scratching method did not damage the glass surface at all but instead left a very thin polymer residual layer behind, and thereby the measured film thickness leads to the lower bound of κ . For the Dektak profilometer measurement, 3 different grooves were measured and averaged to obtain one thickness; for the ellipsometry measurement, the area of the 3mm \times 12mm ellipse was measured, which corresponds to the used beam spot size; for the AFM measurement, the height profile of an AFM topography image was used (Figs. 6.4e and 6.4f).

Since the polymer mixtures were designed to form a strong H-bonding interaction that can trigger the polymer chain aggregation, their surface is expected to not as smooth as the mono

polymeric film, in which weak VDW bonding is dominant. As can be seen in Figs. 6.4 (a-c), i- and a-PMMA(45 mol%):PVA(55 mol%) and PAP(30 mol%):PAA(70 mol%) spin-coated films showed small features on their surface, the lateral size of which is on the order of 1 μm , while the height is about 30 nm. Since the radii of the used Dektak stylus is 12 μm , these features cannot be precisely sensed by a Dektak profilometer. For this reason, the thickness measured by a Dektak profilometer is expected to be overestimated, which is close to the sum of the entire

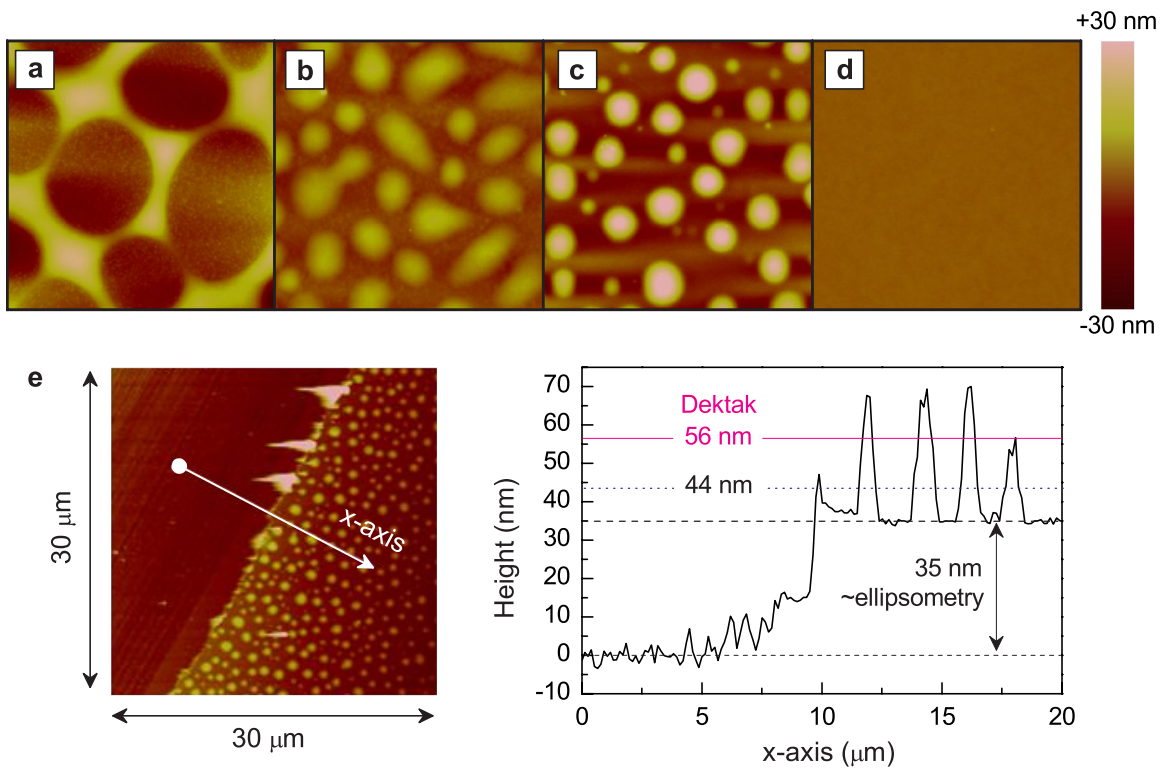


Figure 6.4 | AFM topography images for the i- and a-PMMA(45 mol%):PVA(55 mol%), the PAP(30 mol%):PAA(70 mol%), and the PAP spin-coated films. (a-d) The 5 $\mu\text{m} \times 5 \mu\text{m}$ AFM topography images for the i-PMMA(45 mol%):PVA(55 mol%) (R_a roughness = 7.72 nm) (a), the a-PMMA(45 mol%): PVA(55 mol%) (R_a roughness = 3.97 nm) (b), the PAP(30 mol%):PAA(70 mol%) (R_a roughness = 8.17nm) (c), and the PAP (R_a roughness = 0.22 nm) spin-coated film (d). (e) The 30 \times 30 μm AFM topography image of the PAP(30 mol%):PAA(70 mol%) spin-coated film, in which half of the PAP:PAA film was removed by a surgical knife. (f) The height profile of the AFM image shown in e, showing the film thickness excluding small islands to be 35nm which is consistent to the value measured by ellipsometry (34 nm). The averaged height of islands is about 30 nm, and is similar to the difference between the Dektak value (56 nm) and the ellipsometry value (34 nm). The 44 nm represents the thickness that includes the contribution from the small islands. κ of the sample shown is 1.56 $\text{W m}^{-1}\text{K}^{-1}$, calculated from $d_f = 34 \text{ nm}$.

height of the island and the smooth film thickness, while the correct value for the thermal conductivity calculation is the sum of the small feature height weighted by its lateral area and the smooth thin film thickness. As shown in Fig. 6.2, thicknesses measured by a Dektak profilometer tend to be larger than values measured by an ellipsometer, especially for mixed polymer films, the surface of which has the small islands presumably due to the formation of strong H-bonding. For this reason, values by either ellipsometry or AFM were used for thicknesses of these H-bonded films with rough surfaces (R_a roughness ~ 8 nm). As can be seen in Figs. 6.4, the AFM and the ellipsometry data agrees well with each other, and the thickness measured by ellipsometry was used for the thermal conductivity calculation in this work. It should be noted however that the measured thickness by an ellipsometer is close to the thickness of the smooth thin film that excludes the contribution from the small features (Fig. 6.4f). For this reason, κ calculated by the ellipsometry thickness is likely smaller than the actual value, since a smaller d_f makes $\Delta T_f/d_f$ larger, and hence κ smaller. For mono-polymeric films, this problem of the islands does not exist as their surface is very smooth (R_a roughness $\ll 1$ nm).

Atomic force microscopy

AFM (Bruker ICON AFM) was performed to investigate morphological and compositional properties of the mixtures. To map compositional changes, phase images in AFM tapping mode were taken; such images are known to relate to the viscoelastic properties of the sample surface and hence represent a spatial distribution of variations in polymer chains and hydrogen bonded regions. AFM images of i- and a-PMMA:PVA and PAP: PAA films are shown in Fig. 6.6; their phase images indicate the homogeneous distribution of mixed polymer chains, while the degrees of homogeneity vary with the mixture ratio and the type of the H-bonding agents.

6.5 Thermally conductive amorphous organic materials

Based on Eq. 6.7, polymer pairs with large bonding strength should be chosen to maximize interface thermal conductance ($\sigma_{H,C}$) and their relative concentrations should be controlled to maximize n_1n_2 . To facilitate strong H-bonding, the length of H-bonding needs to be minimized, suggesting that the polymer backbone chains of the two pairs should be identical to each other without large side chains.

6.5.1 Mixtures of PMMA and PVA

PMMA is often called acrylic glass and one of the most popularly used plastic materials (e.g., it is often used as a substitute for window glass). Its backbone structure has a simple linear shape without large side chains and contains a carbonyl group (C=O) on every other carbon atom (Fig. 6.1a), making it a likely candidate for strong H-bonding. PVA has an identical backbone as PMMA and contains a hydroxyl group (OH) on every other backbone carbon atom (Fig. 6.1a), making it ideal for strong H-bonding with PMMA.

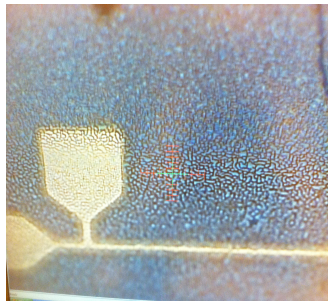


Figure 6.5 | Phase segregation occurred in the i-PMMA(30 mol%):PVA film. A thick solution with 5 weight% of polymer was used for spin-coating the film. κ was measured to be $0.24 \text{ W m}^{-1}\text{K}^{-1}$ for the sample shown here. The width of the heater line shown is $50 \mu\text{m}$.

Mixing PMMA and PVA has been shown to have many technical challenges [131], as PMMA is hydrophobic while PVA is hydrophilic. In the solutions used here, the two polymers were found to dissolve well in DMF solvent, while they were found to phase-segregate during the evaporation of the DMF solvent. When the solution was thicker (i.e., large weight%), phase segregation was more apparent. For example, spin-coating of the 5 w% solution, which led to a film thickness of 124 nm, showed significant phase segregation (Fig. 6.5). In this film, κ was observed to remain almost unchanged: κ in an i-PMMA(30 mol%):PVA(70 mol%) film made from the 5w% solution was $0.24 \pm 0.01 \text{ Wm}^{-1}\text{K}^{-1}$, while κ in unmixed i-PMMA and PVA were 0.25 ± 0.01 and $0.17 \pm 0.02 \text{ Wm}^{-1}\text{K}^{-1}$, respectively. To increase the miscibility of the two components, a thinner solution (1w% polymers in the DMF solution) was prepared and spin-coated, leading to smooth and continuous films of PMMA:PVA. The resultant film thickness ranged from 15.6 to 20.7 nm, which is sufficiently thin to cause the DMF solution to evaporate instantly. The film was therefore likely solidified before phase segregation occurred. AFM images for the films made from thinner solution (1w%) clearly show a continuous surface profile (Fig. 6.6). For this reason, all solutions of various mixture ratios were prepared with 1w% of polymers, leading to continuous films for all mixture ratios.

In PMMA:PVA films without phase segregation, strong H-bonding is expected, since they each have a hydrogen bonding agent in every other carbon atom in the chain and their backbones each have a simple linear shape without large side chains. As can be seen in Figs. 6.7a and 6.7b, κ in the mixture significantly increased as the monomer molar ratio of PMMA:PVA approaches to 0.45:0.55. Since measuring the H-bonding concentration in a thin film has numerous practical difficulties, the H-bonding concentration (ϕ_H) is approximated by $\phi_H = \min(n_{PMMA}, 0.8n_{PVA})$, assuming that all the H-bonding donor (acceptor) forms a H-bond; PVA used in this work is 80%

hydrolyzed (i.e., 80% of PVA monomer contains the hydroxyl group). This assumption predicts the optimal mole fraction of PMMA monomers for the maximum inter-chain H-bonding concentration to be 44.4 mol%. Note that n_{PMMA} and n_{PVA} are the monomer concentration rather than polymer chain concentration appeared in Eq. 6.7; the mixture ratio was controlled based on the monomer concentration.

In reality, the portion of monomers that participate in the inter-polymer H-bonding is not 100%, because not all the PMMA chains situate within the proximity of a PVA chain. This imperfect mixing of two polymers is expected to result in the spatial distribution in chemical bonds consisting of strong H-bonds and weak VDW bonds. Since H-bonding is known to increase the mechanical strength of polymer films [132], the viscoelastic property of the polymer surface is expected to be different at the H-bonding rich and the VDW bonding rich regions. To probe the spatial distribution of the H-bonding, the phase image of the AFM tapping mode that measures the phase difference between input and out signals was taken, since it is known to reflect the surface viscoelastic property [133]. As can be seen in Fig. 6.6, the mixtures that showed the maximum thermal conductivities appear to have exceptionally flat AFM phase images, which imply their homogeneous chemical composition.

To quantify the AFM phase image, its standard deviation (σ_{SDEV}) was calculated from the measured roughness. σ_{SDEV} in i-PMMA(45 mol%):PVA(55 mol%) and (a-PMMA(45 mol%):PVA(55 mol%) were 0.162° and 0.38° , respectively, which are far smaller than the unmixed i-PMMA (0.59°), a-PMMA (0.71°), and PVA (0.69°) (Table 6.1). Since the chemical composition of unmixed polymer must be identical, the larger values of σ_{SDEV} in monopolymeric films indicate the variation of surface polymer packing density, further implying the

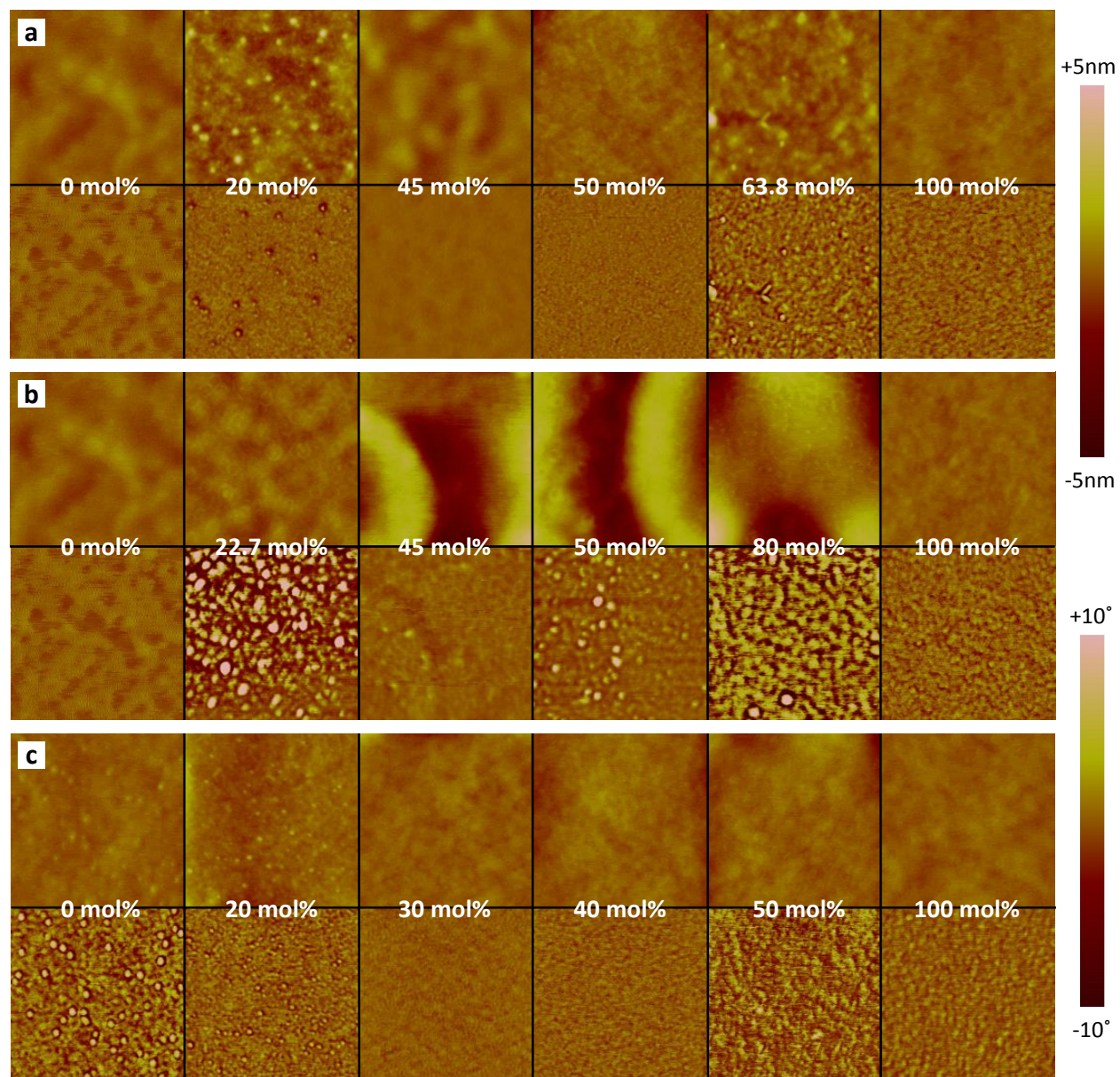


Figure 6.6 | Tapping-mode AFM topography and phase images for i- and a-PMMA:PVA and PAP:PAA spin-coated films. (a-c) AFM topography (upper) and phase images (lower) for i-PMMA:PVA spin-coated films at various mol% of i-PMMA (a), a-PMMA:PVA spin-coated films at various mol% of a-PMMA (b), and PAP:PAA spin-coated films at various mol% of PAP (c). Colour bar scales are ± 5 nm for all topography images and $\pm 10^\circ$ for all phase images. All images shown have a size of $500\text{nm} \times 500\text{nm}$.

supreme packing density in high- κ samples compared with the unmixed polymers. When two polymers are mixed well (i.e., low σ_{DEV}), strong H-bonding decreases the distance between polymer chains, and hence increases the packing density [128]. Together with the expected H-

bonding interaction, this larger packing density in the optimal mixture ratio leads to increase in κ to be not parabolic as predicted by Eq. 6.7 but similar to a delta function (Figs 6.7a-c).

As a likely result, κ in i-PMMA(50 mol%):PVA(50 mol%) was measured to be $1.17 \pm 0.13 \text{ Wm}^{-1}\text{K}^{-1}$, and κ in a-PMMA(45 mol%):PVA(55 mol%) was measured to be $1.16 \pm 0.11 \text{ Wm}^{-1}\text{K}^{-1}$; these values are more than a factor of 5 larger than the thermal conductivities of the constituent polymers (i-PMMA: 0.25 ± 0.01 , a-PMMA: 0.22 ± 0.01 and PVA: $0.17 \pm 0.02 \text{ Wm}^{-1}\text{K}^{-1}$).

The XPS spectrum of O_{1s} represents the chemical potential that the oxygen atom experiences, and thus provides useful information regarding the chemical bonding of oxygen. As can be seen in Fig. 6.8, the peak of O_{1s} shifts to a lower binding energy as the mixture ratio approaches 0.45:0.55, showing a similar trend as the thermal conductivity. This peak shift is clear evidence

i-PMMA mol%	$\sigma_{SDEV} (^{\circ})$	a-PMMA mol%	$\sigma_{SDEV} (^{\circ})$	PAP mol%	$\sigma_{SDEV} (^{\circ})$
0	0.69	0	0.69	0	1.55
9.9	0.22	9.9	0.28	11.5	1.94
20	0.53	22.7	3.31	20	0.81
30.6	0.80	30.6	2.98	25.7	1.44
40	0.52	35	6.81	30 ^(*)	0.38
45	0.16	45	0.38	30 ^(**)	0.35
50	0.36	50	1.39	40	0.53
55	0.55	55	0.73	50	1.34
63.8	1.02	63.8	0.89	60	1.26
80	1.22	80	2.43	67.4	1.26
100	0.59	100	0.71	100	0.61

*: $\kappa = 1.56 \text{ Wm}^{-1}\text{K}^{-1}$, **: $\kappa = 1.72 \text{ Wm}^{-1}\text{K}^{-1}$

Table 6.1 | Standard deviation of the AFM phase images (σ_{SDEV}) in PMMA:PVA and PAP:PAA mixtures.

of a significant change in chemical bonding of the oxygen atom and presumably due to the shorter polymer packing distance in high- κ samples (i.e., low σ_{SDEV}), yet current understanding regarding the mechanisms of H-bonding and polymer packing cannot fully explain this large shift in the binding energy (1 eV for i-PMMA:PVA, 2 eV for a-PMMA:PVA). Further investigation of the quantitative study of this shift is required.

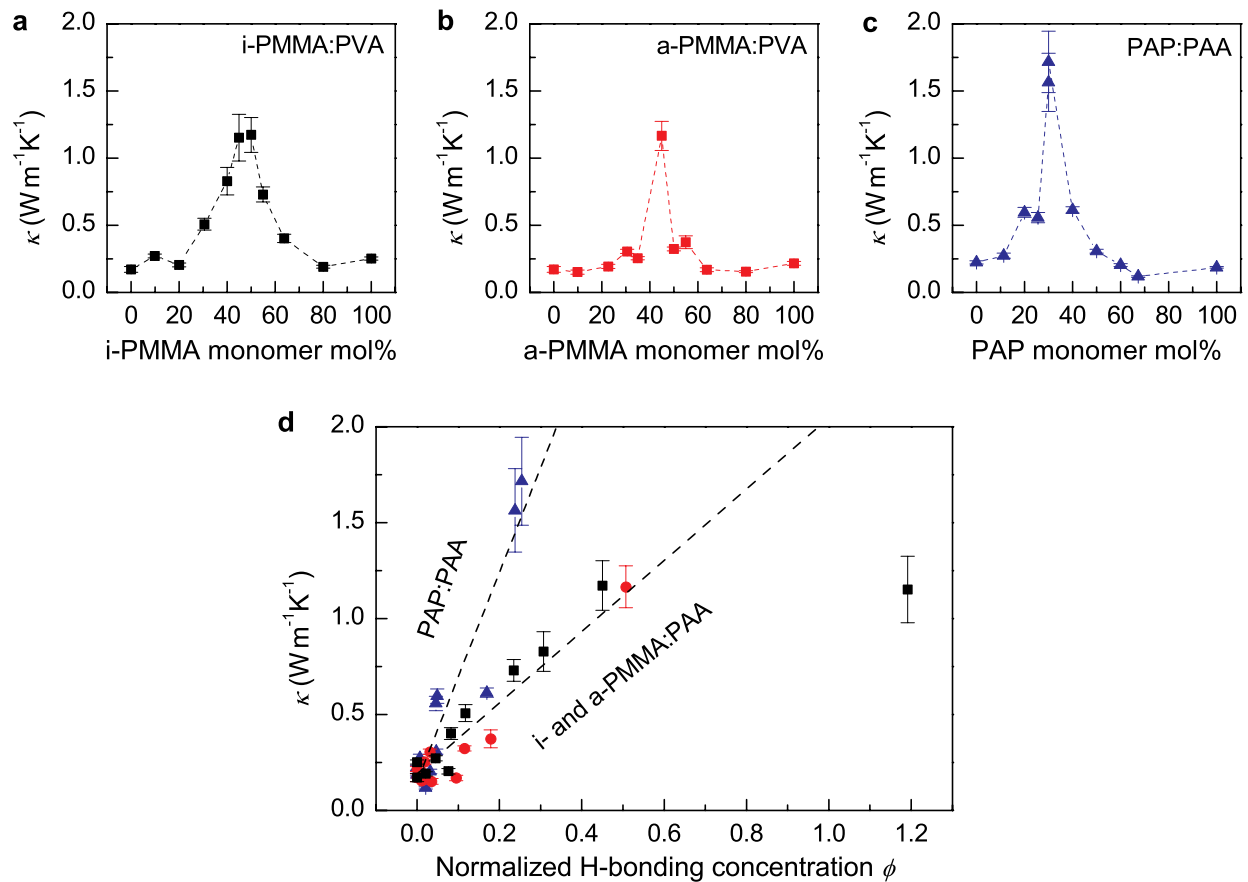


Figure 6.7 | Thermal conductivity in the H-bonding mixtures. (a-c) Measured thermal conductivities in i-PMMA:PVA spin-coated films at various mol% of i-PMMA **(a)**, a-PMMA:PVA spin-coated films at various mol% of a-PMMA **(b)**, and PAP:PAA spin-coated films at various mol% of PAP **(c)**. **(d)** Thermal conductivity versus H-bonding concentration normalized by the standard deviation of the AFM phase image. Also shown is the best fitting for the PMMA:PVA and the PAP:PAA data (dashed line).

6.5.2 Mixtures of PAP and PVA

PAP contains an amide (a strong H-bonding acceptor) on every other carbon atom along its backbone. Furthermore, this amide is oriented to the outside of the PAP chain, and thereby is capable of forming a short H-bond with an H-bonding donor. For these reasons, PAP is expected to form strong H-bonds with PAA, which contains a hydroxyl group on every other carbon atom along its backbone. Similar to PMMA:PVA, PAP:PAA mixtures also exhibit a clear trend in σ_{SDEV} (Fig. 6.6c) that its magnitude significantly decreases in the mixture ratio that maximizes κ . σ_{SDEV} in PAP(30 mol%):PAA(70 mol%) was measured to be 0.35° , which is again much smaller than the unmixed PAP (0.61°) and PAA (1.55°), indicating both the homogeneous distribution of H-bonds and the highly packed polymer chains. A delta-like peak in κ occurs, which is similar with the PMMA:PVA pairs, and κ was measured to be $1.72 \text{ Wm}^{-1}\text{K}^{-1}$, which is the highest value reported among non-crystalline (amorphous) organic materials. The optimal mixture ratio is PAP(30 mol%):PVA(70 mol%) rather than the 1:1 ratio as predicted by Eq. 6.7. This biased optimal mol% of PAP is because PAA contains both a hydroxyl and a carbonyl group and thereby is capable of self H-bonding within its own backbone, which does not contribute to increasing $\sigma_{H,C}$ in the di-polymeric plastic. The fact that κ is maximized at 70 mol% suggests that approximately half of the hydroxyl groups in the PAA chain are involved in self H-bonding; the calculated H-bonding concentration, $\phi_H = \min(n_{PAP}, 0.5n_{PAA})$, predicts the optimal n_{PAP} for the maximum inter-chain H-bonding concentration to be 33.3 mol%.

The O_{1s} XPS spectrum of the PAP:PAA mixtures, which provides the change in chemical bonding of the oxygen atom, is shown in Fig. 6.8c. While the deconvolution of the O_{1s} XPS spectrum is challenging because of the many peaks associated with O_{1s} (the carbonyl groups in both PAP and PAA as well as the hydroxyl group in PAA), the position of the O_{1s} peak for

PAP(30 mol%):PAA(70 mol%) with the maximum κ ($1.72 \text{ Wm}^{-1}\text{K}^{-1}$) again appears to red-shift to a lower binding energy compared with other PAP:PAA mixture ratios. Likewise the PMMA:PVA pair, this red-shift of O_{1s} peak for the high- κ sample indicates the change in the chemical bonding of oxygen atom, which is presumably due to the decrease in inter-polymer distance as evidenced by its small σ_{SEV} .

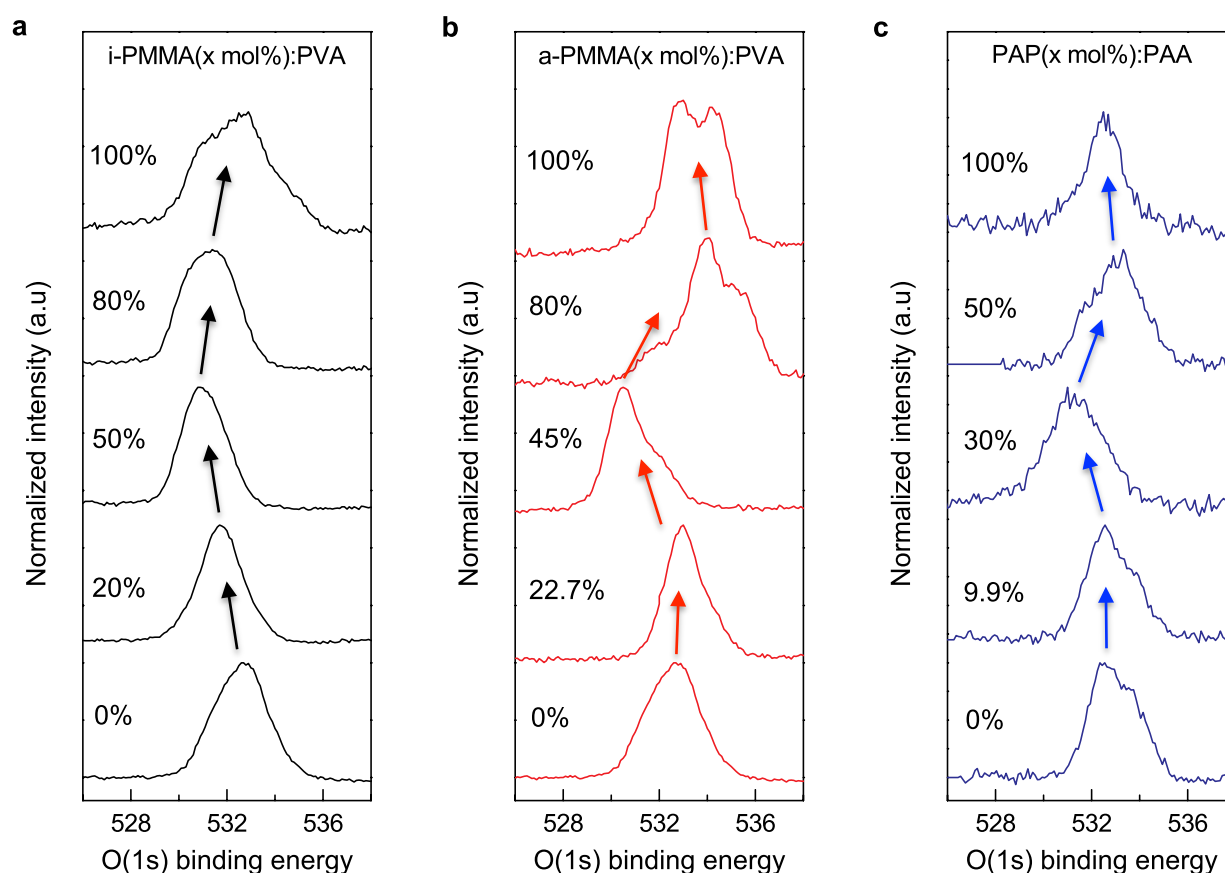


Figure 6.8 | O_{1s} XPS spectra of i- and a-PMMA:PVA and PAP:PAA at various mol% of the H-bonding acceptor monomer. (a-c) Measured O_{1s} XPS spectra in i-PMMA:PVA spin-coated films at various mol% of i-PMMA (a), a-PMMA:PVA spin-coated films at various mol% of a-PMMA (b), and PAP:PAA spin-coated films at various mol% of PAP (c). Peak positions were calibrated by the Au(4f) peak simultaneously measured with the O_{1s} peak; the XPS beam spot contained both a gold and a polymer film. Data courtesy of Lei Shao (University of Michigan).

6.5.3 κ versus ϕ

In this Chapter, three candidate mixtures of polymer that are capable to form strong H-bonding were tested, showing similar trend of the delta-peak like increase in κ , decrease in σ_{SDEV} , and the red-shift of the O_{1s} XPS spectra. Since σ_{SDEV} is inversely proportional to the polymer packing density (and hence the H-bonding distance) [134] and also to the homogeneity of H-bonds, the calculated H-bonding concentration (ϕ_H) was normalized by σ_{SDEV} in order to take account into these effects: $\phi = \phi_H/\sigma_{SDEV}$. Figure 6.7d plots ϕ versus κ for three H-bonding mixtures, showing the clear linear trend in κ versus ϕ . A stronger correlation between κ and ϕ (i.e., larger $d\kappa/d\phi$) is observed in PAP:PAA, which I ascribe to the capability of amide group for stronger H-bonding as the nitrogen atom can additionally make the amide group more electronegative than the carbonyl group itself. While the lowest σ_{SDEV} occurred in i-PMMA(45 mol%):PVA(55 mol%), κ remained almost unchanged, indicating that the effect of the H-bonding homogeneity on the thermal conductivity is saturated. $d\kappa/d\phi$ in i-PMMA:PVA and a-PMMA:PVA is observed to be equal to each other, indicating that the H-bonding strength is independent of the tacticity of PMMA.

Chapter 7

Conclusion and insights

The plastics industry is the third largest manufacturing industry in the United States; its productivity has grown 2.3 percent per year since 1980, while the average productivity among all manufacturing industries is 1.9 percent per year during the same period of time [135]. This active plastic market is a result of the numerous advantages of organic materials, such as low weight, durability, versatility, and amenability to low-energy manufacturing. They are used in virtually all product areas, and deeply integrated into modern human life.

Despite these benefits, organic materials have two major limitations for certain applications: they are poor conductors of electricity and heat. The contribution of my dissertation relates to these limitations in current organic materials, as I have presented strategies for improving charge carrier mobility in doped organic semiconductors (OSCs) and improving thermal conductivity in common commercial plastic materials.

The first contribution of this work has been to provide insight regarding charge transport mechanisms in organic semiconductors, which are key to making OSCs more electrically conductive. I developed a model of the Seebeck coefficient appropriate for OSCs, and demonstrated the further use of this model to quantitatively determine the degree of carrier localization. The localization lengths of numerous organic semiconductors were studied based on

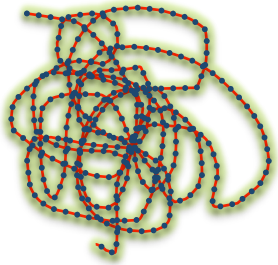
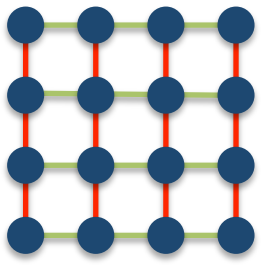
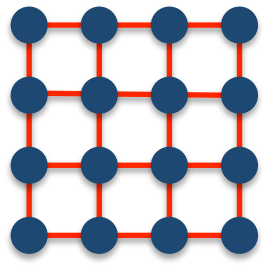
Seebeck coefficient data gathered from either prior literature or my own measurements, from which three distinct hopping transport regimes became apparent: activated, intermediate, and variable hopping. Transport in several high-mobility organic semiconductors tested in this work was found to be in the intermediate hopping regime, in which dynamic disorder due to random intermolecular vibrations is the main source of carrier localization, and the carrier localization length was found to be as large as the molecular spacing. The hopping model with this relatively large localization length was shown to be consistent with the very weak dependence of carrier mobility on temperature observed in these high-mobility organic semiconductors and often interpreted as evidence of band transport (complete delocalization). The effects of dopants, additives, and morphology on carrier localization were determined, providing insight on fundamental questions that must be addressed in order to further improve carrier mobility in conducting plastics.


An experimental demonstration for this intermediate hopping transport was carried out in iodine-doped bulk pentacene films. By simultaneously measuring the Seebeck coefficient and electrical conductivity during iodine dedoping, a signature suggesting possible impurity scattering was observed for the first time among organic semiconductors, indicating weak carrier localization in the pentacene films.

Based on this understanding of charge carrier transport, I proposed the importance of reducing dopant volume in improving carrier mobility in doped organic semiconductors. This strategy of reducing dopant volume was applied to thermoelectric application, for which the conversion efficiency critically depends on carrier mobility. By reducing dopant volume, the three thermoelectric parameters were observed to uniquely vary in a manner that increases ZT , leading to a large value of $ZT = 0.42$ at room temperature in solution processed polymer films.

The last contribution of my dissertation is to propose a new approach for improving thermal conductivity in polymer materials. On the basis of the fact that inter-chain heat transfer in polymers is largely limited by the weak inter-chain van der Waals interaction, polymers were designed to have a stronger inter-chain bonding. Commercially popular poly(methyl methacrylate) and other polymers were blended in order to alter the weak van der Waals bonds to strong hydrogen bonding, and their thermal conductivities were shown to increase by a factor of 5 as H-bonding concentration increases, reaching over $1 \text{ Wm}^{-1}\text{K}^{-1}$. Compared to existing methods of increasing thermal conductivity, the suggested approach does not increase the materials price, is expected to enhance mechanical properties, and further is compatible with the common thermal molding method of manufacturing.

The strategies of reduced dopant volume for thermoelectric materials and increased intermolecular bonding for improved thermal conductivity in polymer mixtures showed promising results, suggesting paths for future work. For improving electrical transport, I believe the dynamic disorder caused by the intermolecular vibrations is the primary challenge that organic semiconductors must overcome in order to improve their charge carrier mobility to the level of crystalline inorganic semiconductors (Fig. 7.1). The importance of dynamic disorder in OSCs has only very recently been emphasized in the literature [136], and many experimental and theoretical studies still remain to be done. The effects of molecular structure, intermolecular interactions, and dopant type on dynamic disorder are interesting and worthy of future study. For particular applications that need to use doped organic semiconductors (e.g., thermoelectric generators), the efficiency of molecular doping needs to be improved, as nonzero total dopant volume can result in significant decreased carrier mobility.

	a – amorphous OSCs	b – crystalline OSCs	c – crystalline ISCs
Source of disorder	Static disorder + Dynamic disorder	Dynamic disorder (thermal vibration)	None (actually, very small but negligible)
Performance	$\mu \sim 10^{-3} \text{ cm}^2 \text{ V}^{-1} \text{ s}^{-1}$	$\mu \sim 10^0 \text{ cm}^2 \text{ V}^{-1} \text{ s}^{-1}$	$\mu \sim 10^3 \text{ cm}^2 \text{ V}^{-1} \text{ s}^{-1}$
History	Past OSCs	Current OSCs	Dream OSCs
α	$\sim 1 \text{ \AA}$	$\sim 10 \text{ \AA}$	Mean free path $\sim 10^2 \text{ \AA}$
Appearance			

 **van der Waals bonds** – very weak (~ 10 to 100 meV) – large vibration at 300K



Next step? Suppress the dynamic disorder!
How? Hydrogen bonding instead of VDW?


 **covalent bonds** – very strong ($\sim 1 \text{ eV}$) – negligible vibration at 300K

Figure 7.1 | OSCs – past, current, and future. (a-c) The source of disorder, material performance, and microscopic appearance of amorphous OSCs (a), crystalline OSCs (b), and crystalline ISCs (c). The gap between the crystalline OSCs and the crystalline ISCs is the dynamic disorder, the current challenge to overcome.

The engineered intermolecular interaction for increased thermal conductivity promises new possibilities for the plastic industry, as large thermal conductivity leads to better functionality and reliability of plastic products. In the presented work, only hydrogen bonding was tested as a replacement for the weak van der Waals intermolecular interaction, while the energy of the hydrogen bonding itself varies among numerous polymers and, furthermore, other strong types of bonding such as ionic and covalent (e.g., cross-linking) bonding are also promising candidate for this strategy. Combining the presented strategy with other existing methods (e.g., high thermal conductivity filler) is also an interesting future task to investigate whether this

combination can lead to synergetic effects on the thermal conductivity; the filler method also suffers from low thermal boundary conduction between fillers and polymer chains.

References

1. Hicks, L.D. and M.S. Dresselhaus, *Effect of Quantum-Well Structures on the Thermoelectric Figure of Merit*. Physical Review B, 1993. **47**(19): p. 12727-12731.
2. Hicks, L.D. and M.S. Dresselhaus, *Thermoelectric Figure of Merit of a One-Dimensional Conductor*. Physical Review B, 1993. **47**(24): p. 16631-16634.
3. Bell, L.E., *Cooling, heating, generating power, and recovering waste heat with thermoelectric systems*. Science, 2008. **321**(5895): p. 1457-1461.
4. Wang, H., et al., *Heavily Doped p-Type PbSe with High Thermoelectric Performance: An Alternative for PbTe*. Advanced Materials, 2011. **23**(11): p. 1366-1370.
5. Hochbaum, A.I., et al., *Enhanced thermoelectric performance of rough silicon nanowires*. Nature, 2008. **451**(7175): p. 163-U5.
6. Ohta, H., et al., *Giant thermoelectric Seebeck coefficient of two-dimensional electron gas in SrTiO₃*. Nature Materials, 2007. **6**(2): p. 129-134.
7. Kim, G. and K.P. Pipe, *Thermoelectric model to characterize carrier transport in organic semiconductors*. Physical Review B, 2012. **86**(8): p. 085208.
8. Sun, Y.M., et al., *Organic Thermoelectric Materials and Devices Based on p- and n-Type Poly(metal 1,1,2,2-ethenetetrathiolate)s*. Advanced Materials, 2012. **24**(7): p. 932.
9. Kim, B.G., et al., *A molecular design principle of lyotropic liquid-crystalline conjugated polymers with directed alignment capability for plastic electronics*. Nature Materials, 2013. **12**(7): p. 659-664.
10. Diao, Y., et al., *Solution coating of large-area organic semiconductor thin films with aligned single-crystalline domains*. Nature Materials, 2013. **12**(7): p. 665-671.
11. Gunes, S., H. Neugebauer, and N.S. Sariciftci, *Conjugated polymer-based organic solar cells*. Chemical Reviews, 2007. **107**(4): p. 1324-1338.
12. Thompson, B.C. and J.M.J. Frechet, *Organic photovoltaics - Polymer-fullerene composite solar cells*. Angewandte Chemie-International Edition, 2008. **47**(1): p. 58-77.
13. Bubnova, O., et al., *Optimization of the thermoelectric figure of merit in the conducting polymer poly(3,4-ethylenedioxythiophene)*. Nature Materials, 2011. **10**(6): p. 429-433.

14. Jiang, F.X., et al., *Thermoelectric performance of poly(3,4-ethylenedioxythiophene): Poly(styrenesulfonate)*. Chinese Physics Letters, 2008. **25**(6): p. 2202-2205.
15. Chang, K.C., et al., *The Thermoelectric Performance of Poly(3,4-ethylenedioxythiophene)/Poly(4-styrenesulfonate) Thin Films*. Journal of Electronic Materials, 2009. **38**(7): p. 1182-1188.
16. Kim, D., et al., *Improved Thermoelectric Behavior of Nanotube-Filled Polymer Composites with Poly(3,4-ethylenedioxythiophene) Poly(styrenesulfonate)*. Acs Nano, 2010. **4**(1): p. 513-523.
17. Liu, C.C., et al., *Highly conducting free-standing poly(3,4-ethylenedioxythiophene)/poly(styrenesulfonate) films with improved thermoelectric performances*. Synthetic Metals, 2010. **160**(23-24): p. 2481-2485.
18. See, K.C., et al., *Water-Processable Polymer-Nanocrystal Hybrids for Thermoelectrics*. Nano Letters, 2010. **10**(11): p. 4664-4667.
19. Zhang, B., et al., *Promising Thermoelectric Properties of Commercial PEDOT:PSS Materials and Their Bi₂Te₃ Powder Composites*. Acs Applied Materials & Interfaces, 2010. **2**(11): p. 3170-3178.
20. Kim, G.H., et al., *Engineered doping of organic semiconductors for enhanced thermoelectric efficiency*. Nature Materials, 2013. **12**(8): p. 719-723.
21. Kume, H. *Fujifilm Shows High-efficiency Thermoelectric Converter Using Organic Material*. 2013 [cited 2013 October 19]; Available from: http://techon.nikkeibp.co.jp/english/NEWS_EN/20130206/264517.
22. Gregory P. Moriarty, K.B., Bart Stevens, Choongho Yu, and Jaime C. Grunlan, *Fully Organic Nanocomposites with High Thermoelectric Power Factors by using a Dual-Stabilizer Preparation*. Energy Technology, 2013. **1**(4): p. 265-272.
23. Ioffe, A.F., *Semiconductor thermoelements, and Thermoelectric cooling*. [Rev. and supplemented for the English ed. 1957, London,; Infosearch. 184 p.
24. Jacoboni, C., et al., *Review of Some Charge Transport Properties of Silicon*. Solid-State Electronics, 1977. **20**(2): p. 77-89.
25. Park, T., et al., *Flexible PEDOT electrodes with large thermoelectric power factors to generate electricity by the touch of fingertips*. Energy & Environmental Science, 2013. **6**(3): p. 788-792.
26. Shirakawa, H., et al., *Synthesis of Electrically Conducting Organic Polymers - Halogen Derivatives of Polyacetylene, (Ch)X*. Journal of the Chemical Society-Chemical Communications, 1977(16): p. 578-580.

27. Anderson, P.W., *Absence of Diffusion in Certain Random Lattices*. Physical Review, 1958. **109**(5): p. 1492-1505.
28. Bohlin, J., M. Linares, and S. Stafstrom, *Effect of dynamic disorder on charge transport along a pentacene chain*. Physical Review B, 2011. **83**(8): p. 085209.
29. Troisi, A. and G. Orlandi, *Dynamics of the intermolecular transfer integral in crystalline organic semiconductors*. Journal of Physical Chemistry A, 2006. **110**(11): p. 4065-4070.
30. Jurchescu, O.D., J. Baas, and T.T.M. Palstra, *Effect of impurities on the mobility of single crystal pentacene*. Applied Physics Letters, 2004. **84**(16): p. 3061-3063.
31. Sakanoue, T. and H. Sirringhaus, *Band-like temperature dependence of mobility in a solution-processed organic semiconductor*. Nature Materials, 2010. **9**(9): p. 736-740.
32. Coehoorn, R., et al., *Charge-carrier concentration dependence of the hopping mobility in organic materials with Gaussian disorder*. Physical Review B, 2005. **72**(15): p. 155206.
33. Pasveer, W.F., et al., *Unified description of charge-carrier mobilities in disordered semiconducting polymers*. Physical Review Letters, 2005. **94**(20): p. 206601.
34. Miller, A. and E. Abrahams, *Impurity Conduction at Low Concentrations*. Physical Review, 1960. **120**(3): p. 745-755.
35. Chanda, M. and S.K. Roy, *Plastics technology handbook*, 2007, CRC Press/Taylor & Francis Group: Boca Raton, FL.
36. Mamunya, Y.P., et al., *Electrical and thermal conductivity of polymers filled with metal powders*. European Polymer Journal, 2002. **38**(9): p. 1887-1897.
37. Huxtable, S.T., et al., *Interfacial heat flow in carbon nanotube suspensions*. Nature Materials, 2003. **2**(11): p. 731-734.
38. Yu, A.P., et al., *Enhanced Thermal Conductivity in a Hybrid Graphite Nanoplatelet - Carbon Nanotube Filler for Epoxy Composites*. Advanced Materials, 2008. **20**(24): p. 4740.
39. Shahil, K.M.F. and A.A. Balandin, *Graphene-Multilayer Graphene Nanocomposites as Highly Efficient Thermal Interface Materials*. Nano Letters, 2012. **12**(2): p. 861-867.
40. Henry, A. and G. Chen, *High Thermal Conductivity of Single Polyethylene Chains Using Molecular Dynamics Simulations*. Physical Review Letters, 2008. **101**(23): p. 235502.
41. Shen, S., et al., *Polyethylene nanofibres with very high thermal conductivities*. Nature Nanotechnology, 2010. **5**(4): p. 251-255.
42. Wang, X.J., et al., *Thermal Conductivity of High-Modulus Polymer Fibers*. Macromolecules, 2013. **46**(12): p. 4937-4943.

43. Welty, J.R., *Fundamentals of momentum, heat, and mass transfer*. 5th ed. 2008, Hoboken, N.J. ; Chichester: Wiley. xiii, 711 p.
44. *Rayleigh number*. [cited 2013 October 25]; Available from: http://en.wikipedia.org/wiki/Rayleigh_number.
45. DaRosa, A.V., *Fundamentals of Renewable Energy Processes, 2nd Edition*. Fundamentals of Renewable Energy Processes, 2nd Edition, 2009: p. 1-844.
46. Mitdank, R., et al., *Enhanced magneto-thermoelectric power factor of a 70 nm Ni-nanowire*. Journal of Applied Physics, 2012. **111**(10): p. 104320.
47. Fisichella, G., et al., *Micro- and nanoscale electrical characterization of large-area graphene transferred to functional substrates*. Beilstein Journal of Nanotechnology, 2013. **4**: p. 234-242.
48. Zhang, K.J., et al., *Thermal and Electrical Transport in Ultralow Density Single-Walled Carbon Nanotube Networks*. Advanced Materials, 2013. **25**(21): p. 2926-2931.
49. Borca-Tasciuc, T., A.R. Kumar, and G. Chen, *Data reduction in 3 omega method for thin-film thermal conductivity determination*. Review of Scientific Instruments, 2001. **72**(4): p. 2139-2147.
50. Lee, S.M. and D.G. Cahill, *Heat transport in thin dielectric films*. Journal of Applied Physics, 1997. **81**(6): p. 2590-2595.
51. Cahill, D.G., et al., *Nanoscale thermal transport*. Journal of Applied Physics, 2003. **93**(2): p. 793-818.
52. Ju, Y.S., K. Kurabayashi, and K.E. Goodson, *Thermal characterization of anisotropic thin dielectric films using harmonic Joule heating*. Thin Solid Films, 1999. **339**(1-2): p. 160-164.
53. Cahill, D.G., *Thermal-Conductivity Measurement from 30-K to 750-K - the 3-Omega Method*. Review of Scientific Instruments, 1990. **61**(2): p. 802-808.
54. Zhang, Q.G., et al., *Influence of grain boundary scattering on the electrical and thermal conductivities of polycrystalline gold nanofilms*. Physical Review B, 2006. **74**(13): p. 134109.
55. Kurabayashi, K., et al., *Measurement of the thermal conductivity anisotropy in polyimide films*. Journal of Microelectromechanical Systems, 1999. **8**(2): p. 180-191.
56. Dennler, G., M.C. Scharber, and C.J. Brabec, *Polymer-Fullerene Bulk-Heterojunction Solar Cells*. Advanced Materials, 2009. **21**(13): p. 1323-1338.
57. Pei, Y.Z., et al., *Low effective mass leading to high thermoelectric performance*. Energy & Environmental Science, 2012. **5**(7): p. 7963-7969.

58. Mott, N.F. and E.A. Davis, *Electronic processes in non-crystalline materials*. International series of monographs on physics. 1971, Oxford,,: Clarendon Press. xiii, 437 p.
59. Troisi, A. and G. Orlandi, *Charge-transport regime of crystalline organic semiconductors: Diffusion limited by thermal off-diagonal electronic disorder*. Physical Review Letters, 2006. **96**(8): p. 086601.
60. Arkhipov, V.I., et al., *Charge carrier mobility in doped semiconducting polymers*. Applied Physics Letters, 2003. **82**(19): p. 3245-3247.
61. Tanase, C., et al., *Unification of the hole transport in polymeric field-effect transistors and light-emitting diodes*. Physical Review Letters, 2003. **91**(21): p. 216601.
62. Movaghar, B. and W. Schirmacher, *On the Theory of Hopping Conductivity in Disordered-Systems*. Journal of Physics C-Solid State Physics, 1981. **14**(6): p. 859-880.
63. Vissenberg, M.C.J.M. and M. Matters, *Theory of the field-effect mobility in amorphous organic transistors*. Physical Review B, 1998. **57**(20): p. 12964-12967.
64. Arkhipov, V.I., et al., *Weak-field carrier hopping in disordered organic semiconductors: the effects of deep traps and partly filled density-of-states distribution*. Journal of Physics-Condensed Matter, 2002. **14**(42): p. 9899-9911.
65. Fishchuk, I.I., et al., *Effective-medium theory of hopping charge-carrier transport in weakly disordered organic solids*. Physical Review B, 2002. **65**(12): p. 125201.
66. Roichman, Y., Y. Preezant, and N. Tessler, *Analysis and modeling of organic devices*. Physica Status Solidi a-Applied Research, 2004. **201**(6): p. 1246-1262.
67. Fishchuk, I.I., et al., *Analytic model of hopping mobility at large charge carrier concentrations in disordered organic semiconductors: Polarons versus bare charge carriers*. Physical Review B, 2007. **76**(4): p. 045210.
68. Marumoto, K., et al., *Spatial extent of wave functions of gate-induced hole carriers in pentacene field-effect devices as investigated by electron spin resonance*. Physical Review Letters, 2006. **97**(25): p. 256603.
69. Schmechel, R., *Gaussian disorder model for high carrier densities: Theoretical aspects and application to experiments*. Physical Review B, 2002. **66**(23): p. 235206.
70. Ambegaokar, V., B.I. Halperin, and J.S. Langer, *Hopping Conductivity in Disordered Systems*. Physical Review B-Solid State, 1971. **4**(8): p. 2612.
71. Bassler, H., *Charge Transport in Disordered Organic Photoconductors - a Monte-Carlo Simulation Study*. Physica Status Solidi B-Basic Research, 1993. **175**(1): p. 15-56.

72. Shklovskii, B.I. and A.L. *Efros, *Electronic properties of doped semiconductors*. Springer series in solid-state sciences. 1984, Berlin ; New York: Springer-Verlag. xii, 388 p.
73. Hesse, R., W. Hofberger, and H. Bassler, *Absorption-Spectra of Disordered Solid Tetracene and Pentacene*. Chemical Physics, 1980. **49**(2): p. 201-211.
74. Yogev, S., et al., *Direct measurement of density of states in pentacene thin film transistors*. Physical Review B, 2011. **84**(16): p. 165124.
75. Ullah, M., et al., *Dependence of Meyer-Neldel energy on energetic disorder in organic field effect transistors*. Applied Physics Letters, 2010. **96**(21): p. 213306.
76. Roichman, Y. and N. Tessler, *Generalized Einstein relation for disordered semiconductors - Implications for device performance*. Applied Physics Letters, 2002. **80**(11): p. 1948-1950.
77. Gregg, B.A., S.G. Chen, and R.A. Cormier, *Coulomb forces and doping in organic semiconductors*. Chemistry of Materials, 2004. **16**(23): p. 4586-4599.
78. Pernstich, K.P., B. Rossner, and B. Batlogg, *Field-effect-modulated Seebeck coefficient in organic semiconductors*. Nature Materials, 2008. **7**(4): p. 321-325.
79. Harada, K., et al., *Improved thermoelectric performance of organic thin-film elements utilizing a bilayer structure of pentacene and 2,3,5,6-tetrafluoro-7,7,8,8-tetracyanoquinodimethane (F-4-TCNQ)*. Applied Physics Letters, 2010. **96**(25): p. 253304.
80. Käfer, D., *Characterization and Optimization of Growth and Electronic Structure of Organic Thin Films for Applications in Organic Electronics*, in the Department of Physical Chemistry I 2008, the Ruhr-University Bochum, Germany.
81. Lang, D.V., et al., *Amorphouslike density of gap states in single-crystal pentacene*. Physical Review Letters, 2004. **93**(8): p. 086802.
82. Yoneya, N., et al., *Reduction of contact resistance in pentacene thin-film transistors by direct carrier injection into a-few-molecular-layer channel*. Applied Physics Letters, 2004. **85**(20): p. 4663-4665.
83. Podzorov, V., et al., *Hall effect in the accumulation layers on the surface of organic semiconductors*. Physical Review Letters, 2005. **95**(22): p. 226601.
84. Kahol, P.K., et al., *Effect of dopants on electron localization length in polyaniline*. Synthetic Metals, 2003. **139**(2): p. 191-200.
85. Dlott, D.D., *Optical Phonon Dynamics in Molecular-Crystals*. Annual Review of Physical Chemistry, 1986. **37**: p. 157-187.

86. Xia, Y.J., K. Sun, and J.Y. Ouyang, *Solution-Processed Metallic Conducting Polymer Films as Transparent Electrode of Optoelectronic Devices*. *Advanced Materials*, 2012. **24**(18): p. 2436-2440.
87. Crispin, X., et al., *The origin of the high conductivity of poly(3,4-ethylenedioxythiophene)-poly(styrenesulfonate) (PEDOT- PSS) plastic electrodes*. *Chemistry of Materials*, 2006. **18**(18): p. 4354-4360.
88. Elschner, A., *PEDOT : principles and applications of an intrinsically conductive polymer*. 2011, Boca Raton, FL: CRC Press. xxi, 355 p.
89. Walzer, K., et al., *Highly efficient organic devices based on electrically doped transport layers*. *Chemical Reviews*, 2007. **107**(4): p. 1233-1271.
90. Knupfer, M., *Exciton binding energies in organic semiconductors*. *Applied Physics a-Materials Science & Processing*, 2003. **77**(5): p. 623-626.
91. Fisher, T.E., et al., *The micro-mechanics of single molecules studied with atomic force microscopy*. *Journal of Physiology-London*, 1999. **520**(1): p. 5-14.
92. Nollau, A., et al., *Controlled n-type doping of a molecular organic semiconductor: Naphthalenetetracarboxylic dianhydride (NTCDA) doped with bis(ethylenedithio)-tetrathiafulvalene (BEDT-TTF)*. *Journal of Applied Physics*, 2000. **87**(9): p. 4340-4343.
93. Park, Y.W., *Structure and Morphology - Relation to Thermopower Properties of Conductive Polymers*. *Synthetic Metals*, 1991. **45**(2): p. 173-182.
94. von Muhlenen, A., et al., *Thermopower measurements on pentacene transistors*. *Physical Review B*, 2007. **75**(11): p. 115338.
95. Kim, G.H., M. Shtein, and K.P. Pipe, *Thermoelectric and bulk mobility measurements in pentacene thin films*. *Applied Physics Letters*, 2011. **98**(9): p. 093303.
96. Nelson, S.F., et al., *Temperature-independent transport in high-mobility pentacene transistors*. *Applied Physics Letters*, 1998. **72**(15): p. 1854-1856.
97. Knipp, D., R.A. Street, and A.R. Volkel, *Morphology and electronic transport of polycrystalline pentacene thin-film transistors*. *Applied Physics Letters*, 2003. **82**(22): p. 3907-3909.
98. Brinkmann, M., et al., *Electronic and structural evidences for charge transfer and localization in iodine-doped pentacene*. *Journal of Physical Chemistry A*, 2004. **108**(40): p. 8170-8179.
99. Sharifzadeh, S., et al., *Quasiparticle and optical spectroscopy of the organic semiconductors pentacene and PTCDA from first principles*. *Physical Review B*, 2012. **85**(12): p. 125307.

100. Slack, G., *Chapter 34 in CRC handbook of thermoelectrics (Editor: D. M. Rowe)*. 1995, Boca Raton, FL: CRC Press. vii, 701 p.
101. Hicks, L.D., et al., *Experimental study of the effect of quantum-well structures on the thermoelectric figure of merit*. Physical Review B, 1996. **53**(16): p. 10493-10496.
102. Poudel, B., et al., *High-thermoelectric performance of nanostructured bismuth antimony telluride bulk alloys*. Science, 2008. **320**(5876): p. 634-638.
103. Venkatasubramanian, R., et al., *Thin-film thermoelectric devices with high room-temperature figures of merit*. Nature, 2001. **413**(6856): p. 597-602.
104. Biswas, K., et al., *High-performance bulk thermoelectrics with all-scale hierarchical architectures*. Nature, 2012. **489**(7416): p. 414-418.
105. Hsu, K.F., et al., *Cubic AgPbmSbTe_{2+m}: Bulk thermoelectric materials with high figure of merit*. Science, 2004. **303**(5659): p. 818-821.
106. Sales, B.C., et al., *Filled skutterudite antimonides: Electron crystals and phonon glasses*. Physical Review B, 1997. **56**(23): p. 15081-15089.
107. Vining, C.B., *An inconvenient truth about thermoelectrics*. Nature Materials, 2009. **8**(2): p. 83-85.
108. Boukai, A.I., et al., *Silicon nanowires as efficient thermoelectric materials*. Nature, 2008. **451**(7175): p. 168-171.
109. Koh, Y.K., et al., *Comparison of the 3 omega method and time-domain thermoreflectance for measurements of the cross-plane thermal conductivity of epitaxial semiconductors*. Journal of Applied Physics, 2009. **105**(5): p. 054303.
110. Nardes, A.M., et al., *Microscopic understanding of the anisotropic conductivity of PEDOT : PSS thin films*. Advanced Materials, 2007. **19**(9): p. 1196.
111. Lang, U., et al., *Microscopical Investigations of PEDOT:PSS Thin Films*. Advanced Functional Materials, 2009. **19**(8): p. 1215-1220.
112. Sprenger, D. and O. Anderson, *Deconvolution of Xps Spectra*. Fresenius Journal of Analytical Chemistry, 1991. **341**(1-2): p. 116-120.
113. Casian, A., *Violation of the Wiedemann-Franz law in quasi-one-dimensional organic crystals*. Physical Review B, 2010. **81**(15): p. 155415.
114. Yue, R.R. and J.K. Xu, *Poly(3,4-ethylenedioxythiophene) as promising organic thermoelectric materials: A mini-review*. Synthetic Metals, 2012. **162**(11-12): p. 912-917.

115. Yoshida, A. and N. Toshima, *Gold Nanoparticle and Gold Nanorod Embedded PEDOT:PSS Thin Films as Organic Thermoelectric Materials*. Journal of Electronic Materials, 2013.
116. Kim, Y.H., et al., *Highly Conductive PEDOT:PSS Electrode with Optimized Solvent and Thermal Post-Treatment for ITO-Free Organic Solar Cells*. Advanced Functional Materials, 2011. **21**(6): p. 1076-1081.
117. Moniruzzaman, M. and K.I. Winey, *Polymer nanocomposites containing carbon nanotubes*. Macromolecules, 2006. **39**(16): p. 5194-5205.
118. Potts, J.R., et al., *Graphene-based polymer nanocomposites*. Polymer, 2011. **52**(1): p. 5-25.
119. Kim, G.-H., et al., *This work has not been published yet*.
120. *Automotive Plastics Market By Product (ABS, PP, PU, PVC, PE, PC, PMMA, PA), By Application (Power Trains, Under the Hood, Electrical Components, Chassis, Furnishing), Bio-based Opportunity (PLA, PHA, PCL, PBS) - Global Industry Analysis, Size, Share, Growth, Trends and Forecast, 2012 - 2018*. 2013 [cited 2013 October 10th]; Available from: <http://www.prweb.com/releases/2013/7/prweb10923470.htm>.
121. *Thermally conductive compounds reduce vehicle weight via metal replacement*. 2012 [cited 2013 October 10th]; Available from: <http://www.plasticstoday.com/articles/thermally-conductive-compounds-reduce-vehicle-weight-metal-replacement-plastic-20121004a>.
122. Nylund, C. and K. Meinander, *The influence of heat transfer coefficient on cooling time in injection molding*. Heat and Mass Transfer, 2005. **41**(5): p. 428-431.
123. O'Brien, P.J., et al., *Bonding-induced thermal conductance enhancement at inorganic heterointerfaces using nanomolecular monolayers*. Nature Materials, 2013. **12**(2): p. 118-122.
124. Kurabayashi, K., *Anisotropic thermal properties of solid polymers*. International Journal of Thermophysics, 2001. **22**(1): p. 277-288.
125. Volkov, A.N. and L.V. Zhigilei, *Scaling Laws and Mesoscopic Modeling of Thermal Conductivity in Carbon Nanotube Materials*. Physical Review Letters, 2010. **104**(21): p. 215902.
126. Balberg, I., et al., *Excluded Volume and Its Relation to the Onset of Percolation*. Physical Review B, 1984. **30**(7): p. 3933-3943.
127. Mark, J.E., *Physical properties of polymers handbook*. AIP series in polymers and complex materials. 1996, Woodbury, N.Y.: AIP Press. xv, 723 p.

128. Pascault, J.-P., *Thermosetting polymers*. Plastics engineering. 2002, New York: Marcel Dekker. viii, 477 p.
129. Jo, Y.S., et al., *RAFT homo- and copolymerization of N-acryloyl-morpholine, piperidine, and azocane and their self-assembled structures*. *Macromolecules*, 2008. **41**(4): p. 1140-1150.
130. Jin, Y.S., et al., *Origins of thermal boundary conductance of interfaces involving organic semiconductors*. *Journal of Applied Physics*, 2012. **112**(9): p. 093503.
131. Adoor, S.G., et al., *Solution and solid-state blend compatibility of poly(vinyl alcohol) and poly(methyl methacrylate)*. *Journal of Applied Polymer Science*, 2006. **100**(3): p. 2415-2421.
132. Lin, Y., et al., *Study of hydrogen-bonded blend of polylactide with biodegradable hyperbranched poly(ester amide)*. *Macromolecules*, 2007. **40**(17): p. 6257-6267.
133. Salmeron, M., et al., *Viscoelastic and Electrical-Properties of Self-Assembled Monolayers on Au(111) Films*. *Langmuir*, 1993. **9**(12): p. 3600-3611.
134. Kosaka, P.M., et al., *Atomic force microscopy reveals two phases in single stranded DNA self-assembled monolayers*. *Nanoscale*, 2013. **5**(16): p. 7425-7432.
135. *Fast Facts on Plastic*. [cited 2013 October 15th]; Available from: <http://www.plasticsindustry.org/AboutPlastics/content.cfm?ItemNumber=798&navItemNumber=1280>.
136. Alexander S. Eggeman, S.I., Alessandro Troisi, Henning Sirringhaus, and a.P.A. Midgley, *Measurement of molecular motion in organic semiconductors by thermal diffuse electron scattering*. *Nature Materials*, 2013: p. Advanced online publication, DOI: 10.1038/NMAT3710.